ON THE EFFECT OF LYMAN ALPHA TRAPPING DURING THE INITIAL COLLAPSE OF MASSIVE BLACK HOLE SEEDS.

A Dissertation
Presented to
The Academic Faculty

By

Qi Ge

In Partial Fulfillment
of the Requirements for the Degree
Doctor of Philosophy in the
School of Physics

Georgia Institute of Technology

May 2018

ON THE EFFECT OF LYMAN ALPHA TRAPPING DURING THE INITIAL COLLAPSE OF MASSIVE BLACK HOLE SEEDS.

Approved by:

Professor John Wise, Advisor
School of Physics
Georgia Institute of Technology

Professor Deirdre Shoemaker
School of Physics
Georgia Institute of Technology

Professor Tamara Bogdanovic
School of Physics
Georgia Institute of Technology

Professor David Ballantyne
School of Physics
Georgia Institute of Technology

Professor Richard Vuduc
School of Computational Science and Engineering
Georgia Institute of Technology

Date Approved: March 15, 2018

ACKNOWLEDGEMENTS

I would like to acknowledge my highest indebtedness and render my warmest thanks to my supervisor, Professor John Wise, who made this work possible. His friendly guidance and expert advice have been invaluable throughout all stages of the work.

My sincere thanks must also go to the members of my thesis advisory and exam committee: Professor Deirdre Shoemaker, Professor Tamara Bogdanovic, Professor David Ballantyne, and Professor Richard Vuduc. They generously gave their time to offer me valuable comments toward improving my work and provided me constructive criticism which helped me develop a broader perspective to my thesis.

I am most grateful to the people in CRA for lending me their expertise and intuition to my scientific and technical problems: Chao, D.K., Kirk, Aychi, KwangHo, Yu, Khai, Raj, Stavropoulos, Bryan, Bhavesh and many others.

I have special thanks to all my friends in Atlanta: Wenbin, Yang, Shangguo, Xiong, Xiaoyun, Kan, Xincheng, Zhangxian, Chao, Jingjing and He for their countless help.

I wish to show my deeply thank to my parents for their unconditional trust, timely encouragement, and endless patience. It was their love that raised me up again when I got weary. Without their raises and supports, I cannot finish my acedemic degrees.

Finally, I thank with love to Jing Li, my wife. Jing has been my great companion, loved, supported, encouraged, entertained, and helped me get through this agonizing period in the most positive way.

TABLE OF CONTENTS

LIST OF TABLES

LIST OF FIGURES

SUMMARY

In this thesis, we report on the formation of supermassive black holes and the effect of Lyα radiation trapping during their initial collapses, paying special attention to massive black hole seeds in the early Universe. The formation of supermassive black holes have been studied numerically over the last 30 years, and the direct collapse scenario is favorable in explaining the existence of quasars powered by 10^9 $M_\odot$ supermassive black holes when the Universe was less than one billion years old.

Radiation transfer of the Lyα line plays an important role in theories and observations of galaxies and black holes. This thesis utilizes a Monte Carlo method to solve the transport of Lyα radiation with cosmological simulations using the community-driven open-source code *Enzo*. We find that Lyα radiation is trapped in a precursor to a massive black hole seed, a collapsing metal-free gas cloud. This trapped radiation prevents the gas from cooling and gravitational compression heats the gas to 50,000 K.

The thesis is organized as follow. In Chapter 1, we introduce the background and review the literature on supermassive black hole formation and Lyα radiation transfer. In Chapter 2, we overview the numerical methods employed in the cosmological simulations with *Enzo* and the Monte Carlo radiation transfer scheme. In Chapter 3, we show our results on the impact of Lyα radiation trapping on the massive black hole seed formation, where we focus on a single cooling primordial halo. We conclude in Chapter 4, and we discuss future work that will apply machine learning to Lyα radiation transfer.

CHAPTER 1

INTRODUCTION AND BACKGROUND

In this thesis, we focus on the processes involving the initial structure formation in the early Universe. We are especially interested in the formation of supermassive black holes (SMBHs), paying special attention to the impact of radiation transfer on the formation of seed black holes that eventually grow into the SMBHs observed today. Theoretical models of dark matter halo growth and their associated galaxies have been established over the past 30 years to explain high-redshift galaxy observations. With the methods described in this thesis, we establish a baseline for the detailed mechanics of black hole seed formation in dark matter halos that can support efficient atomic hydrogen cooling that is main driver of early galaxy formation. While Lyman-α cooling plays a vital role during seed formation, this thesis focuses on its transfer through the optically-thin and thick regimes during a monolithic collapse into a massive black hole seed.

1.1 Supermassive Black Hole Formation

Typically, black holes with masses $\geq 10^5$ $M_\odot$ are regarded as SMBHs, and those with masses $10^2 - 10^5$ $M_\odot$ are called intermediate black holes (IMBHs). As material accretes onto these black holes, a significant fraction of their gravitational potential is released into the surrounding environment. SMBHs have been established as the central engines of active galactic nuclei (AGN Salpeter, 1964; Zel'dovich, 1964). Quasars, a type of AGN, are one of the most powerful probes of the early universe, providing measurements and constraints for reionization, early structure formation, and early chemical enrichment. Observations of bright QSOs with luminosities $\gtrsim 10^{47}$ erg s^{-1} at $z \gtrsim 6$ suggest that SMBHs as massive as

10^9 $M_\odot$ have already been assembled when the universe was less than 1 billion years old (Fan, 2006; Willott et al., 2010; Mortlock et al., 2011; Wu et al., 2015).

The most pressing question is "how did these high-redshift SMBHs form in such a short time?". Assuming that a non-spinning black hole grows at the Eddington accretion limit starting from a relatively small mass ($\lesssim 10^2$ $M_\odot$), it would take 700 Myr for the growth of a "light" seed into the observed SMBHs at $z \sim 6$. For spinning black holes, radiative efficiencies are 20–30% higher, limiting the accretion rate and would take an additional 250 Myr (Thorne, 1974; Gammie et al., 2004). Black hole seeds are thought to have a common origin from metal-free (Population III; Pop III) massive stars and can be placed in the following categories:

1. the remnant from typically massive (10–100 $M_\odot$) Pop III stars (Madau & Rees, 2001; Volonteri & Rees, 2006);

2. the collapse of dense stellar clusters (Davies et al., 2011);

3. the direct collapse of a gaseous metal-free cloud into a supermassive star ($M \sim 10^5$ $M_\odot$) (Bromm et al., 2003; Wise et al., 2008; Begelman et al., 2006; Volonteri et al., 2008).

Also a combination of these seeding mechanisms may be possible.

1.1.1 Population III Star Remnants

Pop III stars, sometimes called the "first stars", have large characteristic masses on the order of 30–100 $M_\odot$ and form in dark matter (mini-)halos with masses $\sim 10^6$ $M_\odot$ at redshift $z \sim 20$. Electronic transitions in atomic hydrogen and helium only become efficient coolants at $\sim 10^4$ K, but gas in these minihalos cannot heat to such temperatures as they virialize (Bromm et al., 1999; Abel et al., 2002; Yoshida et al., 2006). The most efficient

coolant therefore is molecular hydrogen (H_2). Massive Pop III stars have surface temperatures of 10^5 K, generating enough energetic photons to completely ionize their host halos and start the process of cosmic reionization (Bromm et al., 2001; Bromm & Loeb, 2004; Glover, 2005). Pop III stars with masses $20 - 140$ $M_\odot$ and $\gtrsim 260$ $M_\odot$ are expected to directly collapse into black hole remnants, possible providing the seeds of the first quasars (Madau & Rees, 2001; Heger et al., 2003; Ricotti & Ostriker, 2004). It is also possible that more massive black holes form after the epoch of the first stars in larger halos with virial temperatures $T \sim 10^4$ K that corresponds to a mass of $\sim 10^8$ $M_\odot$ (Spaans & Silk, 2006; Begelman et al., 2006).

In order for light Pop III ($M \sim 100$ $M_\odot$) remnant black holes to be the seeds of $z \sim 6$ quasars, the accretion must extremely fast and near the Eddington limit. Simulations have shown that they do not grow rapidly immediately after their formation (Haiman & Loeb, 2001; Kitayama et al., 2004; Alvarez et al., 2006). Radiation feedback from the first stars heats the gas in the host halo, quenching any possible cold and dense gas that would possibly fall into the black hole. Any further accretion must be accomplished through mergers of other halos, providing fresh cold gas to the host halo (Ricotti & Ostriker, 2004; Kuhlen & Madau, 2005).

The black hole accretion rate can be estimated through the so-called Bondi-Hoyle rate, which assumes a point mass growing from a medium with uniform density and temperature. This rate is given by

$$\frac{dM}{dt} \sim \frac{2\pi G^2 m_{\rm H} n_{\rm H}}{c_{\rm s}^3} M^2 \tag{1.1}$$

where M is the black hole mass, $m_{\rm H}$ and $n_{\rm H}$ are the hydrogen mass and number density, $c_{\rm s}$ is the sound speed (Bondi, 1952). Assuming that the seed originates from a Pop III star and has a mass of 100 $M_\odot$ and is embedded in a gas with $T = 1000$ K, it would take ~800 Myr for it to reach 10^9 $M_\odot$, that is nearly the age of the universe at $z \sim 6$ (Bromm & Loeb, 2004). Meanwhile, as the black hole evolves, radiative feedback keeps the gas densities

low and the temperatures elevated, even taking into account cosmological accretion. Simulations have shown that accretion rates of these light seeds barely reach the Eddington limit (Johnson et al., 2007). Therefore, the light seed route toward a high-redshift SMBH faces an early challenging bottleneck of a hostile (warm and diffuse) accretion environment.

The stellar endpoints leading to BH formation are indicated in Fig. 1.1. Primordial stars with masses in the range $40 - 140$ $M_\odot$ and above 260 $M_\odot$ are expected to directly collapse into BHs of similar masses (Heger & Woosley, 2002; Heger et al., 2003). For a trace amount of metals, all stars above 40 $M_\odot$ directly collapse into a BH, but these stars also lose an increasing amount of mass through winds as metallicities increase. The fraction of massive stars collapsing into BHs depends on the shape of the initial mass function (IMF) of the first stars. Although numerical simulations suggest that some Pop III stars might be rotating as fast as ~ 1000 km s^{-1}, close to their break-up limit (Stacy et al., 2011), stellar evolution models that include rotational effects indicate that stellar winds from such metal-free stars is still very low when compared to metal-enriched stars. Thus Population III stars with low rotational speeds are favored for the formation of the most massive light black hole seeds because they retain most of their initial mass until they collapse into black holes (Ekström et al., 2008).

1.1.2 Collapse from Dense Clusters

Gravitational collapse of dense star clusters provides another viable mechanism for generation of massive black holes, since we do know that dense star clusters do exist, they are often produced in regions of active star formation. Moreover, it has been known for a long time that the dynamical evolution of any star cluster, with stars of different individual masses, will be characterized by a contracting core and an expanding envelope, leading to a mass-segregation instability (Spitzer, 1969). Such a phenomenon brings slowly this stellar system towards the core collapse, which can occur even in the absence of the mass

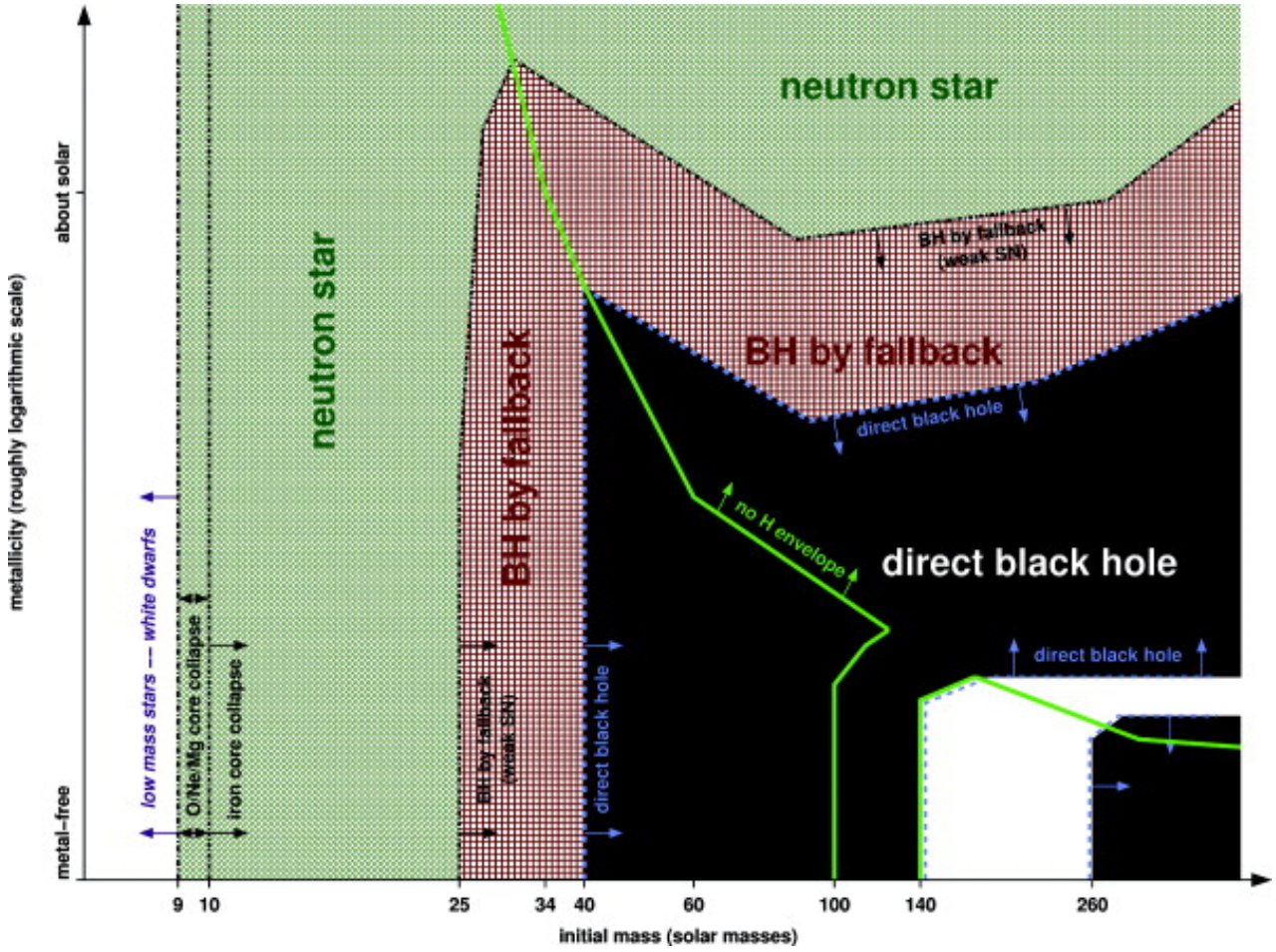

Figure 1.1: Remnants of massive single stars as a function of initial metallicity (y-axis; qualitatively) and initial mass (x-axis). The thick green line separates the regimes where the stars keep their hydrogen envelope (left and lower right) from those where the hydrogen envelope is lost (between 100 to 140 $M_{\odot}$). The dashed blue line indicates the border of the regime of direct black hole formation (black). This domain is interrupted by a strip of pair-instability supernovae that leave no remnant (white). The tracks for the formation of direct black holes from the stars are highlighted by the black color while the white region in the bottom right indicates the range for a pair instability supernova. Adopted from Heger et al. (2003).

segregation (Antonov, 1962; Hénon, 1965). Such an evolution is directly related to high stellar number densities, while cluster cores may and do collapse, they can be stabilized by binaries and not continue all the way to black hole formation (Heggie, 1975).

The process of a cluster catastrophically collapsing has been studied by various groups that focus on the runaway merging of the most massive stars, especially in young clusters (Shapiro, 2004). Also, among old clusters, the growth of a massive black hole could be seeded as globular clusters merge (Kawakatu & Umemura, 2005). Both of the mechanisms could have, in the present day, produced massive black hole remnants in present-day globular clusters and, at high redshift, could have produced black hole seeds in galaxy centers. The expected masses of such cluster collapse black hole seeds are in the range $10^2 - 10^4$ $M_\odot$, which are also potential starting points for high-redshift SMBHs (O'Leary et al., 2006; Davies et al., 2011).

1.1.3 Direct Collapse Black Hole Seed

Given the difficulties experienced by light black hole seeds produced by typical Pop III stars and dense stellar clusters, the best possible seeding scenario is that they started even more massive. The direct collapse black hole scenario envisions a primordial gas cloud that collapses without fragmentation into a single object. This formation sequence occurs in halos where atomic cooling efficient but cannot cool through molecules or metals, otherwise the gas would fragment and form a stellar cluster. As the gas cloud contracts, it could be slowed by rotational support, as it possesses some specific angular momentum that originates from tidal torques from the nearby cosmological matter distribution (Loeb & Rasio, 1994; Bromm & Loeb, 2004; Lodato & Natarajan, 2006; Wise et al., 2008).

In the direct collapse scenario, which is the focus of this thesis, halos with a virial temperature $T_{\rm vir} \simeq 10^4$ K ($M_{\rm vir} \gtrsim 10^8$ $M_\odot$ at $z \sim 10$), known as atomic cooling halos, that are chemically pristine and have a very low molecular hydrogen density can catastrophi-

cally collapse (Rees & Ostriker, 1977; White & Frenk, 1991). The cooling associated with direct collapse occurs at such a virial temperature because the atomic hydrogen ionization and collisional de-excitation rates increase by several orders of magnitude. To quantify the scale of cooling, we define the cooling time as,

$$t_{\rm cool} = \frac{3kT}{n\Lambda(T)} \tag{1.2}$$

where T is the cooling temperature and $\Lambda(T)$ is the cooling rate. By applying this definition to the virial temperature and density radial profile, we can determine at which radius, named the cooling radius $r_{\rm cool}$, the interior material is able to cool within a Hubble time (Rees & Ostriker, 1977). Describing a gravitational collapsing is free-fall dynamic time

$$t_{\rm ff} = \sqrt{4\pi G\rho} \tag{1.3}$$

The ability for a gas cloud to cool is directly related to its collapse, namely, the ratio of $t_{\rm cool}$ to the gravitational free-fall time $t_{\rm ff}$. For a collapsing halo, the general collapse criterion is that the cooling time of the gas is less than the free-fall time, i.e. $t_{\rm cool} \lesssim t_{\rm ff}$. For the cooling radius to satisfy this condition, the collapse proceeds on a free-fall timescale, unimpeded by gas pressure. Any gas outside the cooling radius, which has already been shock-heated to the virial temperature during virialization, would not have had time to radiatively cool its gravitational energy, remaining essentially unchanged thereafter.

Numerical simulations have indeed shown that fragmentation is inefficient when H_2 cooling is absent. However, in most models, the absence of H_2 was assumed, rather than derived. The absence of H_2 molecules from protogalactic halo gas can be justified by a sufficiently intense UV radiation, which is usually provided by an H_2 photodissociating (Lyman-Werner; LW) background. The relevant criterion is that the photodissociation timescale is shorter than the H_2 formation timescale. For a collapsing halo with virial tem-

perature $T_{\rm vir} < 10^4$ K, the gas cannot cool in the absence of H_2, the densities remain low and H_2 can be dissociated even by a relatively feeble UV flux. The critical value of the LW background is found to be $J_{21} \sim 0.1$. Here J_{21} is the background specific intensity in units of 10^{-21} erg s^{-1} cm^{-2} Hz^{-1} sr^{-1} at the Lyman limit (13.6 eV). The critical intensity J_{21} is much higher in more massive collapsing halos, with virial temperatures $T_{\rm vir} \gtrsim 10^4 K$. The associated gas inside such halos proceeds to collapse monolithically and isothermally without fragmentation when the LW background has $J_{21} \gtrsim 10^3$ given a 10^5 K blackbody spectral shape. The gas in these halos can cool via excitations of atomic H and reach much higher densities, at which point, the H_2 molecules can then become self-shielding from the LW radiation and can cool. (e.g. Omukai, 2001; O'Shea & Norman, 2008; Shang et al., 2010; Wolcott-Green & Haiman, 2012; Agarwal & Khochfar, 2015; Glover, 2015).

Fragmentation during collapse is highly suppressed when H_2 cooling is absent (Bromm et al., 2003; Regan & Haehnelt, 2009). The Jeans mass describes the critical point at which a gaseous cloud becomes gravitationally unstable and begins to collapse as it lacks sufficient thermal pressure support to balance the force of gravity. For the direct collapse black hole seed, the Jeans mass can be written as,

$$M_{\rm J} \simeq 10^{5.5}\ {\rm M}_\odot \left(\frac{T}{10^4\ {\rm K}}\right)^{3/2} \left(\frac{n}{10^4\ {\rm cm}^{-3}}\right)^{-1/2}, \tag{1.4}$$

where n is the baryon number density. This value determines the approximate fragment mass during the collapse and is a key characteristic quantity to follow during this phase. The gas temperature T depends highly on whether radiative cooling is efficient, that is mainly determined by the H_2 fraction in a metal-free gas. When it is efficient, the temperature $T \sim 300$ K, corresponding to $M_{\rm J} \sim 10^3$ M$_\odot$, implying that the cloud will fragment into Pop III stars. Prior to reionization, the LW background is not sufficiently high to affect all atomic cooling halos (Visbal et al., 2014a), but there is a small possibility that such a pre-galactic halo has a nearby neighboring galaxy that boosts the impinging LW radiation above

a critical J_{21} value (e.g. Dijkstra et al., 2008; Agarwal et al., 2014; Visbal et al., 2014b; Regan et al., 2016, 2017). Without H_2 cooling, atomic hydrogen transitions allow the gas to cool to 8000 K but no further, resulting in a central Jeans mass $M_{\rm J} \sim 10^5 - 10^6$ $M_\odot$, that has the possibility of collapsing into a dense stellar cluster or supermassive star, ultimately producing a massive black hole on the order of $M \simeq 10^4 - 10^5$ $M_\odot$.

Because the strength of the impinging LW radiation plays an important role in direct collapse black hole formation, we further discuss the sources of LW radiation. The overall background that prevents H_2 cooling in minihalos ($T_{\rm vir} \lesssim 10^4$ K) was likely established by the massive Pop III stars that had formed in previous generations of minihalos. In this case, the background spectrum is likely to be closer to the 10^5 K scale, implying $J_{21} \gtrsim 10^3$. Furthermore, early minihalos hosting Pop III stars are easily self-ionized with most of their LW radiation escaping into the intergalactic medium, quantified by the LW escape fraction $f_{\rm esc,LW} \sim 1.0$ (Kitayama et al., 2004; Whalen et al., 2004). If we see $f_{\rm esc,LW} \ll 1.0$, the mean UV background is unlikely to reach the required critical value. The LW radiation field will have spatial fluctuations, and a very small fraction of 10^4 K halos that have an unusually close and bright neighboring galaxy, providing a sufficiently high flux to the direct collapse black hole host halo. The cosmological clustering of first generations of high-redshift halos suggest that $\sim 10^{-6}$ of halos will have a nearby bright neighbor, which has been termed the "close pair" scenario (Dijkstra et al., 2008).

1.2 Theory and Observations of Lyman-Alpha Radiation

The Lyman series is the set of radiative transitions in the hydrogen atom that arise when the electron goes from an excited state ($n \geq 2$) to the ground state ($n = 1$). The first line in the spectrum of the Lyman series - named Lyman-α (hereafter, Lyα) - was discovered in 1906 by Theodore Lyman, who was studying the ultraviolet spectrum of electrically excited hydrogen gas. The rest of the lines of the spectrum were discovered by Lyman in

subsequent years.

Lyman alpha is the resonant line corresponding to the energy difference between the ground state and the first excited state of neutral hydrogen. This is the most famous transition in the early Universe, and because atomic hydrogen is the main constitute of the primordial halos, the Lyα line is often the most prominent line emerging from astrophysical objects, especially in the formation of SMBHs. In the following sections, the various physical processes that may result in emission of Lyα will be discussed. In a nutshell, the Lyα photons are produced around the formation and main sequence of massive stars within dense baryonic halos.

Lyα lines have been used for detection of young galaxies (Partridge & Peebles, 1967). This method was based on the assumption that ionizing photons that are emitted by young, newly formed stars are efficiently reprocessed into recombination lines which contains a large amount of Lyα photons. Moreover, we can expect to observe structure formation from a Lyα emission afterglow. Galaxies are surrounded by vast reservoirs of gas that are capable of both emitting and absorbing Lyα radiation. Except for the direct observation of galaxies, spatially extended Lyα nebulae provide insight into the formation and evolution of galaxies (Furlanetto et al., 2005). Currently, the observations that focus on Lyα line have been an ideal candidate of identifying new targets, including Hobby-Eberly Telescope Dark Energy Experiment (HETDEX) which has increased the sample of Lyα emitting galaxies by orders of magnitude at $z \sim 2 - 4$ (Hill et al., 2008); Subaru's Hyper Suprime-Cam (HSC) which will provide a similar boost out to $z \sim 7$ (Aihara et al., 2017); Integral field unit spectrographs such, as MUSE (Bacon et al., 2010), and also the Keck's Cosmic Web Imager instrument (Martin et al., 2014) that have mapped out spatially extended Lyα emission down to $\sim$10 times lower surface brightness levels than before and have taken spatially resolved spectra.

1.2.1 Astrophysics Sources of Lyα Radiation

Lyα emitters (LAEs) are simply galaxies observed in Lyα, achieved either through spectroscopy or through narrow-band imaging with ground-based observations generally yielding high-redshift LAEs (Cowie & Hu, 1998; Fynbo et al., 2001; Nilsson & Meisenheimer, 2009). Narrowband imaging has the advantage that many LAE candidates can be found simultaneously, but to investigate a non-vanishing volume of space the width of the filter cannot be too small, and thus the redshift determination is not very accurate. Spectroscopically confirmed LAEs cannot only pinpoint their redshift precisely, but also make sure that an object is in fact an LAE and not an lower energy line emitting strongly at another wavelength. Common contaminators are Lyβ and OII/OIII emitters located at lower redshifts.

Several physical processes may result in the emission of Lyα photons, but can in most cases be divided into recombinations following the ionization of the hydrogen, or collisions with other atoms. When we refer to LAEs in the scale of galaxies, we list four main candidates below.

Reprocessed UV radiation: The most significant source to Lyα radiation in young galaxies is hydrogen recombination following ionization by the UV radiation from massive Pop III stars. At the onset of star formation, UV radiation from the hot and massive stars will ionize the surrounding neutral hydrogen gas. When the protons and electrons recombine, a fraction of the recombinations will result in the emission of a Lyα photon. If the UV photon has more energy than the Lyα transition, it may excite a hydrogen atom. In the end, the result will be an atom excited to the first excited state. In this case, if the hydrogen atom is in $2s$ state, the excited atom will emit two photons instead, having recombination with an intermediate and temporary state. Quantum mechanics does not allow radiative transitions between just any two quantum states and these radiative transitions must obey the "Hund's rules." Otherwise the atom will be spontaneously in $2p$ state and emit a Lyα photon. At

$T = 10^4$ K, ultimately 68% of the recombinations are accompanied by the emission of a Lyα photon. This fraction is only mildly sensitive to temperature, e.g. at 5×10^3 K (2×10^4 K) the fraction is 70% (64%) (Spitzer, 1978).

Gravitationally heated gas: The gravitational collapse of primordial baryonic halo into the deep potential wells created by mostly dark matter. As the gas becomes more dense or optically thick, atomic collisions becomes more dominant force to lose the potential energy, the temperature will be heated up to 10^5 K scale, which cools by collision and emits Lyα photons, in a nutshell, the potential energy of the gas is released as cooling radiation. The Lyα radiation makes up to 50% of the total gas radiation by a baryonic haloes with temperature $T \sim 2 \times 10^5$ K at high redshifts when the metallicities are low.

Ultraviolet radiation background: UV radiation that is not absorbed in the galaxy will escape into the intergalactic medium and be incorporated into the UV radiation background. Cosmic reionization occurs gradually between $z = 6 - 15$, mainly from radiation originating from primordial galaxies, and in the process, a substantial fraction of neutral gas in these galaxies is photo-ionized. When the optical depth of neutral hydrogen (HI) region is small ($\ll 1$), the UV background will propagate through the medium without many absorption and associated recombination events. However, when the HI optical depth becomes high enough ($\gg 1$), the gas in dark matter halos are known as damped Lyα absorbers (DLAs). At these column densities, the damping wings of the Lyα absorption line profile becomes strong (Furlanetto et al., 2005). The Lyα radiation generated from the UV background consists a very small portion compared those from massive stars, but the radiative processes are the same, in which the neutral hydrogen atom is photo-ionized or photo-excited and then emits a photon after recombination or de-excitation, respectively.

Lyα blobs: A special type of LAEs are known as Lyα blobs (LABs) that have extremely large sizes ($\gtrsim 100$ kpc) and high luminosities ($\gtrsim 10^{43}$ erg/s). LABs have been discovered for the better part of two decades now (Fynbo et al., 1999; Nilsson et al., 2006). Since they exhibit little or no continuum radiation, the possible mechanics behind the emission could be cooling radiation similar to the ionized environments around massive stars or ones caused by the UV background. Meanwhile, other sources, such as quasars and strong galactic outflows, have been used to explain these objects. Some galaxies proceed through a phase in their early life in which gas accreting onto a central SMBH, creating an AGN. It then injects tremendous amounts of energy through two jets along the axis of rotation. These jets may then further ionize surrounding gas, possibly producing Lyα radiation (Haiman & Rees, 2001).

1.2.2 Lyman-Alpha Emission Mechanism

A hydrogen atom emits a Lyα photon once its electron is in the $2p$ state and decays to the ground state. In this section, we illustrate quantitatively how radiative photons are generated through this process.

Collisional De-excitation

This process happens when a electron collides with a neutral hydrogen atom. When the electron enters the effective potential of the atom, there will be electromagnetic radiation emitted and a portion of it belongs to the Lyα line. The radiation strength of this collisional cooling depends on both the relative and absolute velocity of the two particle system and also depends on the number densities of both electrons and neutral hydrogen atoms. The velocity distribution of electrons and atoms are uniquely determined by the temperature of

the medium. Thus the radiation energy of collisional de-excitation is,

$$\eta_{\rm dcol} = n_{\rm e} n_{\rm HI} A_{\rm 1s2p}(T) \tag{1.5}$$

where $n_{\rm e}$ and $n_{\rm HI}$ are the respective number densities of electrons and neutral atomic hydrogen, and $A_{\rm pq}(T)$ is the de-excitation rate between levels p and q at a temperature T. In general, the de-excitation rate can be denoted as

$$A_{\rm pq} = \frac{h^2}{(2\pi m_{\rm e})^{3/2}(k_{\rm B}T)^{1/2}} \frac{\langle \Omega_{\rm pq} \rangle}{g_{\rm p}} exp(-\frac{\Delta E_{\rm pq}}{k_{\rm B}T}) \tag{1.6}$$

Here h is the Planck constant; $m_{\rm e}$ is the electron mass; $k_{\rm B}$ is the Boltzmann constant; $g_{\rm p}$ is the degeneracy of level p; $\Delta E_{\rm pq}$ is the energy difference between the levels p and q; $\langle \Omega_{\rm pq} \rangle$ is the velocity averaged collision strength. The velocity averaged collision rate can be solved straightforwardly through the following sequence. We can expand this expression to the total radiation strength of collisional radiation with the rate expression becoming

$$\eta_{\rm dcol,all} = n_{\rm e} n_{\rm HI} C(T), \tag{1.7}$$

where

$$C(T) = \sum_{q} A_{\rm 1s\rightarrow q} \Delta E_{\rm 1s\rightarrow q}. \tag{1.8}$$

We now sum up all the energies of the excited states. Among all the hydrogen electronic states, Lyα contributes the most to the total radiation energy, which approximately accounts for 60% of the energy budget at $T \sim 10^4$ K. In this thesis, we adopt the analytic fitting result from Black (1981):

$$C(T) = 7.5 \times 10^{-19} (1 + T_5^{1/2})^{-1} e^{-(118348\ {\rm K})/T}\ {\rm erg\ cm^3\ s^{-1}}, \tag{1.9}$$

where $T_5 \equiv T/(10^5\ {\rm K})$. Fig. 1.2 shows that the cooling curve increases dramatically

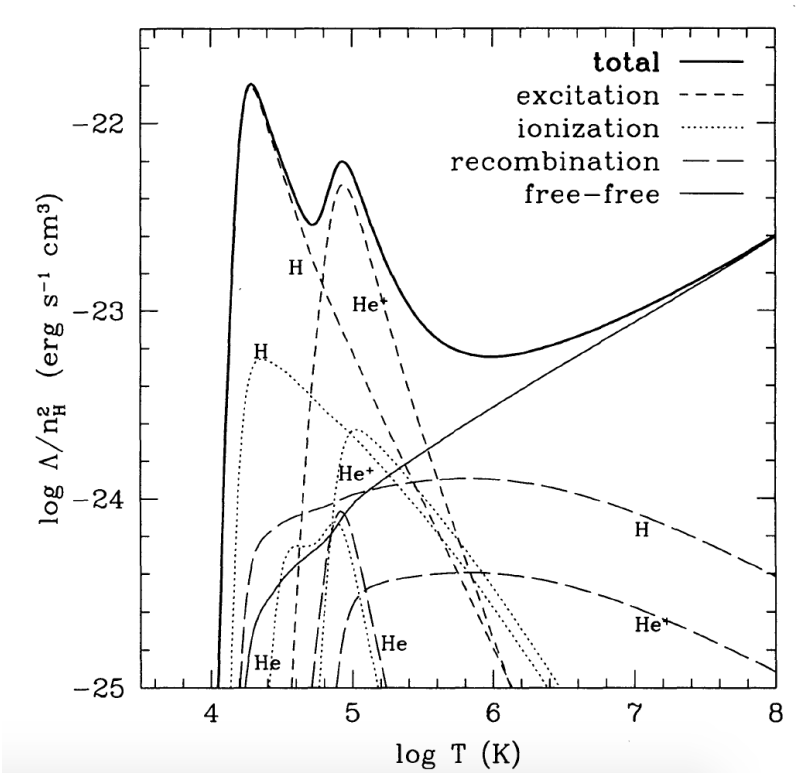

Figure 1.2: The temperature dependence of the primordial cooling rate under the assumption of collisional ionization equilibrium. After $\log T \sim 4.2$, the collisional ionization of hydrogen removes most of the neutral hydrogen that eliminates the collisional excitation cooling channel. Starting at $\log T \sim 4.6$, the collisional ionization of helium dominates over helium. Adopted from Thoul & Weinberg (1995).

around $T \sim 10^4$ K, which is due to the corresponding increase in C(T). The maximum rate occurs at $\log T \sim 4.2$ when the hydrogen ionization rate reaches a maximum, and at higher temperatures, the neutral hydrogen fraction decreases substantially, eliminating this cooling channel.

Recombination

In a pure hydrogen gas with a nonzero ionized fraction, protons will capture the free electrons at some rate. A fraction of the captured free electrons will decay into the ground state through a cascade, producing a Lyα photon in the process. As a result, if the recombined hydrogen atom is in the p state, the probability of generating Lyα photon is the summation with intermediate state q,

$$P(p \rightarrow \mathrm{Ly}\alpha) = \sum_q P(p \rightarrow q) P(q \rightarrow \mathrm{Ly}\alpha) \tag{1.10}$$

where $P(p \rightarrow q)$ is the transition probability of both direct and indirect transfers from level p to level q. As the Hund's rules permit radiative cascades from a quantum state p to quantum state q, this probability is given by,

$$P(p \rightarrow q) = \frac{A_{\mathrm{pq}}}{\sum_{p'q'} A_{\mathrm{p'q'}}} \tag{1.11}$$

Here A_{pq} is the Einstein A coefficient. For a single recombination emission process, free electrons can undergo transitions to bound states by emission of a photon,

$$H^+ + e^- \rightarrow H_{\mathrm{excited},nl} + h\nu, \tag{1.12}$$

where the electron is captured into some specific state nl that was initially unoccupied. The cross-section for electron capture via this "radiative recombination" process is σ_{nl}. Thus

the recombination rate coefficient α_{nl} for electron capture directly to level nl, with the energy difference E from the ground state level, is

$$\alpha_{nl} = \left(\frac{8kT}{\pi m_{\rm e}}\right)^{1/2} \int_0^\infty \sigma_{nl}(E) \frac{E}{(kT)^2} e^{-E/kT}\, dE \tag{1.13}$$

If the region under consideration has a significant amount of neutral hydrogen, the recombination photon will have a very high probability of being absorbed by another hydrogen atom shortly after this emission with a proton created as a by-product. Therefore, aside from the transport of the ionization energy an extremely short distance, a recombination directly to the ground state under these circumstances has virtually no effect on the ionization state of the gas. Baker & Menzel (1938) proposed two distinguished limits.

Case A: When the gas is optically thin to ionizing radiation, every ionizing photon emitted during the recombination process escapes. For this case, we sum the recombination rate coefficients α_{nl} over all levels nl.

Case B: When the gas is optically thick to radiation just above 13.59 eV, ionizing photons emitted during recombination are immediately reabsorbed, creating another ion and free electron by photoionization. In this case, the recombinations directly to $n = 1$ do not reduce the ionization of the gas, and only recombinations to $n \geq 2$ act to reduce the ionization.

The effective radiative recombination rates for hydrogen for these two limiting cases are thus

$$\begin{aligned} \alpha_{\rm A}(T) &= \sum_{n=1}^{\infty} \sum_{l=0}^{n-1} \alpha_{nl}(T) \\ \alpha_{\rm B}(T) &= \sum_{n=2}^{\infty} \sum_{l=0}^{n-1} \alpha_{nl}(T) = \alpha_{\rm A}(T) - \alpha_{1s}(T) \end{aligned} \tag{1.14}$$

After numerically calculating the recombination coefficients, the two rates can be fitted in the following function forms in the temperature range $30K \leq T \leq 3 \times 10^4$ K

$$\begin{aligned} \alpha_{\rm A}(T) &= 4.13 \times 10^{-13} T_4^{-0.7131-0.0115\ \ln(T4)}\ {\rm cm}^3\ {\rm s}^{-1} \\ \alpha_{\rm B}(T) &= 2.54 \times 10^{-13} T_4^{-0.8163-0.0208\ \ln(T4)}\ {\rm cm}^3\ {\rm s}^{-1}, \end{aligned} \tag{1.15}$$

where $T_4 \equiv T/(10^4\ {\rm K})$. In the spectrum of the Case B recombination, the Lyα and Lyβ are two strongest lines. The rate coefficients for recombinations that result in emission of these lines can be approximated by

$$\begin{aligned} \alpha_{{\rm Ly}\alpha}(T) &= 1.17 \times 10^{-13} T_4^{-0.942-0.031\ \ln(T4)}\ {\rm cm}^3\ {\rm s}^{-1} \\ \alpha_{{\rm Ly}\beta}(T) &= 3.03 \times 10^{-14} T_4^{-0.874-0.058\ \ln(T4)}\ {\rm cm}^3\ {\rm s}^{-1}. \end{aligned} \tag{1.16}$$

These approximations are accurate to within $\sim$2% for $0.1 < T_4 < 3$. Now we turn back to Lyα photons only. The probability that an arbitrary recombination event results in a Lyα photon is

$$P({\rm Ly}\alpha) = \sum_{n=2}^{\infty} \sum_{l=0}^{n-1} \frac{\alpha_{nl}(T)}{\alpha_{\rm tot}(T)} P(n, l \rightarrow {\rm Ly}\alpha). \tag{1.17}$$

For the Case B recombination which we consider in our work on the direct collapse black hole scenario, the probability $P({\rm Ly}\alpha) = 0.68$ at $T = 10^4$ K.

1.3 Lyman-Alpha Radiation Resonant Scattering

Here we discuss the basic properties of the Lyα resonant scattering, basically covering the diffusion process and the spectral properties.

1.3.1 Lyman-Alpha Scattering Cross-Section

We first describe the classical derivation of the cross-section of Lyα absorption by evaluating the magnitude of the cross-section. We first determine the spatial distribution of radiation and also the spectrum of the emergent photons.

Considering the case of a neutral hydrogen atom, we treat the system as a dipole, i.e. a harmonic oscillator. In the lab frame, the initial frequency of the atom is ω_0 and the incoming photon has the frequency ω. When the photon enters the system, the damped harmonic oscillator satisfies the equation of motion,

$$\ddot{x} + \Gamma\dot{x} + \omega_0^2 x^2 = \frac{e}{m_{\rm e}} E_0 \exp(i\omega t) \tag{1.18}$$

Here we use x to denote the spatial displacement of the electron in the lab frame. The equation of motion can be solved as

$$x = \frac{eE_0}{m_{\rm e}} \frac{1}{\omega^2 - \omega_0^2 + i\omega\Gamma} \tag{1.19}$$

By applying the Larmor formula, the average radiation power after the hydrogen atom absorbs the photon is

$$\langle P_{\rm out} \rangle = \frac{2e^2\langle \ddot{x} \rangle^2}{3c^3} = \frac{e^4\omega^4 E_0^2}{12c^3 m_e^2 \omega_0^2} \frac{1}{(\omega - \omega_0)^2 + \Gamma^2/4}. \tag{1.20}$$

The electromagnetic wave incoming flux is $\langle F_{in} \rangle = c^2 E_0^2 / 8\pi$. Therefore, we can calculate the absorbing cross-section as

$$\begin{aligned} \sigma(\omega) &= \frac{\langle P_{\rm out} \rangle}{\langle F_{\rm in} \rangle} = \frac{8\pi \langle P_{\rm out} \rangle}{cE_0^2} \\ &= \frac{2\pi e^4 \omega^4}{3m_e^2 \omega^2 c^4} \frac{1}{(\omega - \omega_0)^2 + \Gamma^2/4} \end{aligned} \tag{1.21}$$

Substituting the photon frequency into this equation, we obtain a Lorentzian profile, indicating that Lyα absorbing cross-section is frequency dependent,

$$\sigma(\mu) = \sigma_0 \frac{(\Gamma/2\pi)^2(\mu/\mu_0)^4}{(\mu-\mu_0)^2 + \Gamma^2/16\pi^2}, \tag{1.22}$$

where we have used $\mu \equiv \omega$ to consistent with the literature. Here $\sigma_0 = (3/8\pi)(2\pi c/\omega_0)^2 \simeq 7 \times 10^{-11}$ cm^{-2} is the Thomson scattering cross-section.

We now focus on the quantum viewpoint instead of the classical derivation to get more insight. Only if the photon energy matches closely the energy difference $E_f - E_i$ between the initial state i and final state f of the hydrogen atom, it is in resonance and has a large probability of exciting the electron. For the Lyα transition, $i = 1s$ and $f = 2p$.

Now we consider a system with a neutral hydrogen atom residing in a electromagnetic field. For an electron with position operator x in a time varying electromagnetic field with scalar and vector potentials $\Phi(x,t)$ and $A(x,t)$, the Hamiltonian is,

$$H = \frac{1}{2m_\mathrm{e}}\left[p + \frac{e}{c}A(x,t)\right]^2 - e\Phi(x,t), \tag{1.23}$$

where $p = -i\hbar\nabla$ is the momentum operator. In order to solve the equation of motion, we use the Coulomb gauge here with $\nabla \cdot A = 0$, and we therefore have the updated Hamiltonian as

$$\begin{aligned} H &= \frac{1}{2m_\mathrm{e}}p^2 + e\Phi + \frac{e}{2m_\mathrm{e}c}A\cdot p + \frac{e^2}{2m_\mathrm{e}c^2}A\cdot A \\ &= H_0 + H_1 + H_2 \end{aligned} \tag{1.24}$$

Here $H_0 = (1/2m_\mathrm{e})p^2 + e\Phi$ is the original unperturbed Hamiltonian that only consists of a proton and an electron with the perturbation terms $H_1 = (e/2m_e c)A \cdot p$ and $H_2 = (e^2/2m_\mathrm{e}c^2)A \cdot A$ that represent the interactions of the electron and the electromagnetic field and the Hamiltonian of the field itself. Generally, we have $H_0 \gg H_1 \gg H_2$. In the

weak field limit, it is appropriate to neglect the H_2 term that only represents the field itself.

Because we are dealing with the quantum system's interaction with the wave, it is better to consider the Fourier transform of the fields

$$A(x,t) = \int a(k)e^{i(kx-\omega t)} + a^{\star}(k)e^{-i(kx-\omega t)}d^3k, \tag{1.25}$$

where the $\star$ indicates the Fourier transfer. By considering the Coulomb gauge, we have $k \cdot a = 0$. We can thus further decompose it within the polarization surface with the directions $\hat{e}_1$ and $\hat{e}_2$. The newly decomposition description is now

$$A(x,t) = \int \left[\sum_{i=1,2} \hat{e}_i(k) \left(a_i(k)e^{i(kx-\omega t)} + a_i^{\star}(k)e^{-i(kx-\omega t)} \right) \right] d^3k, \tag{1.26}$$

where $a_i(k)$ and $a_i^{\star}(k)$ represent the polarization decomposition.

We now describe the electromagnetic field that has a Hamiltonian of

$$H_{\text{rad}} = \int h_{\text{rad}} dV = \frac{1}{8\pi} \int (|E|^2 + |B|^2) dV \tag{1.27}$$

where h_{rad} is the Hamiltonian density while E and B is the time- and spatially-dependent electric and magnetic fields. By utilizing Maxwell's induction equation

$$\begin{aligned} E &= -\frac{1}{c}\frac{\partial A}{\partial t} \\ B &= \nabla \times A \end{aligned} \tag{1.28}$$

and substituting the result into the radiation field Hamiltonian, we have

$$h_{\text{rad}} = \frac{1}{2\pi} \int \sum_{i=1,2} |a_i(k)|^2 k^2 d^3k. \tag{1.29}$$

In terms of the spectrum, denoted by the occupation number $N(k)$, the Hamiltonian density

satisfies $h_{\mathrm{rad}} = \int \sum_{i=1,2} \hbar\omega N_i(k) d^3k$, so that we have

$$a_i(k) = c\left(\frac{hN_i(k)}{\omega}\right)^{1/2}. \tag{1.30}$$

The perturbation Hamiltonian density h_1 in the continuum limit thus has the form

$$h_1 = \frac{1}{2\pi^3}\sum_{i=1,2}\int (h_i^{\mathrm{abs}}(k)e^{-i\omega t} + h_i^{\mathrm{em}}e^{i\omega t})d^3k, \tag{1.31}$$

where

$$h_i^{abs} = \frac{e}{m_{\mathrm{e}}}\left[\frac{h}{\omega}N_1(k)\right]^{1/2} e^{ikx}\hat{e}_i(k)\cdot p \tag{1.32}$$

is the Hamiltonian decomposition density representing absorption. The Hamiltonian density representing the radiation field is described by

$$h_i^{\mathrm{em}} = \frac{e}{m_{\mathrm{e}}}[\frac{h}{\omega}(1+N_1(k))]^{1/2}e^{ikx}\hat{e}_i(k)\cdot p. \tag{1.33}$$

We now have $h = h_0 + h_1$, where h_1 is not explicitly dependent on time t, i.e. $\partial H_1/\partial t = 0$. As a result, we can use typical perturbation theory from quantum mechanics to this system. We know that h_0 has the eigenfunction

$$\Psi_j(x,t) = \phi_j(x)e^{-iE_jt/\hbar}, \tag{1.34}$$

where E_j is the eigenenergy value of j-th eigenstate $\phi_j(x)$, which is time independent because $\partial H_0/\partial t = 0$. With the weighting function $c_j(t)$, the unperturbed function of the whole system is now

$$\Psi(x,t) = \sum_j c_j(t)\phi_j(x)e^{-iE_jt/\hbar} \tag{1.35}$$

Given the initial condition $\Psi(x, t \le 0) = \sum_p b_p\phi_i(x)$, we have $c_j(t \le 0) = b_j$. Consider-

ing first order perturbation theory, we arrive at the expression

$$c_f(t) = -\frac{i}{\hbar}\sum_p \int_0^t \langle f|H_1|p\rangle \exp(i\omega_{fp}t)dt \tag{1.36}$$

We now focus only on the absorption part of the process, the transition probability for an electron absorbing a photon can be derived with the previous equation, which yields the probability magnitude of absorbing a photon with frequency ω, described by

$$c_f(k,t) = \frac{1}{\hbar^2}|\langle f|h_i^{\rm abs}|p\rangle|^2 \frac{\sin^2[(\omega-\omega_{fp})/2]}{[(\omega-\omega_{fp})/2]^2} \tag{1.37}$$

where the frequency $\omega = ck$. To get the total transition probability, we integrate over the k-space and sum over the polarization i to obtain

$$P_f = \left(\frac{e}{2\pi m_{\rm e}}\right)^2 \sum_{i=1,2;j} b_j \int \frac{N_i(k)}{\hbar\omega}|\langle f|e^{ikx}\hat{e}_i(k)\cdot p|j\rangle|^2 \frac{\sin^2[(\omega-\omega_{fp})/2]}{[(\omega-\omega_{fp})/2]^2}\frac{\omega^2}{c^3}d\omega d\Omega, \tag{1.38}$$

where $d^3k = k^2\,dk\,d\Omega = (\omega^2/c^3)\,d\omega\,d\Omega$, assuming we start with $b_j = \delta_{fj}$. In the limit of time going to large values, we will have the probability P_j strongly peaked, so that the transition will eventually occur.

The transition rate probability between level i and level f is then

$$\frac{dP_{if}}{dt} = \sum_{i=1,2}\int \omega_i\,d\Omega, \tag{1.39}$$

where ω_i is the probability of a transition starting from the i state. To solve for the transition rate, we adopt the dipole approximation, where $kx \ll 1$ so that we can evaluate e^{ikx} as

unity[1]. We now can evaluate $|\langle f|e^{ikx}\hat{e}_i(k)\cdot p|j\rangle|$ with $p = im_e[H_0, x]/h$,

$$\frac{dP_{if}}{dt} = \frac{e^2}{hc^3}\sum_{i=1,2}\int \left[N_i\omega^3|\hat{e}_i\cdot x_{fi}|\right]_{fi} d\Omega, \tag{1.40}$$

where

$$\begin{aligned}\hat{e}_1\cdot x_{fi} &= |x_{fi}|\sin\theta\cos\phi\\ \hat{e}_2\cdot x_{fi} &= |x_{fi}|\sin\theta\sin\phi\end{aligned} \tag{1.41}$$

For an unpolarized field, we have $N_1 = N_2 = N(\omega)/2$, giving

$$\frac{dP_{if}}{dt} = \frac{4\pi}{3}\frac{e^2}{hc^3}N(\omega_{fi})\omega_{fi}^3|x_{fi}|. \tag{1.42}$$

However, we desire to find the transition rate as a function of frequency. The bound cross-section is defined as

$$\sigma_\omega = \frac{4\pi^2}{3}\frac{e^2}{\hbar c}|x_{fi}|^2\omega\delta(\omega-\omega_{fi}). \tag{1.43}$$

The absorption transition probability is then an integral over frequency

$$\frac{dP_{if}}{dt} = \int_0^\infty \sigma_\omega c N(\omega)\frac{4\pi\omega^2}{(2\pi)^3c^3}\,d\omega. \tag{1.44}$$

Now we return to the cross-section result derived in classical scenario (Equation 1.22). In order to quantify the "friction parameter" Γ, we consider the oscillator strength parameter f_{if} that is related to the Einstein A-coefficient through $f_{if}\Gamma = A_{if}$. The classical cross-section is then

$$\sigma_\mu = \frac{\pi e^2}{m_e c}f_{ij}\phi_{ij}(\mu) \tag{1.45}$$

where $\phi_{ij}(\mu)$ is the normalized line profile of the corresponding transition. By comparison,

[1]This is a good approximation for UV radiation as we can safely neglect retardation effects across the atom. However, this becomes inadequate for more energetic X-ray radiation.

we thus have

$$\phi_{if}(\mu) = 2\pi\mu\delta(\mu - \mu_{if}), \tag{1.46}$$

and we can calculate the oscillator parameter

$$f_{if} = \frac{2m_{\rm e}}{3\hbar}\omega_{fi}|x_{fi}|^2. \tag{1.47}$$

In the above calculation, however, the line profile was taken to be a delta function. But since emission processes compete with absorption processes, the absorption rate is affected by the transition rate for spontaneous emission, in which the atom decays to the ground state again. Generally, we refer here absorption and re-emission as the same case of resonant scattering. For spontaneous emission, $N(\omega) = 1$, the Einstein A-coefficient is

$$A_f = \frac{dP_{if}}{dt}\frac{d}{dt}|c_f|^2 = -A_f|c_f|^2 \tag{1.48}$$

where i is the initial state. Thus we have the following new expression for the cross-section with the derivation of $\dot{c}_f(t)$,

$$\sigma_\omega = \frac{4\pi^2}{3}\frac{e^2}{\hbar c}|x_{fi}|^2\omega_{fi}L(\omega), \tag{1.49}$$

and the Lorentzian profile associated with the natural line profile also results from this approach,

$$L(\omega) = \frac{1}{\pi}\frac{A_f/2}{(\omega - \omega_{fi})^2 + (A_f/2)^2}. \tag{1.50}$$

This profile is characterized by a sharp peak of width A_f centered at ω_{fi}.

We now consider the fine structure of hydrogen, calculating the transition probability for the transition (n', l', m') to (n, l, m), where n, l and m are the respective quantum

numbers. To evaluate $\langle f|x|i\rangle$, here we denote $|f\rangle$ as,

$$|f\rangle = |nlm\rangle = R_{nl}(r)Y_l^m(\theta,\phi), \tag{1.51}$$

where $R_{nl}(r)$ and $Y_l^m(\theta,\phi)$ are the radial wave-function and spherical harmonic functions, respectively. To solve for the expectation value, we utilize the directions of polarization that can be expressed in terms of spherical harmonics as

$$\begin{aligned} z &= \left(\frac{4\pi}{3}\right)^{1/2} r\, Y_1^0 \\ x \pm iy &= \left(\frac{8\pi}{3}\right)^{1/2} r\, Y_1^{\pm 1}. \end{aligned} \tag{1.52}$$

For the Lyα transition, $|21m'\rangle \rightarrow |100\rangle$, there are three possible values of m'. However, they all result in the same value

$$|\langle|21m'|x|100\rangle|^2 = \frac{2^{15}}{3^{10}}a_0^2, \tag{1.53}$$

where $a_0 = (\hbar^2/m_{\rm e}c^2)$ is the Bohr radius. The transition rate is then evaluated as

$$A_{\rm Ly\alpha} = 6.25 \times 10^8 \text{ s}^{-1}. \tag{1.54}$$

As a result, we arrive at a key result, the half surviving time of the excited state,

$$t_{1/2} = \frac{1}{A_{\rm Ly\alpha}} = 1.60 \times 10^{-9} \text{ s}. \tag{1.55}$$

This is a really short timescale, meaning that we can nearly neglect the time spent in the excited state of a hydrogen atom. For the transitions from $|200\rangle$, the forbidden transition has the half-life eight orders of magnitude larger than the Lyα line. The most probable decay is thus through an intermediate state of opposite parity with the emission of two

photons as result.

To make this result more useful, we denote the frequency uncertainty as $\Delta\nu_{\rm L} = 2\pi/t_{1/2}$, giving the natural frequency width

$$\delta\mu_L = 9.936 \times 10^{-7}\ \mathrm{s}^{-1}. \tag{1.56}$$

The absorption cross-section σ_μ for the Lyα transition is finally given by

$$\sigma_\mu = f_{12}\frac{\pi e^2}{m_{\rm e}c}\frac{\Delta\nu_L/2\pi}{(\nu-\nu_0)^2 + (\Delta\nu_{\rm L}/2)^2}, \tag{1.57}$$

where $\mu_0 = 2.466 \times 10^{15}$ Hz is the intrinsic line frequency of the Lyα transition.

1.3.2 Voigt Profile

The result obtained in the last section gives the probability distribution function for a hydrogen atom absorbing a photon of frequency ν. However, so far it was assumed that the scattering atom is at rest. If the atom is moving with a velocity $v_{\rm H}$, then the re-emitted (scattered) photon will be Doppler shifted based on the relative velocity between the atom reference frame and lab frame. The first order approximation of the Doppler shift for radiation gives an updated frequency

$$\nu' = \nu(1 - \frac{\hat{n}v_{\rm H}}{c}), \tag{1.58}$$

where $\hat{n}$ is the unit vector of the incident photon. From statistical point of view, the velocity of the atom can be categorized into two aspects: macroscopic and microscopic. The macroscopic velocity is related to the bulk velocity of the baryonic matter. These are usually caused by the infall velocity components, tangential velocity components, and various turbulent motions. Numerical or analytical models of astrophysical objects can provide

the velocity. Microscopic velocities are related to the temperature and pressure of the gas. The microscopic effect of the random velocity is determined by the random thermal motions of the atoms and molecules. For gas at some temperature T, these velocities follow a Maxwellian distribution that is a Gaussian distribution in three mutually perpendicular directions. This velocity distribution results in dispersion of

$$\begin{aligned} v_{\rm th} &= \left(\frac{2k_{\rm B}T}{m_{\rm H}}\right)^{1/2} \\ &= 12.85T_4^{1/2}\ {\rm km\ s^{-1}}, \end{aligned} \tag{1.59}$$

where $k_{\rm B}$ is the Boltzmann constant, $m_{\rm H}$ is the atomic mass of hydrogen, and $T_4 \equiv T/(10^4\ {\rm K})$. The associated Doppler frequency shift $\Delta\nu{\rm D}$ distribution is then

$$\begin{aligned} \Delta\nu_{\rm D} &= \frac{v_{\rm th}}{c}\nu_0 \\ &= 1.057\times10^{11}T_4^{1/2}\ {\rm s^{-1}} \end{aligned} \tag{1.60}$$

To simplify the following expressions, we denote the frequency as a frequency shift x relative to the line center,

$$x \equiv \frac{\nu-\nu_0}{\Delta\nu_{\rm D}}. \tag{1.61}$$

The thermal line profile is then expressed by

$$G(x) = \frac{1}{\sqrt{\pi}}e^{-x^2}, \tag{1.62}$$

and the natural line profile is given by

$$L(x) = \frac{a}{\pi}\frac{1}{x^2+a^2}, \tag{1.63}$$

where

$$\begin{aligned} \Delta\nu_{\rm L} &= \frac{2\pi}{t_{1/2}} \\ a &= \frac{\Delta\nu_{\rm L}}{2\Delta\nu_{\rm D}}. \end{aligned} \tag{1.64}$$

We refer to a here as the relative damping width. We now define Voigt profile in the reference frame in which the gas is, on average, at rest, and the resulting profile is a convolution of a Lorentzian and a Gaussian profile,

$$\begin{aligned} \mathcal{V}(x) &= \int_{-\infty}^{\infty} L(x-y)G(y)\,dy \\ &= \frac{1}{\sqrt{\pi}\Delta\nu_D} H(a,x). \end{aligned} \tag{1.65}$$

Here the Voigt function $H(a,x)$ is

$$H(a,x) \equiv \frac{\tau_x}{\tau_0} = \frac{a}{\pi}\int_{-\infty}^{\infty} dy \frac{e^{-y^2}}{(y-x)^2+a^2} \simeq \begin{cases} e^{-x^2} & (\text{core}) \\ a/(x^2\sqrt{\pi}) & (\text{wing}) \end{cases}. \tag{1.66}$$

The core and wings approximations are accurate in their relevant regimes. Since the profile functions $L(x)$ and $G(x)$ are normalized to unity, the convolution will conserve normalization, i.e. $\int_{-\infty}^{\infty}\mathcal{V}(x)\,dx = 1$. The final result for the cross-section of the hydrogen atom in thermal equilibrium is

$$\sigma(x) = f_{\rm Ly\alpha}\frac{\sqrt{\pi}e^2}{m_{\rm e}\,c\,\Delta\nu_{\rm D}} H(a,x). \tag{1.67}$$

The Voigt function at all frequencies is given simply by the sum of the following two terms, $\phi(x) \sim e^{-x^2} + a/(x^2\sqrt{\pi})$. We note that this approximation fails in a very narrow frequency regime where the transition from the core to wing occurs. A useful fitting function that is accurate at all x is explored in Tasitsiomi (2006).

One of the key results from this derivation is that the Lyα cross-section, evaluated at

the line center and averaged over the velocity distribution of atoms, is $\sigma(T) = 5.9 \times 10^{-14} T_4^{-1/2}$ cm^2, which is nearly 11 orders of magnitude larger than the Thomson cross-section. Thus an electron bound to a proton is 11 orders of magnitude more efficient at scattering radiation than a free electron when the frequency of that radiation closely matches the natural frequency of the transition.

1.3.3 Scattering Radiation

Frequency Shifting

Lyα photons traveling through a gaseous medium can be absorbed and subsequently re-emitted with slightly a different energy. Generally, the scattering is coherent in the reference frame of the atom. As in the lab frame, any motion of the atom will add a Doppler shift to the photon. We quantify the velocity of the atom in terms of the thermal velocity,

$$u \equiv \frac{v_{\rm atom}}{v_{\rm th}} \tag{1.68}$$

If we assume the relative frequency of a Lyα photon in the lab frame is x (Equation 1.61), then the frequency in the atom's frame is then

$$x_{\rm sc} = x_{\rm in} - u \cdot \hat{n}, \tag{1.69}$$

where $\hat{n}$ is the original photon direction unit vector. Thus the frequency after the scattering is

$$x_{\rm out} = x_{\rm in} - u_{\rm in} \cdot \hat{n}_{\rm int} + u_{\rm out} \cdot \hat{n}_{\rm out}. \tag{1.70}$$

The atomic recoil effect is important when considering a frequency change. The momentum of the photon may not be conserved in the atom's frame if it were not for the newly acquired momentum of the hydrogen atom itself. This acquired momentum corresponds

to an added kinetic energy, which in turn came at the expense of the energy of the Lyα photon. The energy of the Lyα photon is therefore not conserved exactly, but reduced by a small amount in each scattering event. When the original and the re-emission directions are same or exactly opposite, the momentum will however be conserved. As a result, this will give an additional term to the frequency of the photon as

$$x_{\rm out} = x_{\rm in} - u_{\rm in} \cdot \hat{n}_{\rm int} + u_{\rm out} \cdot \hat{n}_{\rm out} + g(\mu - 1), \tag{1.71}$$

where $g = E_{\rm Ly\alpha}/m_{\rm H}v_{\rm th}c = 2.6 \times 10^{-4} T_4^{-1/2}$ is the fractional energy transfered to the atom per scattering. The loss of energy is also related to the azimuthal angle μ. We note that the recoil effect results in a change of $\sim 10^{-4}$ of the total energy, and this is negligible compared to the back-reaction "drag" force. The probability distribution function of a Lyα photon with frequency $x_{\rm out}$ after entering the atom with frequency $x_{\rm in}$ and angle μ is

$$P(x_{\rm out}|x_{\rm in}, \mu) \propto \int_{-\infty}^{\infty} du \int_{-\infty}^{\infty} dw P(x_{\rm out}|\mu, x_{\rm in}, u, w) P(u|\mu, x_{\rm in}) P(w|\mu, x_{\rm in}), \tag{1.72}$$

where $u = v_\parallel/v_{\rm th}$ and $w = v_\perp/v_{\rm th}$. Since $P(x_{\rm out}|\mu, x_{\rm in}, u, w)$ is non-zero only if $w = [x_{\rm out} - x_{\rm in} + u(1-\mu)]/\sqrt{1-\mu^2}$, we arrive at the PDF

$$P(x_{\rm out}|x_{\rm in}, \mu) \propto \int_{-\infty}^{\infty} du \int_{-\infty}^{\infty} P(u|\mu, x_{\rm in}) P(w|\mu, x_{\rm in})\, dw. \tag{1.73}$$

The scattering probability of Lyα photons off atoms with velocity component u must proportional to the cross-section we derived above, $P(x_{\rm in}|u) \propto A_\alpha/\{[\omega(x_{\rm in} - u)v_{\rm th}/c]^2 + A_\alpha^2/4\}$. With Bayes law, $P(u|x_{\rm in}) = P(x_{\rm in}|u) \times P(u)/P(x_{\rm in})$. We can denote the probability as

$$P(x_{\rm out}|x_{\rm in}, \mu) \propto \int_{-\infty}^{\infty} du \int_{-\infty}^{\infty} \frac{e^{-u^2}}{(x_{\rm in} - u)^2 + a_{\rm v}^2} \exp\left\{ - \left[\frac{\Delta x - u(\mu - 1)}{\sqrt{1-\mu^2}} \right]^2 \right\} dw \tag{1.74}$$

where $a_{\rm v} = A_\alpha c/2\omega v_{\rm th}$. In this radiative transfer problem, we are mostly interested in the conditional PDF $P(x_{\rm out}|x_{\rm in})$. We thus need to calculate the so-called phase function $P(\mu|x_{\rm in})$. We know that the scattering must always be isotropic in the azimuthal direction and hence independent of ϕ. It is determined by the multipole order of the emitted radiation and the difference in total angular momenta J of the initial, intermediate and final states of the scattering system. With the dipole approximation, the phase function is given by

$$P(\mu) \propto 1 + p_{\rm J}\mu^2 \tag{1.75}$$

where $p_{\rm J}$ is the degree of polarization for perpendicular scattering. The initial and final state of the scattering events are ground states while the intermediate is the excited state. For hydrogen atoms, the spin quantum number is $s = \pm 1/2$ and the total angular momentum $J = l + s$, which is always $1/2$ for the ground state. The first excited state, the total angular momentum can either be $J = 1/2$ or $J = 3/2$. The three first excited states are $2S_{1/2}$, $2P_{1/2}$ and $2P_{3/2}$. For the state of $2S_{1/2}$, the photon is scattered through two photon mechanism. For the state of $2P_{1/2}$, where $J = 1/2$,

$$J = \frac{(2J-1)(2J+3)}{12J^2 + 12J + 1} = 0. \tag{1.76}$$

So there is no polarization for the $J = 1/2$ case. While for the $2P_{3/2}$ state that has $J = 3/2$

$$J = \frac{(J+1)(2J+3)}{26J^2 - 15J - 1} = \frac{3}{7}. \tag{1.77}$$

As a result, the normalized phase function for the two cases are

$$\begin{aligned} P_{2P_{1/2}}(\mu) &= \frac{1}{2} \\ P_{2P_{3/2}}(\mu) &= \frac{7}{16}\left(1 + \frac{3}{7}\mu^2\right) \end{aligned} \tag{1.78}$$

The scattering is not the same when the Lyα photon resides in the wing part of the scattering line. The derived probability distributions above are only valid in the core part of the line profile. The scattering in the wing part behaves more like oscillator scattering (Rayleigh), which is a dipole distribution for the phase function (Stenflo, 1980). The normalized phase function at wing part is

$$P_{\rm wing}(\mu) = \frac{3}{4}(1+\mu^2) \tag{1.79}$$

Thus we have the isotropic and dipole scattering which relates to $2P_{1/2}$ and $2P_{3/2}$ states at core and dipole at wing part. Now consider if the photon is at the wing part with the frequency $x_{\rm in}$ before one scattering event, we would like to know the recoil effect of the scattering. The expected change of frequency is,

$$\begin{aligned}\langle \Delta x | x_{\rm in}\rangle &= \int_{-\infty}^{\infty} \Delta x P(x_{\rm out}|x_{\rm in}) dx_{\rm out} \\ &= \frac{1}{2}\int_{-\infty}^{\infty} dx_{\rm out} \int_{-1}^{1} d\mu\, \Delta x P(\mu) P(x_{\rm out}|\mu, x_{\rm in})\end{aligned} \tag{1.80}$$

By substituting the above equations into the expectation value for frequency change, we obtain

$$\begin{aligned}\langle \Delta x | x_{\rm in}\rangle =& \frac{a_{\rm v}}{2\pi^{3/2}\phi(x_{\rm in})} \int_{-1}^{1} \frac{d\mu}{\sqrt{1-\mu^2}} \int_{-\infty}^{\infty} du\, \frac{e^{-u^2}}{(x_{\rm in}-u)^2 + a_{\rm v}^2} \times \\ & \int_{-\infty}^{\infty} d(\Delta x) \exp\left\{ -\left[\frac{\Delta x - u(\mu-1)}{\sqrt{1-\mu^2}}\right]^2 \right\} \Delta x\end{aligned} \tag{1.81}$$

where $a_{\rm v}/2\pi^{3/2}\phi(x_{\rm in})$ is the normalization factor, and we make a substitution of $\Delta x = x_{\rm out} - x_{\rm in}$. Since we are interested in the temperature range of $T = 10^3 - 10^5$ K, it is

appropriate to assume that $x_{\rm in} \gg 1$, that is $x_{\rm in} \gg u$, resulting in

$$\begin{aligned}
\langle \Delta x | x_{\rm in} \rangle &= -\frac{a_{\rm v}}{\pi \phi(x_{\rm in})} \int_{-\infty}^{\infty} du \, \frac{u e^{-u^2}}{(x_{\rm in} - u)^2} \\
&= -\frac{a_{\rm v}}{\pi \phi(x_{\rm in}) x_{\rm in}^2} \int_{-\infty}^{\infty} du \, u e^{-u^2} \left(1 + 2\frac{2}{x_{\rm in}} \right) \\
&= -\frac{2a_{\rm v}}{\pi \phi(x_{\rm in}) x_{\rm in}^3} \frac{\sqrt{\pi}}{2} \\
&= -\frac{1}{x_{\rm in}}
\end{aligned} \tag{1.82}$$

Here we used the line profile of the wing part, which is $\phi(x) = a_{\rm v}/(x^2\sqrt{\pi})$. This is quite instructive as it implies that when a Lyα photon is far in the wing part, the resonant scattering exerts a restoring force which pushes the photon back to line center. This restoring force generally overwhelms the energy losses resulting from atomic recoil we mentioned above, which is $\Delta x = -2.6 \times 10^{-4}\, T_4^{-1/2}$. The transition boundary between the core to the wing part is when the two profiles from Voigt profile equal each other, described by the following equality

$$\begin{aligned}
\frac{1}{\sqrt{\pi}} e^{-x^2} &= \frac{a_{\rm v}}{\pi x^2} \\
x(a_{\rm v}) &= 1.59 - 0.60 \log a_{\rm v} - 0.03 \log^2 a_{\rm v}.
\end{aligned} \tag{1.83}$$

This expression is useful when calculating the properties of the scattering event.

1.3.4 Radiation Transport

We now describe the general case of radiation transport, which is a extremely mature field in astrophysics. For the radiative transfer through a medium with a neutral hydrogen number density $n_{\rm H}$, the radiation intensity I satisfies the condition

$$\begin{aligned}
d\tau &= n_H \sigma_{\rm x} \, dr \\
dI &= -I \, d\tau,
\end{aligned} \tag{1.84}$$

where τ is the optical depth with the cross-section $\sigma_{\rm x}$ for frequency x. When integrated through a certain path with optical depth τ, the radiation intensity is attenuated as

$$I(\tau) = I_0 e^{-\tau}, \tag{1.85}$$

where I_0 is the initial intensity. The escaping fraction is thus $p(\tau) = 1 - e^{-\tau}$.

For a general case, we define $I_\nu(\vec{r}, \hat{n}, \nu, t)$ as the energy crosses a unit area A, per solid angle Ω, per unit time t by a photon with energy $h\nu$ in the direction $\hat{n}$, which can be written down as

$$I_\nu(\vec{r}, \hat{n}, \nu, t) = h\nu \frac{d^3 N_\nu}{d\Omega\, dt\, A}, \tag{1.86}$$

where N_ν is the photon distribution at some frequency ν. The radiation transfer equation describes the dynamics of the transport mechanisms,

$$\begin{aligned} n \cdot \nabla I_\nu(\vec{r}, \hat{n}, \nu, t) + \frac{1}{c}\frac{\partial I_\nu(\vec{r}, \hat{n}, \nu, t)}{\partial t} = -\alpha_\nu(\vec{r}) I(\vec{r}, \nu, t) + j_\nu(\vec{r}, \hat{n}, \nu, t) + \\ \int d\nu' \int d^3\hat{n}' \alpha_{\nu'} I_{\nu'}(\hat{r}, \hat{n}', \nu, t) P(\nu, \hat{n}|\nu', \hat{n}') \end{aligned} \tag{1.87}$$

Here $\alpha_\nu I(\vec{r}, \nu, t)$ denotes the attenuation of the radiation that corresponds to the energy loss by absorption by neutral hydrogen atom. For a small region, the local polarization of absorption can be neglected, and we can assume α_ν is isotropic. The emission coefficient $j_\nu(\vec{r}, \hat{n}, \nu, t)$ represents the newly generated photons due to spontaneous emission and collisional excitation per solid angle per unit volume. The last term in the right hand side represents resonant scattering of photons, which is the main process contributing to the Lyα radiation field. $P(\nu, \hat{n}|\nu', \hat{n}')$ is the redistribution function that describes the probability of radiation that was originally propagating in the direction $\hat{n}$ and frequency ν being scattered into another direction n' and frequency ν'.

In the case of Lyα transfer, the attenuation coefficient is mainly composed by the ab-

sorption of neutral hydrogen, which is denoted as

$$\alpha_\nu(\vec{r}) = \left(n_{1s} - \frac{g_{1s}}{g_{2p}} n_{2p} \right) \sigma(\mu). \tag{1.88}$$

In practice, we can simply state that $\alpha_\nu(r) = n_{1s}\sigma(\mu)$ because the number density of excited hydrogen atom is negligible with respect to the ground state when the temperature of $T \leq 2 \times 10^5$ K. For the emission coefficient, we can express it as an isotropic Voigt profile, corresponding to the generation of Lyα photons,

$$j_\nu(\vec{r}) = \frac{\phi(\nu) h\nu}{4\pi^{3/2}\Delta\nu} \left[n_{\rm e} n_{\rm H} A_{\rm 1s2p} + n_{\rm e} n_{\rm HII} \alpha(T) f_{\rm Ly\alpha}(T) \right], \tag{1.89}$$

where $\phi(\nu)$ is the Voigt profile. The first term in the bracket is the collisional de-excitation and the second is the Lyα recombination.

By assuming $\nabla I_\nu(\vec{r}, \hat{n}, t) = 0$ meaning that the local radiation of Lyα photons is isotropic, we can analyze the scattering of Lyα as a diffusion process. We define the angle averaged intensity as $J_\nu = \frac{1}{4\pi} \int d\Omega \, I_\nu(\hat{n})$. We also replace the displacement ds by the optical depth with $d\tau = n_{\rm H}\sigma_\nu \, ds$. We now can write the radiation transfer equation as

$$\frac{\partial J(x)}{\partial \tau} = -\phi(x) J(x) + S_{\rm x}(\tau) + \int dx' \phi(x') J(x') P(x|x'), \tag{1.90}$$

where $S_x(\tau) = j_{\rm x}(\tau)/n_{\rm H}\sigma_{\rm x}$ is the source function expressed in terms of optical depth τ instead of displacement s.

The Eddington approximation is used when the radiation field is nearly isotropic everywhere. Assuming that the transfer from other line frequencies are from wing part, we can obtain the approximation for the integration as a Taylor series

$$\int dx' J(x') P(x|x') = J(x) - \frac{1}{x}\frac{dJ(x)}{dx} + \frac{1}{2}\frac{d^2 J(x)}{dx^2} + \cdots \tag{1.91}$$

Now the angular averaged intensity $J(\tau, x)$ satisfies the diffusion equation in the form of partial differential equation as

$$\frac{\partial^2 J}{\partial \tau^2} + \frac{\partial^2 J}{\partial \sigma^2} = -\frac{3\phi(x)}{4\pi} S_{\rm x}(\tau) \tag{1.92}$$

Here $\sigma = \sqrt{2/3}\int_0^x dx'/\phi(x')$. Analytic solutions to this transfer equation are only available for systems with particular symmetries. For convenience, we can initially define the source as a delta function with the frequency at $x = x_0$.

First let us consider the radiation transfer of photons emitted by a planar source that exists between two parallel slabs of gas. Lyα photons are emitted with arbitrary initial frequency in a non-absorbing medium, and the solution (Neufeld, 1990) is then given by

$$J(\tau_0, x) = \frac{\sqrt{6}x^2}{24\sqrt{\pi}a_{\rm v}\tau_0} \frac{1}{\cosh[\sqrt{\pi^3/54}(x^3 - x_0^3)/(a_{\rm v}\tau_0)]}, \tag{1.93}$$

where τ_0 is the half optical depth of the slab. From the solution of the intensity function, it can be inferred that the effects of gas temperature and the photon frequency are relatively independent.

Consider another case in which photons originate from the center of a uniform sphere. This spherically symmetric medium has a emergent intensity as (Dijkstra et al., 2006)

$$J(\tau_0, x) = \frac{\sqrt{\pi}x^2}{4\sqrt{6}a_{\rm v}\tau_0} \frac{1}{1 + \cosh[x^3\sqrt{2\pi^3/27}/(a_{\rm v}\tau_0)]}. \tag{1.94}$$

In this case, photons are assumed to be emitted at the line center, i.e. $x_0 = 0$. The maximum intensity occurs at $x_{\rm max} = \pm 0.92(a_{\rm v}\tau_0)^{1/3}$. While all these configurations are highly ideal and intuition can be gained from them, a realistic young galaxy environment may be highly disordered, where the gas velocities are spatially varying, impacting the Lyα photon frequencies through the Doppler shift.

For most systems, we are interested to know how many Lyα photons escape the system's outer boundary. In order to calculate this value, the average number of scattering events a single photon experiences before leaving the system is a key quantity. We first need to determine the average scattering number as a function of frequency x. We notice the average frequency shift is $\langle \Delta x \rangle = 1/x$. The expected number for a photon in the wing to scatter before returning to the core is therefore x^2. Thus the average number of scattering events is

$$P_{\rm scat} = 2 \int_{x_{\rm max}}^{\infty} \frac{\phi(x)}{x^2}\, dx \propto \frac{a_{\rm v}}{x_{\rm max}^3} \tag{1.95}$$

where $x_{\rm max} \propto \tau_0^{1/3}$ is the peak frequency of the spectrum emerging from the sphere. We then have $N_{\rm scat} = 1/P_{\rm scat} \propto \tau_0$. For the slab case, the average number is $N_{\rm scat} \sim 1.1\tau_0$, and $N_{scat} \sim 0.6\tau_0$ for the sphere case (Dijkstra et al., 2006).

Furthermore, we can calculate the expectation time of a photon escaping the system. We now know that photons escape in a single excursion after many scattering events at a peak frequency $x_{\rm max}$. During this excursion, the photon scatter $x_{\rm max}^2$ times in the wing of the line profile. We also know it takes $N_{\rm scat} \sim \tau_0$ scattering events on average before the excursion begins. The vast majority of scattering events thus occur in the line core, where the mean free path is very short. The total distance (in units of the light-crossing time of the system) that the photon traveled while scattering in the line core is

$$L_{\rm core} \sim \tau_0 \cdot \tau_0^{-1} \sim 1, \tag{1.96}$$

while in the wing, the distance traveled before escaping is

$$L_{\rm wing} \sim x_{\rm max}^2 \times [\tau_0 \phi(x_{\rm p})]^{-1} = \frac{x_{\rm max}^4 \sqrt{\pi}}{a_{\rm v}\tau_0} = x_{\rm max}. \tag{1.97}$$

Combining these two distances, the photon travels a total distance of

$$L_{\rm total} = L_{\rm core} + L_{\rm wing} \sim 1 + x_{\rm max} \sim x_{\rm max} \tag{1.98}$$

before escaping the system, showing that Lyα photons are highly constrained to their origin before scattering and Doppler shifting out of the line core.

CHAPTER 2

NUMERICAL METHODS

The main results of this thesis uses numerical simulations to study the development of SMBH seeds and the propagation of Lyα photons in such systems. In this chapter, we will first focus on the massively-parallel hydrodynamics code Enzo, which we use to conduct cosmological simulations on the formation of SMBH seeds, which consists of collapse of primordial gas clouds in dark matter halos and one-zone cooling test models. We then describe the details of Lyα radiation Monte Carlo calculations performed on these simulated data.

2.1 Enzo

For simulations to follow the high spatial and temporal ranges in a cosmological setting, various numerical techniques have been developed that can be broadly split into gridless, Lagrangian methods and grid-based, Eulerian schemes. The first type known as Smoothed Particle Hydrodynamics (SPH Lucy, 1977; Gingold & Monaghan, 1977). The SPH method has resulted in many successful studies, especially with N-body simulations of dark matter large-scale structure. However, with an increasing number of sought-after physical processes being considered, there are many drawbacks of SPH, which cannot be captured within this scheme. The other type uses a Eulerian grid-based hydrodynamic scheme (Laney, 1998; Colella & Woodward, 1984). To follow compact and high-density regions in a system, numerical methods can adaptively increase the spatial and temporal resolution in small volumes of the simulation, known as Structured Adaptive Mesh Refinement (SAMR), introduced by Berger & Colella (1989). The main principle is to adaptively add

and modify additional finer meshes over regions that require higher resolution.

During the last 30 years, the AMR framework have been continuously developed with many additional features. There have been several numerical astrophysical codes that use SAMR. The N-body solver developed by Villumsen (1989) used non-adaptive mesh to increase the resolution in pre-selected regions. This static approach was later used extensively when applied to hydrodynamics (Ruffert, 1994). Later there were numbers of codes developed with adaptive meshing (Couchman, 1991; Jessop et al., 1994; Truelove et al., 1998; Yahagi & Yoshii, 2001; Ziegler, 2005; Zhang & MacFadyen, 2006; Cunningham et al., 2009; Mignone et al., 2012; Almgren et al., 2013). There are several codes that are currently used among the community. FLASH is the most comparable to Enzo and is widely used (Fryxell et al., 2000) that uses grid blocks of fixed size. RAMSES (Fryxell et al., 2000) and ART (Kravtsov et al., 1997) are two more AMR codes that are widely used in cosmological simulations. Moreover, an unstructured grid approach based on a moving Voronoi mesh are now adopted with the newer codes, such as AREPO and TESS (Springel, 2010; Duffell & MacFadyen, 2011).

In this thesis, we used the SAMR code Enzo that is a popular and robust in simulating various astrophysical systems. Enzo was originally developed for cosmological hydrodynamical simulations and is in general an effective tool for general astrophysical problems. Enzo has proved to be efficient, accurate and easily extendable. Several methods papers have covered most of the numerical methods and as well as various extension and performance tests (Bryan et al., 1995; Bryan & Norman, 1997; O'Shea et al., 2004; Norman et al., 2007; Wang et al., 2008; Reynolds et al., 2009; Collins, 2010; Wise & Abel, 2011). Over the last two decades, there are over 400 publications using Enzo. It is able to simulate a number of astrophysical systems including galaxies (Tassis et al., 2003; Lackner et al., 2012), galaxy clusters (Loken et al., 2002; Xu et al., 2011), the interstellar medium (Slyz et al., 2005), the intergalactic medium (Fang & Bryan, 2001; Smith et al., 2011), the cir-

cumgalactic medium (Hummels et al., 2013), cooling flows (Li & Bryan, 2012), turbulence (Kritsuk & Norman, 2004; Collins et al., 2011), the formation of the first stars (Abel et al., 2002; O'Shea & Norman, 2007; Xu et al., 2008; Turk et al., 2009), and the formation of stars in our own Galaxy (Collins et al., 2011, 2012). The Enzo code has been able to overcome many drawbacks which SPH codes cannot solve, where the AMR simulations can effectively resolve the physical models.

2.1.1 Physics Equations

The Eulerian equations of ideal magnetohydrodynamics (MHD) including gravity, in a comoving coordinate system incorporating with the cosmological expansion, are given by

$$\begin{aligned}
\frac{\partial \rho}{\partial t} + \frac{1}{a}\nabla \cdot (\rho v) &= 0, \\
\frac{\partial \rho v}{\partial t} + \frac{1}{a}\nabla \cdot (\rho v v + I p^* - \frac{BB}{a}) &= -\frac{\dot{a}}{a}\rho v - \frac{1}{a}\rho \nabla \phi \\
\frac{\partial E}{\partial t} + \frac{1}{a}\nabla \cdot [(E + p^*)v - \frac{1}{a}B(B \cdot v)] &= -\frac{\dot{a}}{a}(2E - \frac{B^2}{2a}) - \frac{\rho}{a} v \cdot \nabla \phi \\
&\quad - \Lambda + \Gamma + \frac{1}{a}\nabla \cdot F_{\mathrm{cond}} \\
\frac{\partial B}{\partial t} - \frac{1}{a}\nabla \times (v \times B) &= 0
\end{aligned} \tag{2.1}$$

where E, ρ, v, and B are the comoving total fluid energy density, comoving gas density, peculiar velocity, and comoving magnetic field strength, respectively. The matrix I is the identity matrix, and a is the cosmological expansion parameter. The first equation represents conservation of mass, the second conservation of momentum, and the third conservation of total fluid energy. They are respectively, the first, second, and third moments of the Boltzmann equation. The fourth equation is the magnetic induction equation. Other symbols are radiative cooling Λ, heating Γ and thermal heat conduction F_{cond} rates. The comoving fluid energy E, the comoving thermal energy e, the comoving isotropic pressure

p^*, and the gravitational potential are given by

$$\begin{aligned} E &= e + \frac{\rho v^2}{2} + \frac{B^2}{2a} \\ e &= \frac{p}{\gamma - 1} \\ p^* &= p + \frac{B^2}{2a} \\ \nabla^2 \phi &= \frac{4\pi G}{a}(\rho_{\mathrm{total}} - \rho_0), \end{aligned} \tag{2.2}$$

where ρ_0 is the mean density of the medium and γ is the parameter for the equation of state. The evolution of a is governed by the Friedmann equation

$$\frac{\ddot{a}}{a} = -\frac{4\pi G}{3a^2}\left(\rho_0 + \frac{3p_0}{c^2}\right) + \frac{\Lambda c^2}{3}. \tag{2.3}$$

Any collisionless components (such as dark matter and stars) are modeled with particles, whose dynamics are governed by Newton's equations in comoving coordinates,

$$\begin{aligned} \frac{dx}{dt} &= \frac{1}{a}v \\ \frac{dv}{dt} &= -\frac{\dot{a}}{a}v - \frac{1}{a}\nabla\phi. \end{aligned} \tag{2.4}$$

Enzo can also solve the mass conservation equations for a set of chemical species and their reactions. For any species i with comoving number density n_{i}, the equations are in the form

$$\frac{\partial n_{\mathrm{i}}}{\partial t} + \frac{1}{a}\nabla \cdot (n_{\mathrm{i}} v) = \sum_{\mathrm{j}} k_{\mathrm{ij}}(T) n_{\mathrm{i}} n_{\mathrm{j}} + \sum_{\mathrm{j}} \Gamma_{\mathrm{j}}^{\mathrm{ph}} n_{\mathrm{j}} \tag{2.5}$$

where k_{ij} are the rate coefficients for the two-body reactions and are usually functions of only temperature; The $\Gamma_{\mathrm{j}}^{\mathrm{ph}}$ are destruction and creation rates due to photoionization and/or photodissociation.

Enzo can also evolve an inhomogeneous radiation field either by directly solving the radiative transfer equation along rays or by solving a set of moment equations derived from

the radiative transfer equation,

$$\frac{1}{c}\frac{\partial I_\nu}{\partial t} + \frac{a_{\rm em}}{a}\hat{n}\cdot\nabla I_\nu - \frac{H}{c}(\nu\frac{\partial I_\nu}{\partial \nu} - 3I_\nu) = -\kappa_\nu I_\nu + j_\nu \tag{2.6}$$

Here $I_\nu(\nu, x, \Omega, t)$ is the specific intensity of the radiation, with dimensions of energy per time t per solid angle Ω per unit area per frequency ν, while κ_ν is the absorption coefficient and j_ν is the emission coefficient.

2.1.2 Chemistry and Radiative Cooling

Enzo has a robust set of chemistry routines that solves the basic chemical reactions in a chemically pristine (hydrogen, helium, deuterium) gas (Abel et al., 1997; Anninos et al., 1997; McGreer & Bryan, 2008; Turk et al., 2009). There are overall 12 total chemical species that consist of atoms and molecules that are the most efficient coolants in a primordial gaseous environment : H, H^+, He, He^+, He^{++}, H, H_2^+ , H_2, e, D, D^+, and HD. For these species, Enzo considers the following physical processes: radiative heating and cooling of the gas from atomic and molecular line excitation, recombination, collisional excitation, free-free transitions, Compton scattering of the CMB, as well as several models for a metagalactic UV background that heat the gas via photoionization and photodissociation. The collisional processes of these chemical species are included in Table 2.1.

The reactions between radiation and atoms are also considered in Enzo as a potential cooling and heating processes. The radiation field is calculated for a given model and time and attenuated by the optical depth of the local cell to model self-shielding of the gas. For the primordial cooling (without metals), the radiative cooling of this metal-free gas is solved by directly computing the cooling and heating rates from the individual processes mentioned above for atomic H and He. Molecular hydrogen (and HD) cooling processes are also considered if heating and cooling from molecular formation and destruction and

Table 2.1: Collisional Processes

(1)	H	+	e	$\rightarrow$	H^+	+	2e
(2)	H^+	+	e	$\rightarrow$	H	+	γ
(3)	He	+	e	$\rightarrow$	He^+	+	2e
(4)	He^+	+	e	$\rightarrow$	He	+	γ
(5)	He^+	+	e	$\rightarrow$	He^{++}	+	2e
(6)	He^{++}	+	e	$\rightarrow$	He^+	+	γ
(7)	H	+	e	$\rightarrow$	H	+	γ
(8)	H	+	H	$\rightarrow$	H_2	+	e
(9)	H	+	H^+	$\rightarrow$	H_2^+	+	γ
(10)	H_2^+	+	H $\rightarrow$	H_2	+	H^+	
(11)	H_2	+	H^+	$\rightarrow$	H_2^+	+	H
(12)	H_2	+	e	$\rightarrow$	2H	+	e
(13)	2H	+	H	$\rightarrow$	3H		
(14)	H	+	e	$\rightarrow$	H	+	2e
(15)	H	+	H	$\rightarrow$	2H	+	e
(16)	H	+	H^+	$\rightarrow$	2H		
(17)	H	+	H^+	$\rightarrow$	H_2^+	+	e
(18)	H_2^+	+	e	$\rightarrow$	2H		
(19)	H_2^+	+	H^-	$\rightarrow$	H_2	+	H
(20)	2H	+	H_2	$\rightarrow$	$2H_2$		
(21)	2H	+	H	$\rightarrow$	H_2	+	H
(22)	H_2	+	H_2	$\rightarrow$	H_2	+	2H
(23)	3H			$\rightarrow$	H_2	+	H
(24)	D	+	e	$\rightarrow$	D^+	+	2e
(25)	D^+	+	e	$\rightarrow$	D	+	γ
(26)	H^+	+	D	$\rightarrow$	H	+	D^+
(27)	H	+	D^+	$\rightarrow$	H^+	+	D
(28)	H_2	+	D^+	$\rightarrow$	HD	+	H^+
(29)	HD	+	H^+	$\rightarrow$	H_2	+	D^+
(30)	H_2	+	D	$\rightarrow$	HD	+	H
(31)	HD	+	H	$\rightarrow$	H_2	+	D
(32)	H	+	D	$\rightarrow$	HD	+	e

Table 2.2: Radiative Processes

(33)	H	+	γ	$\rightarrow$	H^+	+	e
(34)	He	+	γ	$\rightarrow$	He^+	+	e
(35)	He^+	+	γ	$\rightarrow$	He^{++}	+	e
(36)	H	+	γ	$\rightarrow$	H	+	e
(37)	H_2	+	γ	$\rightarrow$	H_2^+	+	e
(38)	H_2^+	+	γ	$\rightarrow$	H	+	H^+
(39)	H_2^+	+	γ	$\rightarrow$	$2H^+$	+	e
(40)	H_2	+	γ	$\rightarrow$	2H		
(41)	D	+	γ	$\rightarrow$	D^+	+	e

collision-induced emission are included if the user chooses this option. The processes for primordial cooling are shown in Table 2.2.

There are two primary metal cooling methods available in Enzo. The simpler of the two uses the analytic cooling function of Sarazin & White (1987), which assumes a fully ionized gas with a constant metallicity of 0.5 $Z_\odot$. A more sophisticated method makes use of multi-dimensional cooling and heating rate tables computed with the photo-ionization code Cloudy (Ferland et al., 1998). This method works by using Cloudy to compute the cooling and heating rates from the metal species only while the primary assumption made is that of ionization equilibrium.

Enzo can also solve the radiative transfer equation in comoving coordinates with a ray tracing implementation that is called Moray. Ray tracing in Enzo is an accurate method to propagate radiation from point sources on a computational grid as long as there are a sufficient number of rays passing through each cell. Along a ray, the radiation transfer equation reduces to

$$\frac{1}{c}\frac{\partial P}{\partial t} + \frac{\partial P}{\partial r} = -\kappa P \tag{2.7}$$

where P is the photon number flux along the ray. The adaptive ray tracing method is based on Hierarchical Equal Area isoLatitude Pixelation (HEALPix Górski et al., 2005) and

progressively splits rays when the angular sampling becomes too coarse. Several conditions are set up as the rules when determining whether the propagating rays will split (Wise & Abel, 2011). The radiation field is calculated by integration along each ray, which is done by considering the discretization of the ray into segments. One ray segment has an optical depth

$$d\tau = \sigma_{\rm abs}(\nu) n_{\rm abs}\, dr, \tag{2.8}$$

where $\sigma_{\rm abs}(\nu)$ and $n_{\rm abs}$ are the cross section and number density of the absorbing medium, respectively. In the static case, the photon flux of a ray when crossing the cell is reduced by

$$dP = P \times (1 - e^{-\tau}). \tag{2.9}$$

The photoionization and photoheating rates associated with a single ray are

$$\begin{aligned} k_{\rm ph} &= \frac{P(1-e^{-\tau})}{n_{\rm abs}\, V_{\rm cell}\, dt_{\rm P}} \\ \Gamma_{\rm ph} &= k_{\rm ph}(E_{\rm ph} - E_{\rm i}) \end{aligned} \tag{2.10}$$

where $V_{\rm cell}$ is the cell volume, $E_{\rm ph}$ is the photon energy, and $E_{\rm i}$ is the ionization energy of the absorber. After the ray tracing is complete, these rates are used as inputs to update the ionization, chemical, and energy states of the gas in each cell.

2.1.3 Structured Adaptive Mesh Refinement

Structured adaptive mesh refinement (SAMR), in a nutshell, is adding and splitting more cells to the locations where needed. The complete grid structure of Enzo has the root grids which consists of the first level hierarchy, where the whole simulation region is covered. When there are certain refinement criteria met, new subgrids will be added to the root grids. We form these new subgrids that have a finer resolution by the refinement factor r, i.e. the ratio of the coarse cell width to the fine cell width. For an example, when $r = 2$ in one

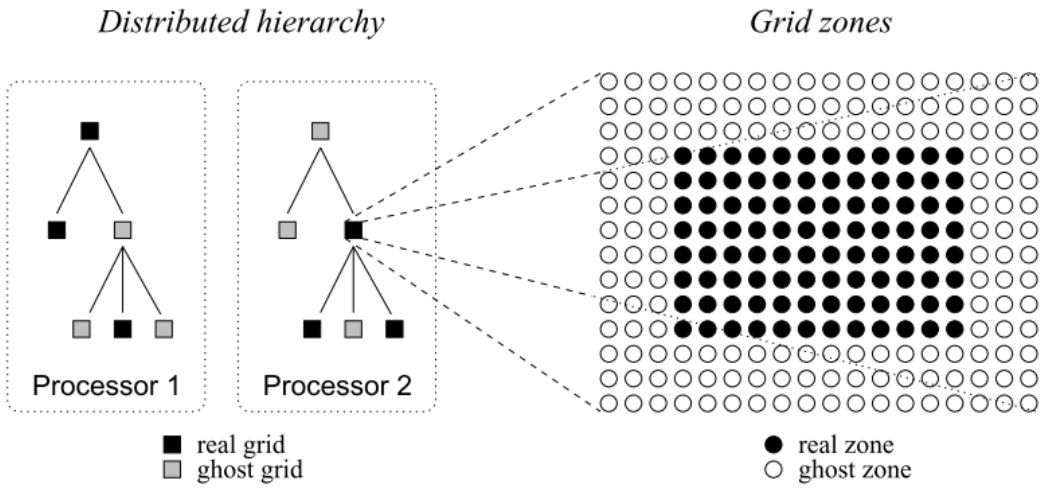

Figure 2.1: Each grid patch in Enzo contains three-dimensional arrays for baryon quantities and one-dimensional arrays for particle quantities. Grids are partitioned into a core of active zones and a surrounding layer of ghost zones. $Left$: Example of a simple, distributed AMR hierarchy showing real and ghost grids. $Right$: Example 2D Enzo grid showing real and ghost zones, as needed for the PPM hydrodynamical stencil (Bryan et al., 2014).

dimension, two smaller cells are contained in one parent cell. Another restriction on the placement of subgrids is that they must be completely enclosed by its parent.

Enzo is developed so that AMR grids are the primary data objects. All of the field variables and particle data are contained within the grid structure. Individual grids are organized into a dynamic, distributed hierarchy of mesh patches. The hydrodynamics solver treats each grid as an independent computational fluid dynamics problem, with Dirichlet boundary conditions stored in the ghost zones, illustrated by Figure 2.1. In Enzo's AMR hierarchy, there are special ghost grids that are also used to interpolate variables between parent and child grids. For each timestep in the simulation, the flux is calculated between child grids that is later projected onto the parent grids.

To integrate the system forward in time, Enzo evolves the system in a manner similar to a "W-Cycle". Beginning with the coarsest level l, all grids on that level are advanced one timestep. Then, one timestep is taken on all grids at the next level of refinement $l + 1$,

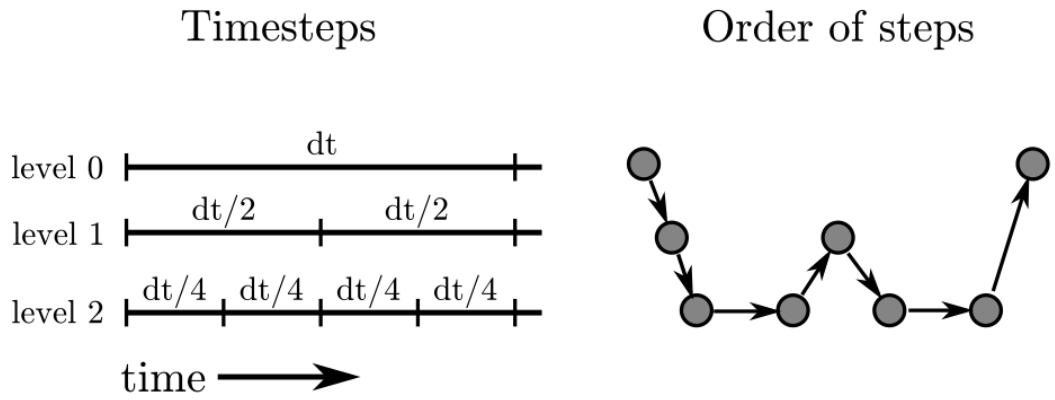

Figure 2.2: $Left$: Example of the timesteps on a 2-level AMR hierarchy. Enzo does not restrict the timesteps on the finer levels to be a factor of $1/2^n$ smaller. $Right$: The order in which the AMR grids are evaluated on each level (Bryan et al., 2014).

and so on until the finest level is resolved. The finest level is then synchronized to the level above it, which then proceeds forward in time one more step. The procedure is shown as Figure 2.2.

Each method operates on all the grids on the given level. The AMR control algorithm, shown below, is recursively in nature and takes the level upon which to operate as an argument.

```
EvolveLevel(level):
  SetBoundaryValues;
  while Time < ParentTime do
      dt = ComputeTimeStep(level);
      SolveHydroEquations(dt);
      SolveOtherEquations(dt);
      Time = Time + dt;
      SetBoundaryValues;
      EvolveLevel(level+1, dt);
      FluxCorrection;
      ProjectionToCoarseGrids;
      RebuildHierarchy(level+1);
end
```

The algorithm of the AMR hierarchy routine for the time evolution of the grids is described as the following.

```
InitializeHierarchy;
while Time <StopTime do
    dt = ComputeTimeStep(0);
    EvolveLevel(0, dt);
    Time = Time + dt;
    CheckForOutput(Time);
end
```

2.1.4 Hydrodynamics

PPM Method

There are two main numerical methods implemented into Enzo to solve the fluid dynamics equations. One purely hydrodynamic method used in Enzo is based on the piecewise parabolic method (PPM) (Colella & Woodward, 1984). Enzo uses a modified Direct Eulerian method, where the one-dimensional Eulerian hydrodynamics equations without expansion terms have the conservative form as

$$\begin{aligned} \frac{\partial \rho}{\partial t} + \frac{1}{a}\frac{\partial \rho v}{\partial x} &= 0 \\ \frac{\partial \rho v}{\partial t} + \frac{1}{a}\frac{\partial \rho v^2}{\partial x} + \frac{1}{a}\frac{\partial p}{\partial x} &= \rho\frac{g}{a} \\ \frac{\partial \rho E}{\partial t} + \frac{1}{a}\frac{\partial \rho v E}{\partial x} &= \rho v\frac{g}{a} \end{aligned} \tag{2.11}$$

Here x and v refer to the one dimensional comoving position and peculiar velocity of the baryonic gas, and g is the acceleration at the cell center. First, the primitive variables (ρ, u and E) are computed with effective left and right states at each grid boundary by constructing a piecewise parabolic relation and then averaged over the corresponding regions. The Riemann problem is solved using these effective left and right states, and finally the fluxes are computed based on the solution to this Riemann problem and the conserved quantities

are updated. The associated Eulerian difference equations are

$$\begin{aligned}
\rho_j^{n+1} &= \rho_j^n + \frac{\Delta t}{\Delta x_j}(\bar{\rho}_{j+1/2}\bar{v}_{j+1/2} - \bar{\rho}_{j-1/2}\bar{v}_{j-1/2}) \\
\rho_j^{n+1}v_j^{n+1} &= \rho_j^{n+1}v_j^n + \frac{\Delta t}{\Delta x_j}(\bar{\rho}_{j+1/2}\bar{v}_{j+1/2}^2 - \bar{\rho}_{j-1/2}\bar{v}_{j-1/2}^2 + \bar{p}_{j+1/2} - \bar{p}_{j-1/2}) \\
&\quad + \frac{\Delta t}{2}g_j^{n+1/2}(\rho_j^n + \rho_j^{n+1}) \\
\rho_j^{n+1}E_j^{n+1} &= \rho_j^n E_j^n + \frac{\Delta t}{\Delta x_j}(\bar{\rho}_{j+1/2}\bar{v}_{j+1/2}\bar{E}_{j+1/2} - \bar{\rho}_{j-1/2}\bar{v}_{j-1/2}\bar{E}_{j-1/2} \\
&\quad + \bar{v}_{j+1/2}\bar{p}_{j+1/2} - \bar{v}_{j-1/2}\bar{p}_{j-1/2}) + \frac{\Delta t}{2}g_j^{n+1/2}(\rho_j^n v_j^n + \rho_j^{n+1}v_j^{n+1}),
\end{aligned} \tag{2.12}$$

where subscripts with j means zone-centered, $j + 1/2$ means surface-centered, and the superscript denotes the n-th timestep. Δx_j is the cell width. All p, ρ, and v are constructed with a monotonic piecewise parabolic (third-order) interpolation method in one dimension. The interpolation formula for a quantity q is given by

$$\begin{aligned}
q_j(x) &= q_{L,j} + \widetilde{x}[\Delta q_j + q_{6,j}(1 - \widetilde{x})] \\
\widetilde{x} &= \frac{x - x_{j-1/2}}{\Delta x_j}, \quad x_{j-1/2} \le x \le x_{j+1/2}
\end{aligned} \tag{2.13}$$

where $q_{L,j}$ is the value of q at the left edge of zone j, while $\Delta q_j = q_{R,j} - q_{L,j}$ and $q_{6,j} = 6[q_j - 1/2(q_{L,j} + q_{R,j})]$ are analogous to the slope and first-order correction to the slope of q, respectively. With these effective left and right states of a quantity q, an approximation to the Riemann problem is used for producing estimates for $\bar{p}_{j\pm1/2}$, $\bar{\rho}_{j\pm1/2}$, and $v_{j\pm1/2}$ that are third-order accurate in space and second-order accurate in time. These are then used to solve the difference equations for the updated primitive variables $\rho^{n+1}, v^{n+1}, E^{n+1}$.

ZEUS Method

Enzo provides an implementation of the finite difference hydrodynamic algorithm employed by the compressible magneto-hydrodynamics code ZEUS (Stone & Norman, 1992).

In the PPM method, operator-split methods break the solution of the hydrodynamic equations into parts, with each part representing a single term in the equations. Each part is evaluated successively using the results preceding it. In comparison, the ZEUS method, in addition to operator-splitting the expansion terms, divides the remaining terms into source and transport steps. These terms are solved in the source steps that represent the right-hand side of hydrodynamics equations, while the transport terms represents the left-hand side.

The ZEUS method uses a von Neumann-Richtmyer artificial viscosity to smooth shock discontinuities that may appear in fluid flows and can cause a breakdown of the finite difference equations, which the resulting terms are

$$\begin{aligned} \rho\frac{\partial v}{\partial t} &= -\nabla p - \rho\nabla\phi - \nabla\cdot Q \\ \frac{\partial e}{\partial t} &= -p\nabla\cdot v - Q:\nabla v \end{aligned} \tag{2.14}$$

Here Q is the artificial viscosity stress tensor, which we take to be diagonal with on-axis terms given by $l^2\rho(\partial v/\partial x)^2$ as proposed by von Neumann and Richtmyer. The length scale l determines the width of shocks and is typically a few times the cell width. In the ZEUS formalism, the velocity is a face-centered quantity, for which the velocity is stored on a grid that is staggered as compared to the density, pressure and energy, which are all at the cell center. By adding up the viscosity terms, the partial difference terms can be updated as

$$\begin{aligned} v_j^{n+b} &= v_j^{n+a} - \frac{\Delta t}{\Delta x_j}\frac{q_j^{n+a} - q_{j-1}^{n+a}}{(\rho_j^n + \rho_{j-1}^n)/2} \\ e_j^{n+b} &= e_j^n - \frac{\Delta t}{\Delta x_j} q_j^{n+a}(v_{j+1}^{n+a} - v_j^{n+a}), \end{aligned} \tag{2.15}$$

where the original and updated states are respectively denoted as $n+a$ and $n+b$. The

artificial viscosity coefficient q_j is described by

$$q_j = \begin{cases} Q_{\rm AV}\rho_j(v_{j+1}-v_j)^2 \quad if \quad (v_{j+1}-v_j) < 0 \\ 0 \quad \text{otherwise} \end{cases} \tag{2.16}$$

where $Q_{\rm AV}$ is a constant with a typical value of two. The transport step is conservative, and the associated finite difference equations are

$$\rho_j^{n+d} = \rho_j^n - \frac{\Delta t}{\Delta x}(v_{j+1/2}^{n+c}\rho_{j+1/2}^* - v_{j-1/2}^{n+c}\rho_{j-1/2}^*) \tag{2.17}$$

Here ρ_j^* is the correctly upwinded value of ρ evaluated at the cell-face corresponding to v_j, making $\rho_j^* v_j$ the mass flux at the cell boundary and guaranteeing mass conservation.

2.2 Monte Carlo Radiation Transfer

The basic idea behind Monte Carlo methods is generating random numbers from probability distributions. Consider a variable x with probability density $P(x)$. We can generate the fully random variable R as the cumulative probability as,

$$R = \int_{-\infty}^{x} P(x')dx' \tag{2.18}$$

where R is in the range of $[0, 1]$. So in order to get the random variable value x, we need to know the analytical form of the integration above. However, in many cases, the integration forms are not trivial. One solution around this difficulty is the rejection method. If we pick another probability density $P^{\rm upper}(x) \geq P(x)$ for all possible values of x, the probability is not normalized, where $\int_{-\infty}^{\infty} P^{\rm upper}(x)\,dx = N$, where $N > 1$. The function $P^{\rm upper}(x)$ is taken to be integrable, which is called the comparison function. If a random point chosen uniformly in this probability function lies under the $P(x)$ value as well, we

accept the corresponding value of x, otherwise the result is rejected and another random number is generated. By generating another random number R_1, we can determine whether the generated x value is accepted. If the number lies between 0 and $P(x)$, we will keep x. Alternatively, we compare R_1 with $P/P^{\rm upper}$, and we will accept the generated x if R_1 is smaller.

The general Monte Carlo process for a scattering transfer calculation consists of following steps.

1. For a single photon, we first determine the frequency x in the atom's frame, which is determined by the natural line profile $L(x) = a/\pi(\pi^2 + a^2)$ (see Equation 1.63).

2. For the hydrogen atom that generates the Lyα photon, the velocity magnitude $v_{\rm H}$ is determined from a Maxwellian distribution. In the calculation, we use the normalized velocity according to the thermal velocity distribution of the medium, which is $u = v_{\rm H}/v_{\rm th}$. The probability distribution of u satisfies the thermal line profile, which is $G(u) = e^{-u^2}/\sqrt{\pi}$.

3. For the direction of both the photon and the hydrogen atom, the photon direction is uniformly distributed without any polarization, whose normal vector is

$$\hat{n} \propto \begin{bmatrix} 2R_1 - 1 \\ 2R_2 - 1 \\ 2R_3 - 1 \end{bmatrix} \tag{2.19}$$

   The result will be rejected if $|\hat{n}| > 1$, otherwise, we will normalize the directional vector.

4. Considering the non-relativistic limit, where $v_{\rm H}/c \ll 1$. The initial frequency in the

lab frame can be obtained by Lorentz transformation as,

$$x_{\rm lab} = x + u \cdot \hat{n}, \tag{2.20}$$

where x is the frequency in the reference frame of the atom.

5. When propagating the Lyα photon, we need to generate the optical depth τ experienced by the photon, where $e^{-\tau}$ is integrable so that we have

$$\tau = \ln R \tag{2.21}$$

6. The optical depth is converted into a physical distance s which is

$$\tau = \int_0^s d\lambda \, n_{\rm H}(r')\sigma(r', x'), \tag{2.22}$$

where $r' = r + \lambda\hat{n}$ and $x' = x - u \cdot \hat{n}$. We cannot, however, integrate the optical depth along the path. But it is reasonable for us to assume that $(\bar{s}\nabla n_{\rm H})/n_{\rm H} \ll 1$. The photon travel distance is thus approximated as

$$s = \frac{\tau}{n_{\rm H}\sigma} \tag{2.23}$$

7. For a single scattering event, the probability distribution of the velocities that is parallel to the incident photon is

$$P(u_\parallel) = \frac{a}{\pi H(a,x)} \frac{\exp(-u_\parallel^2)}{(x-u_\parallel)^2 + a^2}. \tag{2.24}$$

The probability distribution is difficult to integrate analytically in a general case, so we utilize the rejection method to find a randomly generated parallel injection velocity. In order to increase the rate of acceptance with the randomly generated

numbers R_2, we use the two domains separated comparison functions (Zheng & Miralda-Escudé, 2002),

$$g(u_\parallel) \propto \begin{cases} [(x-u_\parallel)^2 + a^2]^{-1} & \text{for} \quad u_\parallel \leq u_0 \\ e^{-u_0^2}[(x-u_\parallel)^2 + a^2]^{-1} & \text{for} \quad u_\parallel > u_0. \end{cases} \tag{2.25}$$

The value of u_0 is chosen to minimize the fraction of generated values that will be discarded. The acceptance fractions are then required to be $\exp(-u_\parallel^2)$ and $\exp(-u_\parallel^2)/\exp(-u_0^2)$ for the $u \leq u_0$ and $u > u_0$ regimes, respectively. A random number R_2 uniformly distributed between 0 and 1 determines which region we use by comparing it with p, where

$$\begin{aligned} p &= \frac{\int_{-\infty}^{u_0} g(u_\parallel) du_\parallel}{\int_{-\infty}^{\infty} g(u_\parallel) du_\parallel} \\ &= \frac{\theta_0 + \pi/2}{[1-\exp(-u_0^2)]\theta_0 + [1+\exp(-u_0^2)]\pi/2} \\ \theta_0 &= \tan^{-1}\frac{u_0 - x}{a} \end{aligned} \tag{2.26}$$

We generate u as $a\tan\theta + x$, where θ is a random number uniformly distributed in the range $[-\pi/2, \theta_0]$ and $[\theta_0, \pi/2]$ for $R \leq p$ and $R > p$, respectively. Then another random number uniformly distributed between 0 and 1 determines whether the generated value of u is accepted by comparing it with the corresponding acceptance fraction.

8. For the perpendicular velocity distribution, the two polarization velocities are generated with the two independent random numbers and are described by

$$u_\perp = \begin{cases} (-\ln R_1)^{1/2}\cos(2\pi R_2) \\ (-\ln R_1)^{1/2}\sin(2\pi R_2) \end{cases} \tag{2.27}$$

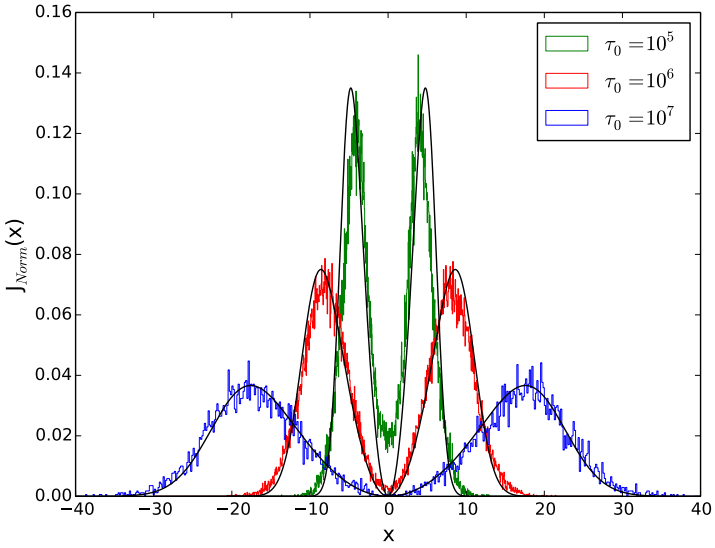

Figure 2.3: Monte Carlo test of analytical solution for a uniform sphere and central radiation source. This test shows the Lyα spectra emerging from a uniform spherical gas cloud, in which Lyα photons are injected in the center of the sphere, at the line center where $x = 0$. The total line center optical depth, τ_0 from the center to the edge is $\tau_0 = 10^5$ (green), $\tau_0 = 10^6$ (red) and $\tau_0 = 10^7$ (blue) with temperature $T = 7000$ K. Overplotted as the black lines are the analytic solutions, showing that our code is accurate at high optical depths.

9. Once we have determined the velocity vector of the atom that is scattering the photon, the outgoing direction of the photon after scattering can be decided by the phase function (Equation 1.75). The azimuthal angle μ is then determined by the phase function with the random spherical angle θ.

2.2.1 Monte Carlo Radiation Test

For any new numerical tool, it is essential to test against known analytical solutions. Here we test our Lyα radiation transport code to the results found in Neufeld (1990). We focus on the ideal static iso-density cases where analytical solutions exist. We first consider the scenario for a iso-density sphere where Lyα photons are generated from the sphere center. We compute the spectrum and intensity at the boundary of the sphere. Figures 2.3

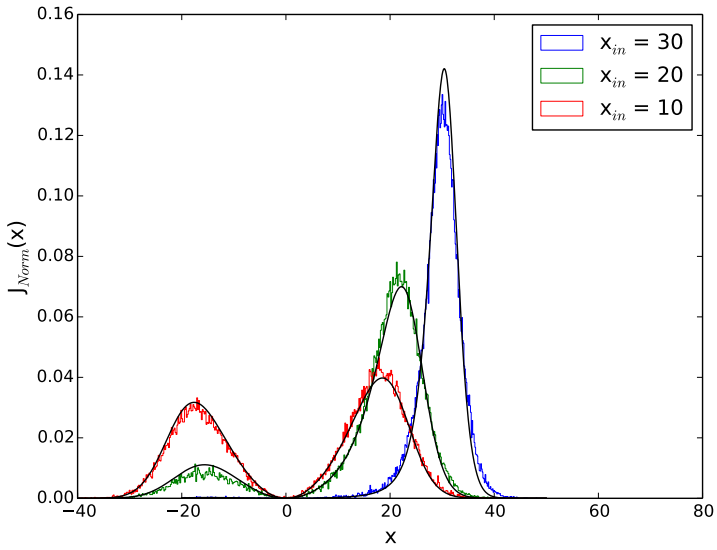

Figure 2.4: The figure shows the Monte Carlo test comparing the analytical solution for the emergent spectrum of photons injected with different initial frequencies Doppler shifting away from the line center. The optical depth set up to be $\tau_0 = 10^7$, while the injection frequencies are $x_{\rm in} = 30$ (blue), $x_{\rm in} = 20$ (green) and $x_{\rm in} = 10$ (red) at a temperature $T = 7000$ K.

and 2.4 show Lyα spectrum emerging from such a sphere with a central Lyα point source surrounded by a pure neutral hydrogen gas, where we consider several cases that vary the total optical depth. The black lines show the associated analytical results.

We compare these exact solutions of the radiation transfer equation to our numerical results, demonstrating that our code works well in the optically thick case. We compute the average number of scattering events before escaping a certain optical depth, $N_{\rm scat} \sim C\tau_0$, where $C \sim 1.1$ for the slab case and $C \sim 0.6$ for the sphere case. In Figure 2.5, we compare this number $N_{\rm scat}$ to the expected analytical result the test relations of average scattering number of a sphere given a certain optical depth τ_0 at a temperature $T = 7000$ K.

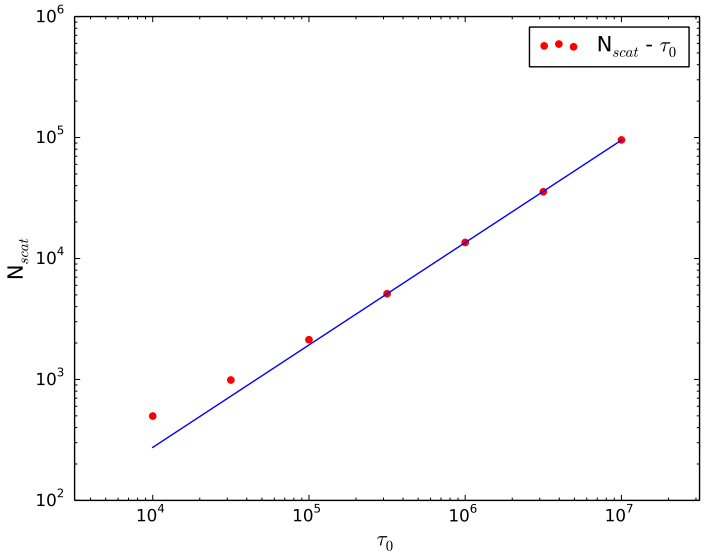

Figure 2.5: The total number of scattering events that a Lyα photon experiences before it escapes from a uniform sphere with optical depth τ_0. The circles and red solid line shows the results from our Monte Carlo simulation and analytical solution, respectively.

CHAPTER 3

RESULTS AND DISCUSSION

One viable seeding mechanism for supermassive black holes is the direct gaseous collapse route in pre-galactic dark matter halos, producing objects on the order of $10^4 - 10^6$ solar masses. These events occur when the gas is prevented from cooling below 10^4 K that requires a metal-free and relatively H_2-free medium. The initial collapse cools through atomic hydrogen transitions, but the gas becomes optically thick to the cooling radiation at high densities. We explore the effects of Lyman-α trapping in such a collapsing system with a suite of Monte Carlo radiation transport calculations in uniform density and isotropic cases that are based from a cosmological simulation. Our method includes both non-coherent scattering and two-photon line cooling. We find that Lyman-α radiation is marginally trapped in the parsec-scale gravitationally unstable central cloud, allowing the temperature to increase to 50,000 K at a number density of 3×10^4 cm^{-3} and increasing the Jeans mass by a factor of five. The effective equation of state changes from isothermal at low densities to have an adiabatic index of 4/3 around the temperature maximum and then slowly retreats back to isothermal at higher densities. Our results suggest that Lyman-α trapping delays the initial collapse by raising the Jeans mass. Afterward the high density core cools back to 10^4 K that is surrounded by a warm envelope whose inward pressure may alter the fragmentation scales at high densities.

This work has been published in the Monthly Notices of the Royal Astronomical Society (Ge & Wise, 2017). This work was co-authored by John Wise who helped me a lot along the project.

3.1 Introduction

Observations of bright quasars at redshifts $z \gtrsim 6$ indicate that supermassive black holes (SMBHs) with masses over 10^9 $M_\odot$ form within the first billion years after the Big Bang. (Fan, 2006; Willott et al., 2010; Mortlock et al., 2011; Wu et al., 2015). These SMBHs are expected to form by seeding mechanisms that can be categorized into three classifications: the growth of massive metal-free (Population III; Pop III) stellar remnants (Madau & Rees, 2001; Volonteri & Rees, 2006), collapse of dense stellar clusters (Davies et al., 2011) and a direct collapse of a gaseous metal-free cloud (Bromm et al., 2003; Wise et al., 2008; Begelman et al., 2006; Volonteri et al., 2008). Light BH seeds from Pop III stars will have a difficult time growing at the Eddington limit into the observed high-redshift quasars because of the warm and diffuse medium left behind by its progenitor star and the limited period between their formation and redshift 6 (Johnson & Bromm, 2007; Alvarez et al., 2009; Jeon et al., 2012); however, hyper-Eddington accretion may overcome this barrier (Alexander & Natarajan, 2014; Inayoshi et al., 2016). Furthermore after a BH merger, the kick velocity of the resulting BH is most likely greater than the escape velocity of their host dark matter halos (Micic et al., 2006; Herrmann et al., 2007).

In the direct collapse scenario, which is the focus of this work, halos with a virial temperature $T_{\rm vir} \simeq 10^4$ K ($M_{\rm vir} \gtrsim 10^8$ $M_\odot$ at $z \sim 10$), known as atomic cooling halos, that are chemically pristine and have a very low molecular hydrogen density can catastrophically collapse (Rees & Ostriker, 1977; White & Frenk, 1991). This happens at such a virial temperature because the atomic hydrogen ionization and collisional de-excitation rates increase by several orders of magnitude. The general criterion for a rapid gaseous collapse is that the gas cooling time is less than the free-fall time. It is thought that the massive baryon cloud collapses monolithically and isothermally without fragmentation in a Lyman-Werner (LW) background[1] $J_{21} > J_{\rm crit} \simeq 10^3$ given a 10^5 K blackbody spectral

[1] J_{21} is the background specific intensity in units of 10^{-21} erg s^{-1} cm^{-2} Hz^{-1} sr^{-1} at the Lyman limit

shape (e.g. Omukai, 2001; Shang et al., 2010; Wolcott-Green & Haiman, 2012; Agarwal & Khochfar, 2015; Glover, 2015).

Numerical simulations have indeed shown that fragmentation is suppressed when H_2 cooling is absent (Bromm et al., 2003; Regan & Haehnelt, 2009). The Jeans mass

$$M_{\rm J} \simeq 10^{5.5}\ {\rm M}_\odot \left(\frac{T}{10^4\ {\rm K}}\right)^{3/2} \left(\frac{n}{10^4\ {\rm cm}^{-3}}\right)^{-1/2}, \tag{3.1}$$

determines the approximate fragmentation mass scale during the collapse and is a key characteristic quantity to follow during this phase. The gas temperature T highly depends on whether radiative cooling is efficient, in particular H_2 in a metal-free gas. When it is efficient, the gas can cool down to $T \sim 300$ K, corresponding to $M_{\rm J} \sim 10^3$ $\rm M_\odot$, implying that the cloud will form massive Pop III stars. Prior to reionization, the LW background is not sufficiently high to affect all atomic cooling halos (Visbal et al., 2014b), but there is a small possibility that such a pre-galactic halo has a nearby neighboring galaxy that boosts the impinging LW radiation above $J_{\rm crit}$ (e.g. Dijkstra et al., 2008; Agarwal et al., 2014; Visbal et al., 2014a; Regan et al., 2016, 2017). Without H_2 cooling, atomic hydrogen transitions allow the gas to cool to 8000 K but no further, resulting in a central Jeans mass $M_{\rm J} \sim 10^5 - 10^6$ $\rm M_\odot$, that has the possibility of collapsing into a dense stellar cluster or a supermassive star, ultimately producing a massive black hole on the order of $M \simeq 10^4 - 10^6$ $\rm M_\odot$.

Coherent scattering properties of Lyα photons have been studied for decades, initially focusing on analytical treatments of radiation scattering (Unno, 1952; Hummer, 1962; Adams, 1971) and the Eddington approximation (Harrington, 1973; Neufeld, 1990; Loeb & Rybicki, 1999). More recent studies utilize Monte Carlo methods in several different scenarios: the emerging spectrum from an isothermal homogeneous medium with plane-parallel or spherical symmetry (Ahn et al., 2002; Zheng & Miralda-Escudé, 2002), an

(13.6 eV).

isotropic velocity field (Dijkstra et al., 2006), a density gradient field (Barnes & Haehnelt, 2010), dust absorption and re-emission (Verhamme et al., 2006), Lyα radiative transfer shells model (Gronke et al., 2015) and transmission through the intergalactic medium (Laursen et al., 2011).

Lyα trapping has been considered to be an important impact factor on the formation of direct collapse black holes (Spaans & Silk, 2006; Latif et al., 2011; Yajima & Khochfar, 2014). The scattering of photons in the dense optically-thick core will limit gas cooling and possibly increase the temperature, leading to a higher Jeans mass. Furthermore, radiation trapping leads to a breakdown of the Eddington limit, making hyper-Eddington accretion onto BHs a possibility (Inayoshi et al., 2016). This transition from an optically-thin cooling limit to an optically-thick medium has been previously approximated with a polytropic equation of state, derived in spherical symmetry, that evolves from isothermal to adiabatic in a range $n = 1 - 10^5$ cm^{-3} (Spaans & Silk, 2006). In this model, the adiabatic behavior at high densities will keep the gas nearly H_2 free during the collapse.

The primary aim of this work is to examine the thermodynamics of the direct collapse to a massive BH seed in an atomic cooling halo. We first construct a radiative cooling model that includes the effects of Lyα trapping that allows us to explore under what conditions the gas deviates from isothermal. Then separately, we perform a cosmological simulation focusing on an atomic cooling halo from which we extract radial profiles and then perform a suite of Monte Carlo Lyα radiation transport calculations in various idealized cases. From these results, we estimate the effective equation of state of the collapsing system, shedding light on the expected mass scale of the central object. The fragmentation scale and final outcome of such a primordial collapse are still open questions, and we aim to edge closer to their answers by including another key physical process in its initial collapse.

The rest of the chapter is organized as follows. In §3.2 we describe our radiative cooling model, including an approximate model of Lyα trapping whose details are left for the Ap-

pendix, the cosmological simulation, and the Lyα radiation transport calculation. In §3.3, we present the results of our radiative cooling rates with Lyα trapping and a suite of Monte Carlo calculations, focusing on the effects of Lyα trapping on the thermodynamics of the central collapse. In §3.4, we conclude and discuss the impact of Lyα trapping especially regarding the fragmentation mass scale and discuss the limitations of our method with future directions on resolving the full evolutionary sequence to a massive BH seed.

3.2 Methods

We investigate the thermal evolution of a collapsing metal-free gas cloud with two independent methods. First, we calculate a cooling rates as a function of temperature, i.e. the cooling curve, when the effects of Lyα trapping are included. Second, in a more realistic setting, we further investigate the amount Lyα trapping and its thermal effects in a Lyα radiation transport post-process calculation that uses several snapshots from a cosmological simulation. We extract the radially averaged properties from a collapsing atomic cooling halo in the cosmological simulation, which serves as a basis for the spherically symmetric radiation transport calculation. From this second approach, we can quantify the propagation of the Lyα radiation and how the cooling rates deviate from the optically-thin approximation.

3.2.1 Radiative cooling with Lyα radiation trapping

We initially investigate the impact of Lyα radiation trapping by modifying the primordial gas cooling curve with an approximate trapping model. This model is similar to previous one-zone models and chemical networks (e.g. Cen, 1992; Omukai, 2001; Schleicher et al., 2010; Shang et al., 2010; Glover, 2015). Generally, the thermal evolution of one-zone models in a free-fall collapse provides a convenient check for possible fragmentation mass scales. These models consider a full chemical network to calculate the cooling rates, and

we initially approach the problem of including Lyα trapping by inspecting how it modifies the cooling curve. Here we adopt the radiative cooling rates from Cen (1992) as a staring point that include collision ionization and excitation, recombination, bremsstrahlung, and Compton cooling from a primordial gas. We also include molecular hydrogen cooling, using the rates from Glover & Abel (2008); however, we consider a strong LW radiation background that suppresses its efficacy when $J_{21} \gtrsim 10^3$. We calculate the cooling curve in a temperature range of $\log(T/\mathrm{K}) = 2-6$ and number density range of $\log(n/\mathrm{cm}^{-3}) = 2-9$.

We now review the resonance scattering properties of Lyα radiative transfer in a pure hydrogen gas to demonstrate how Lyα trapping occurs in an optically-thick medium. While scattering between hydrogen atoms, a single Lyα photon will undergo a frequency change from Doppler effects. As is convention and for convenience, we refer to the frequency in terms of the Doppler width of the line, $x \equiv (\nu - \nu_0)/\Delta\nu_\mathrm{D}$, arising from the thermal velocities of the atoms. Here $\Delta\nu_\mathrm{D} = \nu_0(2k_\mathrm{B}T/m_\mathrm{p}c^2)^{1/2}$ is the Doppler width; $\nu_0 = 2.466 \times 10^{15}$ Hz is the rest-frame frequency of the Lyα transition, and k_B and m_p are the Boltzmann constant and the proton mass, respectively. For a zero temperature gas, the optical depth in the Lyα line follows a Lorentzian profile with respect to frequency x. However, when a Maxwellian velocity distribution is considered, the Lyα line optical depth transforms into a Voigt profile

$$\tau_\nu^\mathrm{Voigt} = \frac{\sqrt{\pi}e^2}{m_\mathrm{e}c} N_\mathrm{HI} f_{12} \times \int \frac{dv}{b} e^{-v^2/b^2} \frac{4\gamma_{12}}{16\pi^2[\nu - (1 - v/c)\nu_0]^2 + \gamma_{12}^2}, \tag{3.2}$$

where $f_{12} = 0.4162$ is the Lyα oscillator strength, N_HI is the neutral hydrogen column density, and the hydrogen velocity dispersion is parameterized as the Doppler parameter

$$b \equiv \sqrt{\frac{2}{3}\langle v^2 \rangle} = \sqrt{\frac{2k_\mathrm{B}T}{m_\mathrm{p}}}. \tag{3.3}$$

Finally, the natural width $\gamma_{12} = A_{12}$ of the line is related to the Einstein A-coefficient $A_{12} = 6.24 \times 10^8$ s^{-1}. The Voigt profile can be difficult to integrate analytically. However, it can be approximated by introducing the Voigt parameter $a \equiv A_{12}/4\pi\Delta\nu_{\rm D}$, allowing us to rewrite the integral as

$$H(a,x) \equiv \frac{\tau_x}{\tau_0} = \frac{a}{\pi}\int_{-\infty}^{\infty} dy \frac{e^{-y^2}}{(y-x)^2+a^2} \simeq \begin{cases} e^{-x^2} & (\text{core}) \\ a/(x^2\sqrt{\pi}) & (\text{wing}) \end{cases}, \tag{3.4}$$

defining $y \equiv v/b$. Here τ_0 represents the optical depth at the line center.

The transport of Lyα photons is much different than continuum radiation transport because of the very short mean free path and, most importantly, their re-emission after absorption. To account for these processes, it is essential to include the scattering term in the radiative transfer equation for Lyα radiation. For example, in an optically-thick system, photons just above the Lyman limit ($E = 13.6$ eV) will be absorbed once and the ion will be subject to case-B recombination. In contrast, neutral atoms will scatter Lyα photons many times. During these scattering events, their frequencies will shift away from the Lyα line center into the wings, where the optical depth is smaller and thus more prone to escape from the system.

We utilize a simplified scattering and trapping model for Lyα radiation transport in our cooling rate calculation. In this model, the photons that are generated from recombination and collisional de-excitation are not assumed to escape the system. They can be trapped if the optical depth is sufficiently high, suppressing any associated cooling. We approximate the effective cooling rate by calculating the average number of scatterings that photons experience before they shift into the wing part of the line profile where they can escape and cool the system. For the interested reader, more details about Lyα radiation transfer can be found in Appendix 3.5.

Lyα radiation is mainly generated by two mechanisms: recombination and collisional excitation. Hydrogen will be ionized at $T \gtrsim 10^4$ K after either being photo- or shock-heated. For recombination, a fraction of the captured free electrons will decay into the ground state through a cascade, producing a Lyα photon in the process. The emissivity of recombination is

$$\eta^{\rm rec} = f_\alpha \alpha_B h\nu_\alpha n_{\rm e} n_{\rm HII}, \tag{3.5}$$

where f_α denotes the ratio of Lyα photons generated from case B recombinations, and $\alpha_{\rm B}$ is the case B recombination rate coefficient. We take $f_\alpha \simeq 0.68$ as a constant because it is only weakly dependent on temperature (Osterbrock & Ferland, 2006). The second process includes a collisional excitation that occurs when an electron decays into the ground state, producing a Lyα photon. The de-excitation coefficient is $A_\alpha = 3.7 \times 10^{-17} \exp(-h\nu_\alpha/kT) T^{-1/2}$ (Osterbrock & Ferland, 2006) and the associated emissivity is

$$\eta^{\rm dcol} = A_\alpha n_{\rm e} n_{\rm HI}. \tag{3.6}$$

In a pure hydrogen gas with a low ionization state, the intrinsic Lyα emissivity can be approximated as $\eta^{\rm src} \equiv \eta^{\rm rec} + \eta^{\rm dcol}$. At temperatures $T = 10^3 - 10^4$ K, the high value of the Einstein A-coefficient A_{12} results in the emissivity being dominated by spontaneous radiation.

At higher densities ($n \gtrsim 10^6$ cm^{-3}), the two-photon process (2s $\rightarrow$ 1s) becomes one of the dominant coolants, even though its Einstein A-coefficient $A_{\rm 2s-1s} = 8.23$ s^{-1} (Omukai, 2001) is significantly smaller than Lyα, because its radiation is optically thin, especially when the Lyα (2p $\rightarrow$ 1s) photons are trapped (Schleicher et al., 2010; Johnson et al., 2012). Also in dense gas, H^- cooling through the free-bound transition ($H + e^- \rightarrow H^- + \gamma$) becomes important and will emit and scatter Lyα photons. However, these transitions are insignificant on the level of 10^{-5} with respect to the collisional de-excitation channel. We can compare the scattering cross-section of photo-detachment in hydrogen to

the two-photon process, both of which can interfere with typical spontaneous emission scattering events. The cross-section of the two-photon emission is $\sim 10^{-10}$ of the H^- photo-detachment cross-section. However, the typical H^- abundance is $\ll 10^{-10}$ when $n < 10^{17}$ cm^{-3} (Van Borm et al., 2014), and from this low abundance of H^-, we can conclude that photo-detachment processes can be neglected at the densities explored in this study (however see Johnson & Dijkstra, 2017). This assumption will break down at higher densities $n \gtrsim 10^{15}$ cm^{-3} when both H^- and H_2 become abundant (Omukai, 2001; Van Borm et al., 2014). However, the free-fall time is extremely short at these times, and it is unclear whether Lyα trapping will play a role during this stage, warranting further work that is outside the scope of this thesis.

3.2.2 Cosmological simulation setup

In our second approach, we perform a suite of Monte Carlo Lyα radiation transport calculations (see Section 3.2.3) that use a cosmological simulation as its basis, which we describe in this section. This simulation focuses on the initial collapse of an atomic cooling halo that uses the radiative cooling rates calculated in the optically-thin limit. We stress that this simulation does not include the hydrodynamic response to any suppressed cooling that comes from Lyα trapping, but it provides a starting point for the post-processing Monte Carlo calculation.

We use a zoom-in simulation with the adaptive mesh refinement (AMR) code ENZO (The Enzo Collaboration et al., 2014), which utilizes an N-body particle-mesh solver for the dynamics of dark matter particles and an piecewise parabolic Eulerian method for the hydrodynamics (Colella & Woodward, 1984; Bryan et al., 1995). The initial conditions are generated with MUSIC (Hahn & Abel, 2011) in a comoving volume of (1 Mpc)^3 at redshift $z = 500$. We consider the following cosmological parameters that are consistent with the WMAP 9-year results: $\Omega_{\rm DM} = 0.235$, $\Omega_\Lambda = 0.7185$, $\Omega_{\rm b}h^2 = 0.02256$, $\sigma_8 =$

0.820, $n_{\rm s} = 0.9710$, $h = 0.697$, where the variables have their typical definitions (Hinshaw et al., 2013). The differences between the WMAP9 and latest Planck parameters (Planck Collaboration et al., 2016) only has minimal timing impacts on structure formation and are within their uncertainties.

We first perform a pathfinder, low-resolution 64^3 dark matter simulation to locate the most massive halo in the volume at $z = 9$, using the HOP halo finding algorithm (Eisenstein & Hut, 1998). Then we resimulate the volume with a zoom-in setup that has the same large-scale modes but with higher resolution and baryons. In this setup, we use a base AMR grid with 256^3 particles and cells that is supplemented with two nested grids, centered on the location of the most massive halo at $z = 9$. These nested grids are static in the AMR hierarchy. The innermost grid has a DM mass resolution of 27.3 $M_\odot$ (1024^3 effective resolution) that is 64 times finer than the top grid. The simulation uses up to 20 levels of AMR refinement, corresponding to a maximal comoving resolution of 0.03 pc. We refine the grid on baryon and DM overdensities when they exceed $3 \times 2^{-0.3l}$, where l is the AMR level. The negative exponent results in the simulation being super-Lagrangian focusing more resolution at higher densities. In addition, the local Jeans length is always resolved by at least four cells to avoid artificial fragmentation (Truelove et al., 1997).

We consider a chemical network of nine primordial species (H, H^+, He, He^+, He^{++}, H^-, H_2^+, H_2 and e^-) to evolve their abundance in non-equilibrium (Anninos et al., 1997; Abel et al., 1997) with the H_2 rates from Glover & Abel (2008). We neglect any metal enrichment because the direct collapse formation scenario requires that the gas to be warm ($\gtrsim 5000$ K) to avoid cooling and fragmentation. Thus to focus on this scenario, we consider only primordial cooling calculated in the optically-thin limit. We do not use the cooling curve that includes Lyα trapping (Section 3.2.1) because we desire to compare the results of a one-zone model and a post-processing calculation, independent of each other. We also apply a Lyman-Werner radiation background with an intensity of $J_{21} = 10^5$ without any

self-shielding effects. We note that this value of J_{21} is artificially high that requires a very close ($\lesssim 1$ kpc) and luminous radiation source. We apply such an intense background to remove any effects from H_2 cooling in order to focus on Lyα radiation trapping.

3.2.3 Monte Carlo Radiative Transfer

Our main results on the effects of Lyα trapping originate from post-processing the most massive halo in spherical symmetry from the previously described cosmological simulation with a suite of Monte Carlo radiation transport calculations. We consider three cases that progressively increase the realism of the system, but are independent of each other:

1. A **uniform density case** with hydrogen number densities ranging from 10^5 cm^{-3} to 10^9 cm^{-3} where the photons are propagated for 10^8 s, corresponding to a light-crossing time of 1 pc, approximately the radius of the Jeans unstable central gas cloud in an atomic cooling halo.

2. A **time-independent isotropic case** whose radial properties are derived from the collapse halo in the cosmological simulation at its final time, when the maximum density is 3×10^{11} cm^{-3}. This calculation is also integrated for 10^8 s.

3. A **time-dependent isotropic case** extends the static case, where we allow the cloud to contract. We take the radial averages from six outputs, whose maximum number densities range from 3×10^7 cm^{-3} to 3×10^{11} cm^{-3} with each output having maximum densities approximately an order of magnitude apart. The output times are 65, 255, 1,100, 4,000, and 12,600 years before the final output.

We extract the pertinent time-dependent radially averaged gas properties, such as density, temperature, and ionization fraction, from the most massive halo as it is catastrophically collapsing. We do not extract the velocity information, but we consider three different

cases: a static medium, radial infall, and solid body rotation. The two latter cases affect the Doppler shifts in sufficiently different ways. Thus, we can unambiguously characterize how the propagation of Lyα photons are influenced by each idealized motion. In the simulation data, the gas flows have coherent rotational and infall characteristics but with subsonic turbulent motions superimposed, which would have a similar effect as Maxwellian thermal motions of the gas. We explore two different velocities, 1 and 5 km s^{-1}, corresponding to 10% and 50% of the sound speed c_s for a $T = 10^4$ K gas, and is consistent with velocities found in cosmological simulations of atomic cooling halos (e.g. Wise & Abel, 2007).

This treatment provides a better approximation of the amount Lyα trapping than our optically-thick adjustments to the cooling curve (Section 3.2.1). Although it is technically possible to ray trace Lyα photons through the native AMR grids from the cosmological simulation (Barnes & Haehnelt, 2009; Laursen et al., 2009; Smith et al., 2017), we ray trace through a spherically symmetric system because the ellipticity of iso-density surfaces is always greater than 0.99 at $n_\mathrm{H} \geq 10^4\ \mathrm{cm}^{-3}$. In addition, we are more interested in the radiation transport within a dense core of a single halo instead of more diffuse regions of evolved galaxies. A ray tracing calculation through an inhomogeneous, very optically-thick medium can suffer from convergence issues and high computational demand, stemming from the large number of scattering events, unlike lower density (yet still optically-thick) calculations. Thus, we choose to treat the system in spherical symmetry to avoid these issues. However the trade-off is that we lose any information about the radiation field asymmetries, such as preferred escape directions. These effects could especially originate from any velocity fields that are not particularly radial or tangential, even if the density field is nearly spherical.

We post-process these data to estimate the evolution of the Lyα radiation field during the collapse. We base our radiative transfer method on Laursen et al. (2009). In this method, Lyα photons are isotropically initialized at the sphere center for the uniform case, and in

radial shells for the non-uniform cases. They have a relative frequency

$$x_{\rm ph} = x_{\rm Ly\alpha} - \mathbf{v}_{\rm H} \cdot \hat{\mathbf{n}}_{\rm ph}, \tag{3.7}$$

where $\mathbf{v}_{\rm H}$ and $\hat{\mathbf{n}}_{\rm ph}$ are the bulk velocity of the gas in units of the sound speed and the photon propagation direction, respectively. We then transport each photon according to the following prescription. The photon travels along a direction $\hat{\mathbf{n}}_{\rm ph}$ for a distance r that corresponds to a uniformly distributed random optical depth $\tau = \int N_{\rm HI}\sigma(x) r\, dr$, where $\sigma(x)$ is the Lyα cross-section at the relative frequency x and $N_{\rm HI}$ is the neutral hydrogen column density. During an interaction, the photon scatters off a neutral hydrogen atom, causing a frequency shift $\Delta x = -u_{\parallel} + \hat{\mathbf{n}}_{\rm ph} \cdot \mathbf{u}$. Here $\mathbf{u}$ is the relative velocity between the gas and photon, and $u_{\parallel}$ is the component parallel to $\hat{\mathbf{n}}_{\rm ph}$. After the photon is scattered, the probability of a change in propagation direction θ is given by the phase function

$$W(\theta) = \begin{cases} 1/2, & \text{(core; } 2P_{1/2}\text{)} \\ (7/16)[1 + (3/7)\cos^2\theta)], & \text{(core; } 2P_{3/2}\text{)} \\ (3/8)(1 + \cos^2\theta), & \text{(wing)} \end{cases} \tag{3.8}$$

that is derived from a dipole approximation of the interaction, and in the profile wings, the scattering behaves like a classical system producing a dipole distribution (Hamilton, 1940; Stenflo, 1980; Laursen et al., 2009).

3.3 Results

3.3.1 Radiative cooling with Lyα trapping

The massive seed BH mass is largely influenced by the mass accretion rates into the central gas cloud and any fragmentation that might occur during its catastrophic collapse, prompted

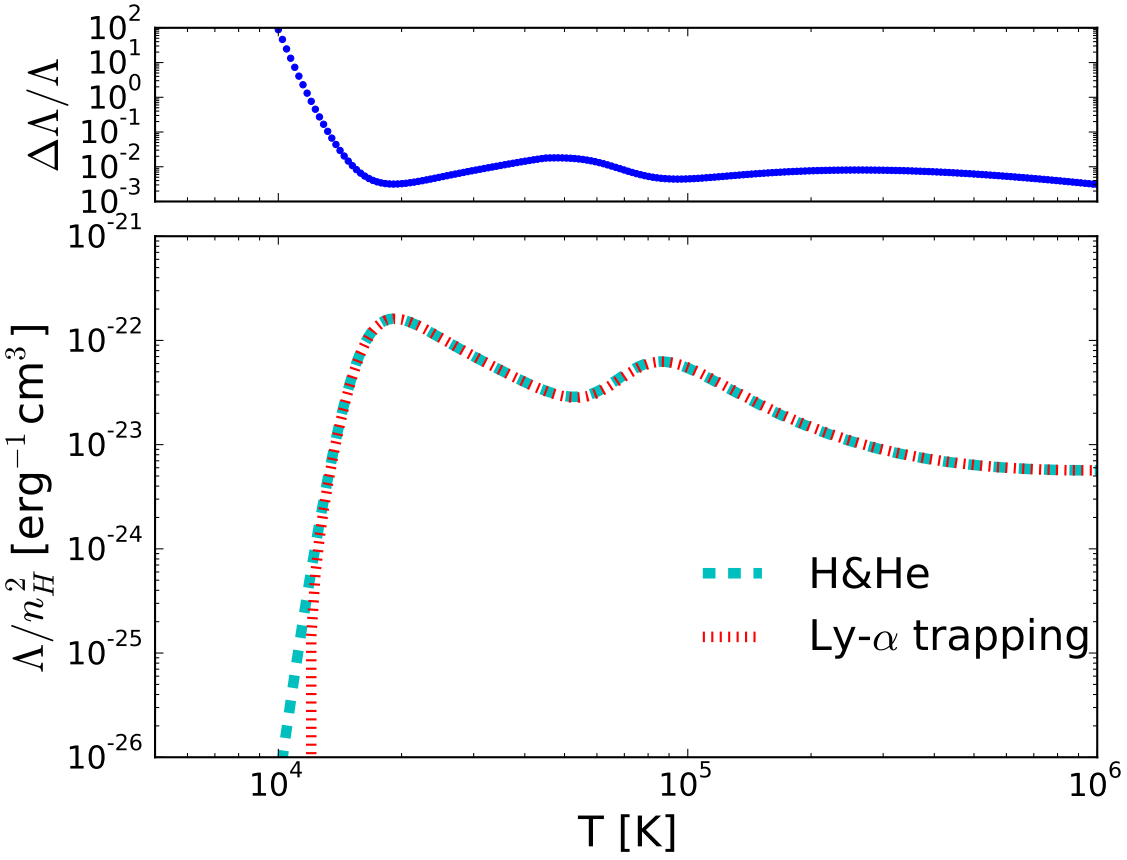

Figure 3.1: Comparison of overall cooling rates in the optically thin and thick approximations. Top panel: The fractional difference in cooling rates between the two cases. Bottom panel: Dependence of the primordial cooling rate per n^2 on temperature in the optically-thin limit (blue dashed) and while considering Lyα trapping (red dotted). Significant differences only exist at $T < 20,000$ K because gas is optically thick to Lyα radiation.

by the radiative cooling of a primordial gas. The virial temperature of the candidate halo that hosts massive BH seed formation is $\gtrsim 8000$ K, which corresponds to a virial mass $M_{\rm vir} \simeq 10^8\ {\rm M}_\odot[(1+z)/10]^{-3/2}$. For such a contraction to proceed the cooling timescale

$$t_{\rm cool} \simeq \frac{1}{n_{\rm e}^2 \Lambda(T)} \frac{3\rho k T}{2\mu m_{\rm p}} \tag{3.9}$$

must be shorter than or similar to the dynamical time $t_{\rm dyn} = (G\rho)^{-1/2}$ (White & Rees, 1978). Here Λ is the cooling function, and $n_{\rm e}$ and ρ are the electron number density and gas density, respectively. Starting at temperatures $T \sim 10^4$ K, hydrogen becomes partially ionized, eventually reaching near complete ionization at $T \sim 1.5 \times 10^4$ K. Thus in halos with virial temperatures near this limit, the assumption that the primordial gas is either completely ionized ($\mu = 0.6$) or neutral ($\mu = 1.22$), in addition to $n_{\rm e}$, could be inaccurate during the collapse and should be tracked.

At low densities $n \lesssim 100\ {\rm cm}^{-3}$, the use of the optically thin cooling rates is valid. However when Lyα radiation from collisional and recombination processes is extremely attenuated at higher densities, the cooling function Λ should decrease as thermal energy cannot be effectively radiated out of the system anymore. When these cooling channels are blocked, a primordial gas can still radiatively cool through the two-photon process.

Figure 3.1 compares the cooling function of atomic metal-free gas in the optically-thin regime and when the gas is optically-thick to Lyα radiation. The trapped Lyα radiation reduces the cooling rates at $T \lesssim 2 \times 10^4$ K, which could result in higher temperatures as the primordial gas cloud collapses. Above this temperature, Lyα trapping and the associated resonance scattering does not occur because spontaneous emission in hydrogen dominates, and furthermore helium de-excitation cooling becomes important at these higher temperatures. Nevertheless, we next investigate this effect further in a separate suite of Lyα radiative transfer calculations as the system is dynamically collapsing, checking how the thermodynamic properties change during this event.

3.3.2 Cosmological Halo Collapse: A Basis for Lyα Transfer

We utilize a collapsing halo from a cosmological simulation as the basis for the Monte Carlo radiation transfer calculations (Section 3.3.3), providing a more realistic environment for the propagation of the Lyα photons. This halo is the most massive in the simulation domain with a total mass $M_{\rm tot} = 5.85 \times 10^7$ M$_\odot$ and a virial radius $r_{\rm vir} = 782$ pc when it catastrophically collapses at $z = 14.664$. This halo mass corresponds to a virial temperature $T_{\rm vir} = 1.17 \times 10^4$ K, which is typical of a metal-free atomic cooling halo that cools and collapses for the first time. The halo does not experience any major mergers for the last 100 Myr of the simulation.

Figure 3.2 shows the evolution of radially-averaged profiles of the gas number density $n_{\rm H}$ and the average electron fraction at a given $n_{\rm H}$ value. The first density profile depicts the system when the maximum $n_{\rm H} \simeq 10^{7.5}$ cm^{-3} (AMR level 15), and then the profiles are shown as the maximum density increases by $\sim$1 dex, finally reaching a maximum $n_{\rm H} \simeq 3 \times 10^{11}$ cm^{-3} (AMR level 20). The density profile generally exhibits a power law $\rho \propto r^{-2.2}$ from the virial radius to $\sim 10^{-3}$ pc. This feature is typical of an isothermal collapse, which happens in this case at $T \simeq 8000$ K, where the gas cooling is limited to atomic processes in the presence of a strong LW radiation field $J_{21} = 10^5$. The inner 1 pc is gravitationally unstable, and its Jeans mass is $\sim 10^5$ M$_\odot$, similar to previous works (e.g. Wise et al., 2008; Regan & Haehnelt, 2009; Shang et al., 2010; Becerra et al., 2015). One exception to the centrally concentrated, spherically symmetric collapse is a clump that fragments ~ 0.1 pc from the densest point, seen as a bump in the density profile, which initially fragments about 5 kyr before the collapse. The electron fraction in the lower panel of Figure 3.2 shows that the free electron fraction decreases with density (i.e. radius) as the recombination rate increases with n^2, eventually saturating at 2×10^{-6}. The electron fraction will play an important role in determining the Lyα emissivity as it is directly related to the electron number density (Equations 3.5 and 3.6).

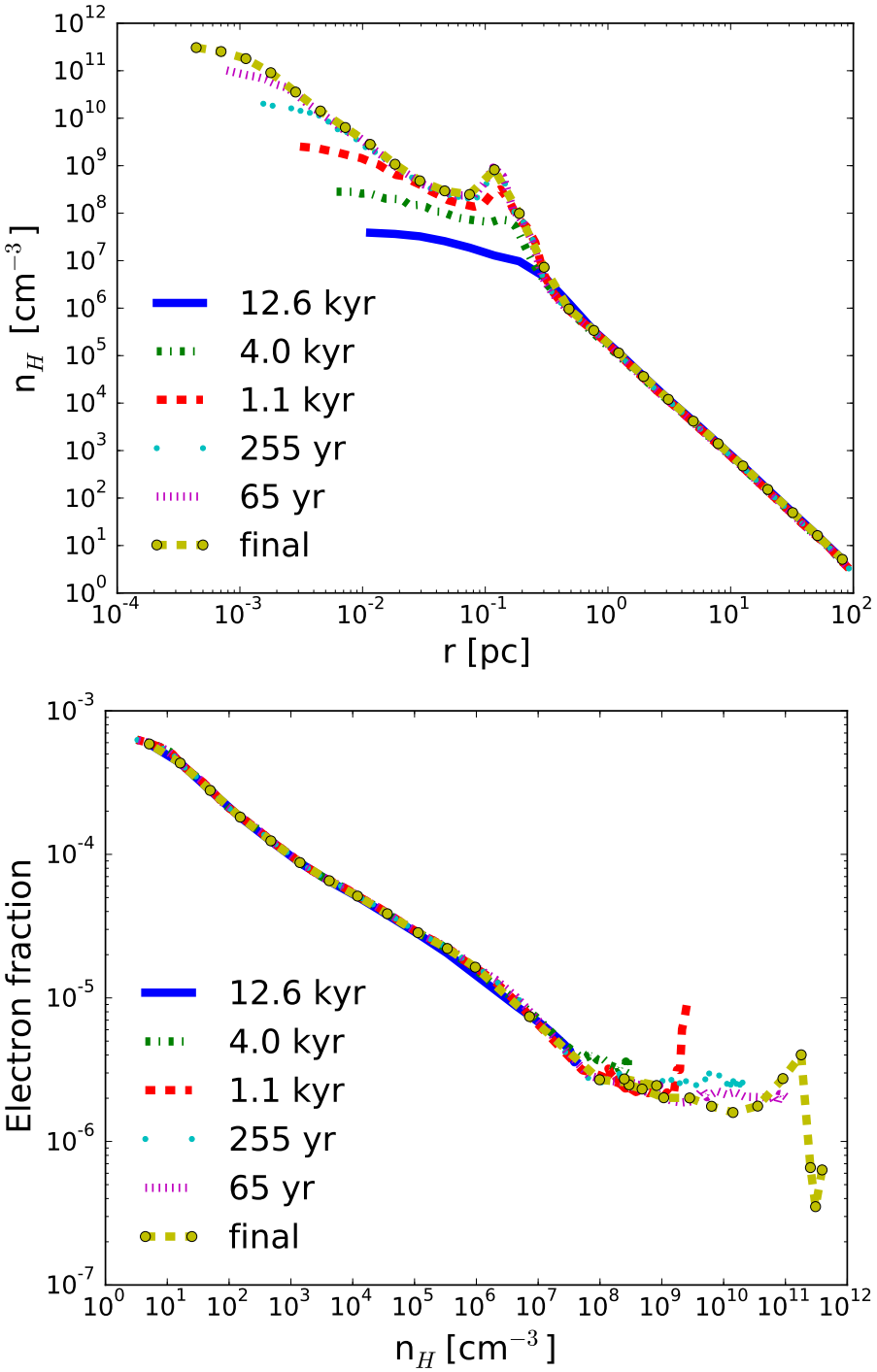

Figure 3.2: Radially-averaged profiles of gas number density (top) and profiles of electron fraction with respect to number density (bottom) at the final output when the collapse reaches $n_H = 3 \times 10^{11}\mathrm{cm}^{-3}$ and 65, 255, 1,100, 4,000, and 12,600 years before this time. The halo density follows a $r^{-2.2}$ power law, appropriate for an isothermal collapse. The bump at 0.1 pc corresponds to lesser overdensity that has fragmented from the main collapsing cloud. The electron fraction drops with density as free electrons are consumed by recombinations.

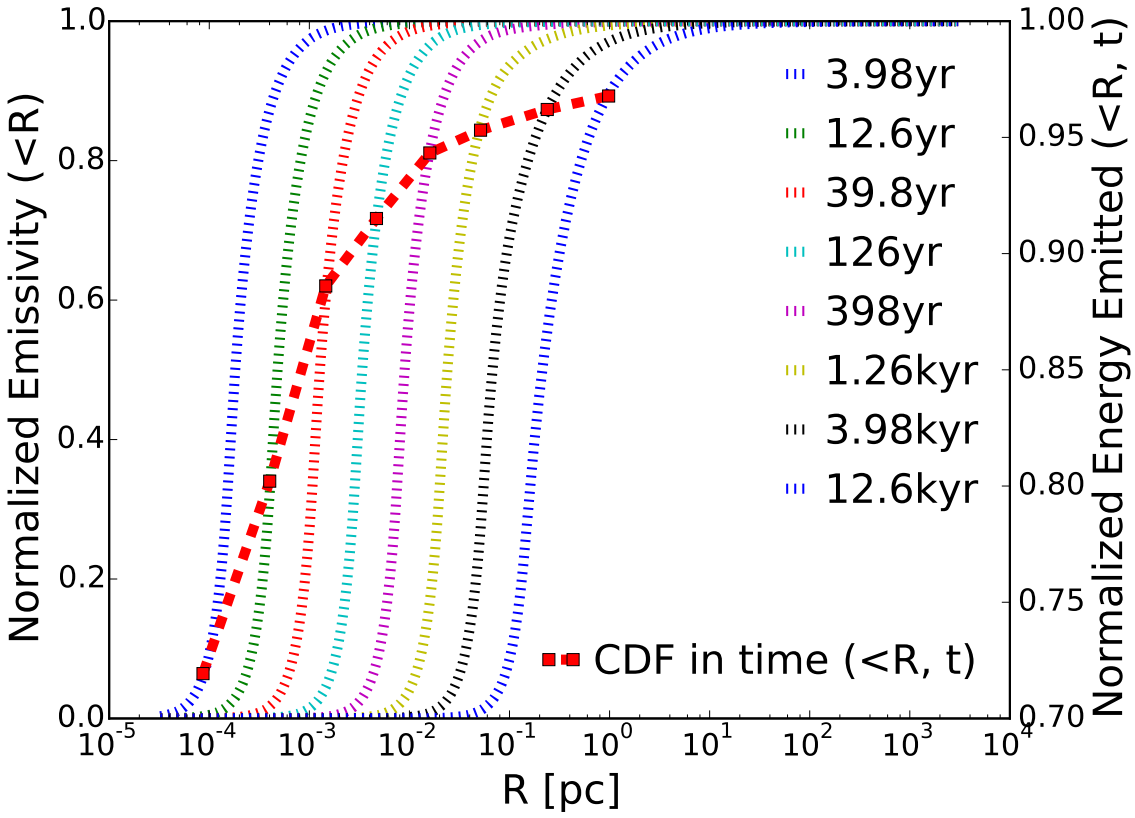

Figure 3.3: *Dotted lines and left axis:* Normalized Lyα emissivity cumulative profiles at eight times (see legend) before the final simulation output. *Dashed line and right axis:* Cumulative amount of Lyα radiation emitted from the time indicated by the intersecting dotted line to 1 Myr before the final output time, i.e. 96% of all Lyα radiation is emitted within 4 kyr of the final collapse.

3.3.3 Monte Carlo Radiation Transfer

Before invoking a radiation transport calculation, we first calculate the Lyα emissivity, using Equations (3.5) and (3.6), in the collapsing halo at eight different snapshots during the event. The bulk of the emission occurs in the central regions, as expected, and we show the cumulative Lyα luminosity,

$$L_{\rm Lya}(< r, t) = \int_0^r \left[\eta^{\rm rec}(t) + \eta^{\rm dcol}(t)\right] dV, \tag{3.10}$$

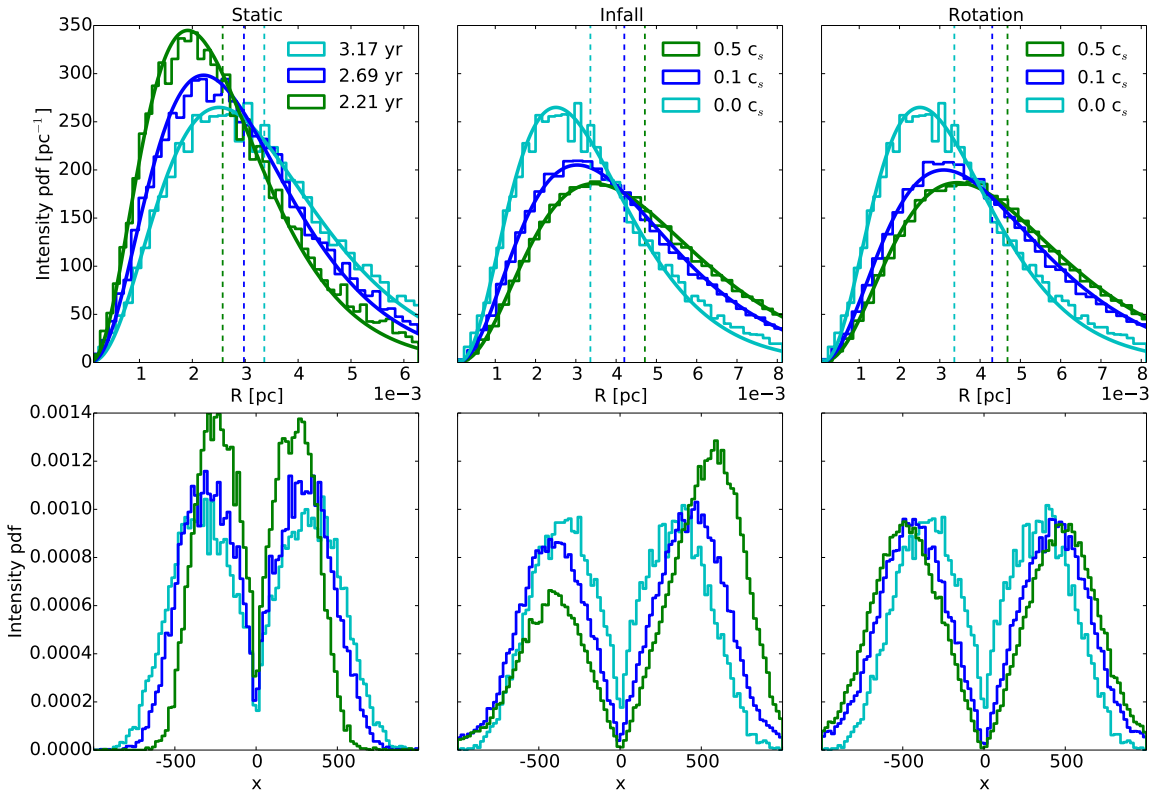

Figure 3.4: Lyα radiation transfer calculations in the uniform density case with a hydrogen number density $n_{\rm H} = 10^8$ cm^{-3}. *Top row:* Lyα radiation intensity as a function of radius for the static case (left), infall case (middle), and rotation case (right), where the vertical lines show the intensity-weighted means. The histograms depict the results from the radiation transport calculation, whereas the smooth curve is a fit to the distribution. The static case shows the radiation propagating outwards, slower than the speed of light due to scattering, at three different times. The infall and rotation cases, shown at $t = 3.17$ yr ($ct = 0.972$ pc), demonstrate that the bulk motion of the gas allows the radiation to propagate farther as the photons experience a greater Doppler shift when they are re-emitted. *Bottom row:* The normalized spectra of Lyα radiation for the same cases shown in the top row. In the static case, the Lyα photons shift away from the line center as time progresses, and the infall and rotation cases show the increased Doppler shifts as the gas bulk motion increases.

as function of radius in Figure 3.3 with the sphere centered on the densest point. One can see that as the inner region collapses, the source of Lyα emission shrinks as the density increases. When the central object becomes gravitationally unstable 12.6 kyr before the final time, 90% (50%) of the emission comes from the central 1.0 (0.2) pc. This radius decreases gradually with time until a sphere of radius 10^{-3} pc generates 99% of the Lyα radiation at the final time.

As the halo is dynamically collapsing, we can calculate the total Lyα energy being emitted throughout its collapse by numerically integrating Equation (3.10) from 1 Myr before the final simulation time to the times shown in Figure 3.3. The red dashed line shows this value, and the differences between adjacent points equal the percentage of total Lyα radiation generated between these two times. For instance, at 4 kyr before the final time, 96% of all Lyα radiation during the collapse is generated after this time, with most of the photons originating within a radius 0.1 pc. This fractional energy decreases with time until 72% of the Lyα radiation originates only 4 yr before the final collapse.

Both the location and timing of the Lyα radiation will aid us in constructing Monte Carlo calculations with the appropriate length and temporal scales. These simulations will explore physical scenarios that gradually increase the realism of the environment through which the Lyα photons propagate. First we will inspect the uniform density case, then the time-independent isotropic case, and finally a collapsing time-dependent isotropic case. The last and most realistic case is used to calculate the effective equation of state, which is an essential ingredient when determining the thermodynamic behavior, and thus possible fragmentation, of the collapsing system.

Uniform density case

The most fundamental case to inspect in a Lyα transfer calculation is a gas parcel with uniform density and temperature. Here we monitor how the radiation propagates from a

Table 3.1: Fitting parameters for the radiation distribution in the uniform density case

Case	$\log(n_{\rm H}/{\rm cm}^{-3})$	a	b_0	b_1
Static	6	3.46	1.28×10^{10}	0.732
	7	3.48	6.67×10^{9}	0.738
	8	3.48	2.42×10^{9}	0.730
	9	3.50	4.15×10^{9}	0.731
Infall	6	2.80	2.04×10^{10}	0.747
	7	2.85	8.86×10^{9}	0.756
	8	2.61	3.40×10^{9}	0.750
	9	2.60	1.24×10^{9}	0.768
Rotation	6	2.77	1.90×10^{10}	0.749
	7	2.72	1.02×10^{10}	0.752
	8	2.77	2.98×10^{9}	0.753
	9	2.78	1.65×10^{9}	0.757

Notes: The parameters apply to Equation (3.11). The static case has zero bulk velocity. The parameters for the infall and rotation case are shown only for the $0.5c_{\rm s}$ cases.

single impulse originating from a point source at $r = 0$. We execute a series of simulations in spherical symmetry with a uniform temperature of 8000 K, which is similar to the temperatures in the atomic cooling halo presented in Section 3.3.2, and four different hydrogen number densities $\log(n_{\rm H}/{\rm cm}^{-3}) = (6, 7, 8, 9)$. The top row of Figure 3.4 shows the radial behavior of the radiation energy distribution in the $n_{\rm H} = 10^8$ cm^{-3} case for the static (left panel), infall (middle panel), and rotation (right panel) cases.

The static case, which is shown at three times, $t = (2.21, 2.69, 3.17)$ yr with the last time corresponding to $t = 10^8$ s and a light travel time $ct = 0.972$ pc, have the radial distributions that are well fit with Gamma distributions, valid for the entirety of the simulation time $t < 10^8$ s,

$$p(r, t) = \frac{r^{a-1}\, e^{-r/b(t)}}{[b(t)]^a\, \Gamma(a)}. \tag{3.11}$$

Here a is a constant and controls the distribution width (i.e. the shape parameter), and $b(t) = b_0 t^{b_1}$ varies with time (i.e. the rate parameter) and controls the length of the tail at larger radii. All variables are expressed in the cgs system. $\Gamma(x)$ is the complete Gamma function, and t is in units of seconds. We do not consider the distribution beyond a light

travel time $r = ct$. These parameters are given in Table 3.1. For such a distribution, the maximum value occurs at $(a-1)b$; the average value is ab; the skewness is $2/\sqrt{a}$. Taking the $n_{\rm H} = 10^8$ cm^{-3} case as an example, we have $ab = 0.281\,t^{-0.272} \times (ct)$. Compared to the optically thin case ($ab = ct$), the Lyα radiation is diluted by a factor of 0.281, and its propagation slows as time progresses, as indicated by the negative exponent. This behavior is apparent in the top-left panel of Figure 3.4, where the distribution migrates to larger radii with its tail becoming longer. Looking at other densities, the shape parameter a is basically unchanged, which is analogous to having a resonant scattering shell with a constant relative thickness. The bottom row of Figure 3.4 shows the relative frequencies of the photons. In the static case, the spectrum is symmetric around the line center ($x = 0$), which is expected, and obeys the Neufeld (1990) profile. The width of the lines depend on the optical depth of the system and the time elapsed. At early times, the photons are nearest to the line center, and they Doppler shift away from the center as they resonate in the neutral hydrogen medium.

Next we inspect the radial distribution of Lyα radiation and its spectra in the infall and rotation cases, which are shown in the middle and right columns of Figure 3.4. Comparing the spectra of the infall cases with $v_{\rm r}/c_{\rm s} = (0.1, 0.5)$ and the static case, we see that the photons are blue-shifted farther away from the line center, which occurs when the infalling gas re-emits the Lyα photons whose relative velocity causes an increase in frequency. Because of the enhanced Doppler shift, the photons scatter less because of the decreased optical depth away from the line center, allowing for the Lyα radiation to propagate farther away from the sphere center, which is seen in a broader radial profile. In the rotation case with $v_\theta/c_{\rm s} = (0.1, 0.5)$, the photons are symmetrically shifted into the wings of the line, which extends the radiation distribution similar to the infall case. These distributions are still nicely fit with a Gamma distribution (Equation 3.11) at various number densities and bulk velocities, and we show the fitting parameters in Table 3.1 alongside the static case. Both infall and rotation cases have larger b parameters, indicating that the radiation is less

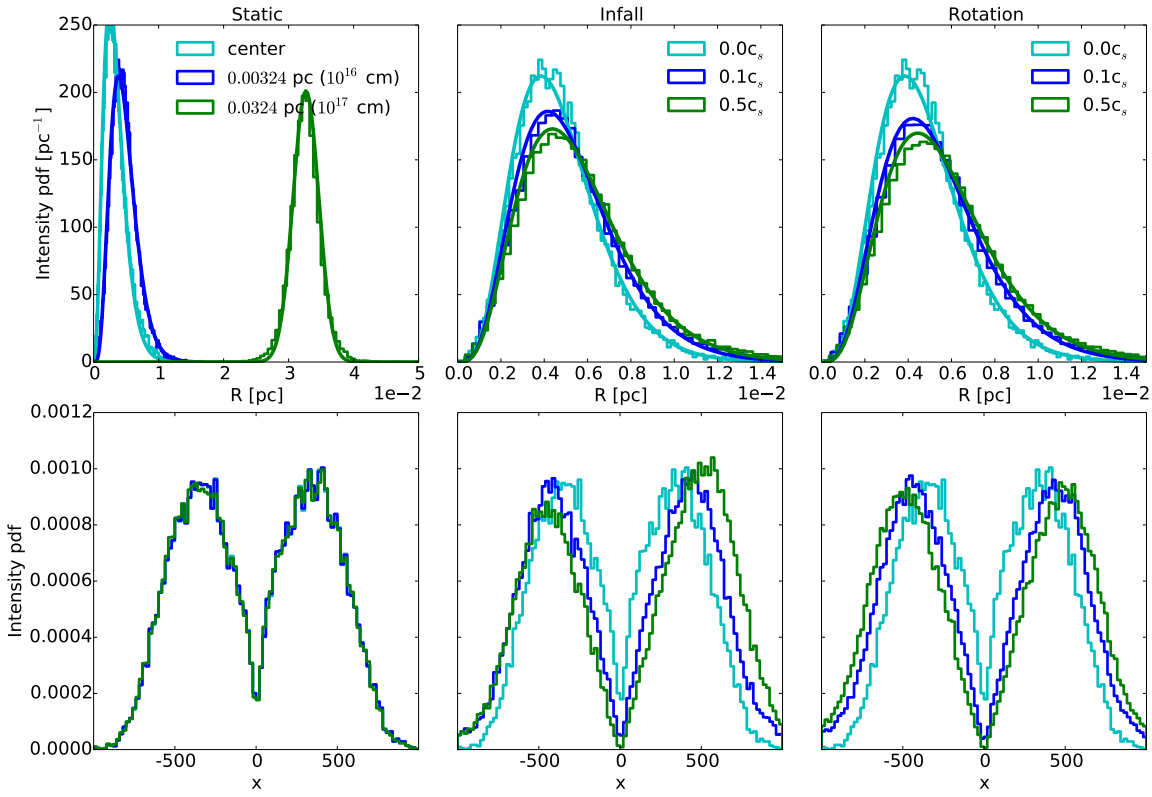

Figure 3.5: Same as Figure 3.4 but for the time-independent isotropic case that propagates Lyα radiation through a spherically symmetric halo with its quantities taken from a cosmological simulation. The static case (left) shows the radiation distribution and spectra at $t = 10^8$ s when the photons are generated at the halo center and in two shells with radii $r = 0.00324$ pc $(10^{16}$ cm) and 0.0324 pc $(10^{17}$ cm). The radiation preferentially propagates outward because of the density gradient. The infall (center) and rotation (right) cases are shown at the same time with the photons generated in a shell of radius $r = 0.00324$ pc $(10^{16}$ cm) for speeds $v/c_{\rm s} = (0.1, 0.5)$. Their distributions and spectra show similar behavior as the uniform density case with the photons being Doppler shifted as the velocity increases, resulting in a wider radiation distribution.

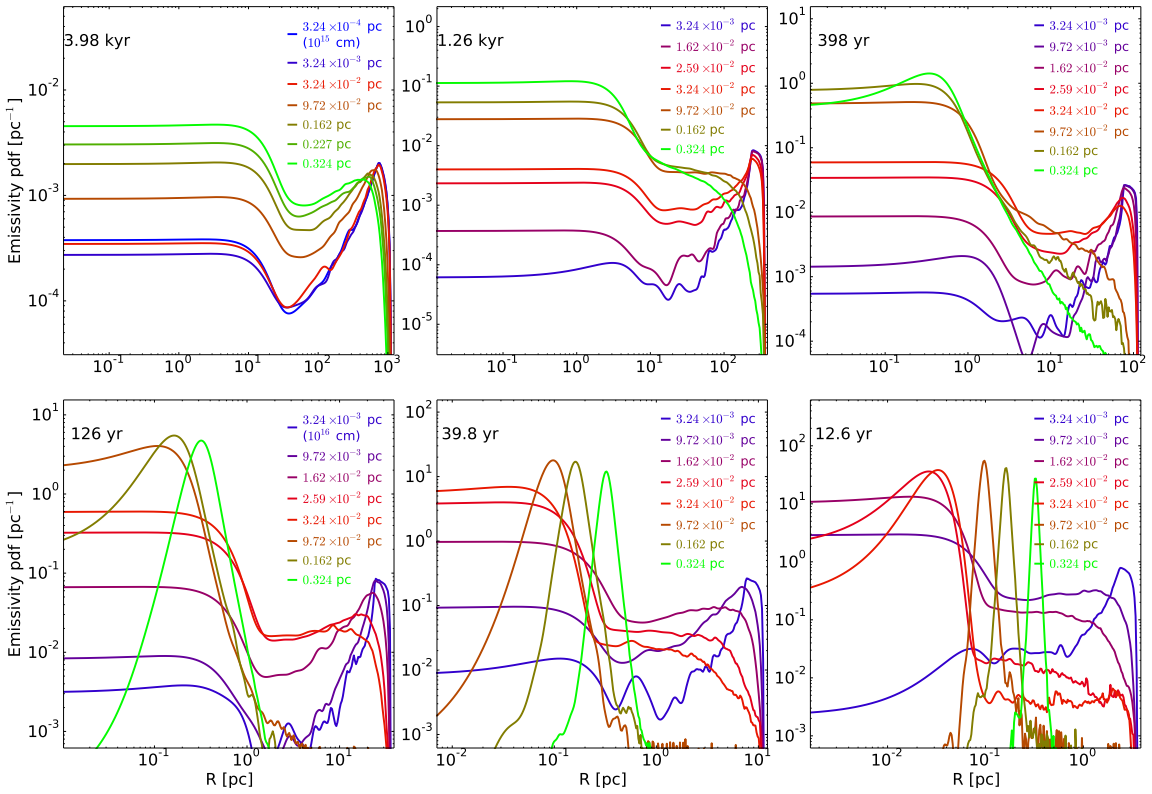

Figure 3.6: Radial distributions of Lyα emissivity sourced from a subset of individual shells in the time-dependent isotropic case at six different times before the final collapse. The lines are colored by their shell radius and track the propagation from that initial radius to the final state. At early times, there is enough time for the emissivities to reach an equilibrium in the core while some fraction escape into the outer regions of the halo. At later times, the distributions from the larger shells do not have time to propagate far from their origin, while the smaller shells contribute the most to the Lyα radiation field in the inner core with radius 0.1 pc.

trapped in the gas.

Because a single impulse of radiation sourced these radial distributions, we can increase the realism of the calculation by integrating these radiation profiles with respect to time in the range $t = 0 \rightarrow \mathcal{T}$, which represents the center constantly emitting photons. Integrating Equation (3.11), we find that the radiation profile transforms into

$$P(r, \mathcal{T}) = \int_0^{\mathcal{T}} p(r, t)\, dt = \frac{r^{1/(b_1-1)}\, \Gamma(a - 1/b_1, (r/b_0)\, \mathcal{T}^{-b_1})}{\mathcal{T}\, b_1\, b_0^{1/b_1}\, \Gamma(a)}, \tag{3.12}$$

where $\Gamma(x, y)$ is the incomplete Gamma function. The resulting distribution has an intensity-

averaged radius $\mathbb{E}(r) = ab/(1 + b_1)$ that is proportional to the distribution coming from a radiation impulse. In this case, the scattering and trapping of Lyα radiation and its diminished radial propagation declines with time as $t^{-\alpha}$, where $\alpha = 2.4 - 2.7$, in the static case.

Time-independent isotropic case

Now that we have established the behavior of Lyα radiation transport in a uniform density and temperature case, we turn our attention to the time-independent isotropic case. Here we consider a spherically symmetric system, taking the radial profiles of density and temperature, along with the average electron fraction as a function of density, from the atomic cooling halo in the cosmological simulation (Section 3.3.2), 4.0 kyr before the final output when the maximum number density $n_{\rm H} = 3 \times 10^8$ cm^{-3}. In this case, we consider three cases of Lyα radiation generation: from the center of the halo and from two concentric shells with radii $r = 0.00324$ pc (10^{16} cm) and 0.0324 pc (10^{17} cm). We do not utilize the velocity information from the simulation but consider the same velocity setups as the uniform density case: static, infalling, and rotation, where the latter two configurations have $v/c_{\rm s} = (0.1, 0.5)$. We allow these photons to propagate according to the scattering radiative transfer equation in a spherically symmetric system.

Figure 3.5 shows the resulting radiation radial distribution (top panels) and spectra (bottom panels) at a time $t = 10^8$ s $= 3.17$ yr, corresponding to a light travel time $ct = 0.972$ pc. Focusing first on the static case (left column), the Lyα radiation propagates away from the center with a maximum at 0.00259 pc (8×10^{15} cm), while the photons from the radiating shells at $r = 0.00324$ pc (10^{16} cm) and 0.0324 pc (10^{17} cm) preferentially migrates outward because of the density gradient. These distributions are again well fit with a Gamma distribution (Equation 3.11), similar to the uniform density case but with $a(t) = a_0 t^{-a_1}$ instead of being a constant. The fitting parameters for the three

Table 3.2: Fitting parameters for the radiation distribution in the static isotropic case

Case	r [cm]	a_0	a_1	b_0	b_1
Static	0	5.99×10^7	0.801	6.90×10^{-7}	2.448
	10^{16}	7.87×10^8	0.916	1.24×10^{-7}	2.525
	10^{17}	6.48×10^9	0.996	1.21×10^{-3}	2.162
Infall	0	3.46×10^2	0.259	2.26×10^6	1.180
	10^{16}	3.98×10^2	0.265	1.71×10^6	1.193
	10^{17}	7.48×10^2	0.291	3.44×10^6	1.162
Rotation	0	2.98×10^2	0.248	1.90×10^6	1.156
	10^{16}	3.82×10^2	0.280	2.02×10^6	1.176
	10^{17}	8.44×10^2	0.301	2.98×10^6	1.142

Notes: The parameters apply to Equation (3.11) but with $a(t) = a_0\, t^{-a_1}$. For $r = 0$, the Lyα radiation originates at the halo center, and for the non-zero radii, it originates from shells of those radii. The static case has zero bulk velocity. The parameters for the infall and rotation case are shown only for the $0.5c_{\rm s}$ cases. The associated fits are accurate for $t < 10^9$ s.

cases are given in Table 3.2. The preference toward outward propagation can be quantified by inspecting the skewness $(2/\sqrt{a})$ of these distributions, which are in the range 0.2–0.4. The spectra for the central and shell sources have similar spectra, as expected, because they are shown at the same integration time and the velocities are the same.

Both the radial distribution of Lyα radiation and the spectra of the infall and rotation cases behave similarly to their counterparts in the uniform density case. The middle and right columns of Figure 3.5 show these respective cases at a time $t = 10^8$ s with the photons being generated in a shell of radius $r = 0.00324$ pc $(10^{16}$ cm). We also consider the cases where photons are generated in the center and a larger shell of radius 0.0324 pc $(10^{17}$ cm), whose fitting parameters are shown in Table 3.2 but not shown in the Figure. The relative velocities of the gas cause a Doppler shift, allowing the photon frequencies to migrate away from the line center, with a tendency toward a blueshift in the infall case and symmetric shifts in the rotation case. This effect increases their mean free path, extending the radial profiles. As the photons propagate outward into the more diffuse regions (recall $\rho \propto r^{-2.2}$) of the halo, they will scatter less frequently, eventually free streaming away from the halo center.

Time-dependent isotropic case

We now consider the case where the halo is dynamically collapsing, whereas previously we restricted the integration times to 10^8 s that is comparable to the light-crossing time of the inner parsec. This time-dependent calculation is similar to the time-independent calculation; however we utilize six outputs from the cosmological simulation that are evenly log-spaced in time, starting at 3.98 kyr before the collapse. The density profiles are approximately isothermal with $\rho \propto r^{-2.2}$ at all times with the maximum density increasing from 3×10^8 cm^{-3} to 3×10^{11} cm^{-3} during this time. At each time, 20 shells radiate Lyα photons, which are equally log-spaced in radius ranging from 3.24×10^{-5} pc (10^{15} cm) to 3.24 pc (10^{19} cm). The output times t_i are given in Table 3.3. The largest shell encloses nearly all of the Lyα radiation that was depicted in Figure 3.3. The major improvement upon the previous cases is that we integrate over the resulting radiation distribution from each shell to compute a cumulative radiation distribution for the entire halo.

Starting at the earliest time, the shells radiate for a time equal to the duration between outputs (i.e. $t_i - t_{i+1}$). We track the radial distribution of the photons from each shell, where Figure 3.6 shows a subset of the 20 shells, allowing us to inspect the propagation behavior from each radiation origin. At the earliest time (3.98 kyr), the radial distributions from each shell have similar shapes. They have plateaus at small radii, which have reached an equilibrium between emission and scattering out of the center. The local maxima at $r \simeq 300 - 600$ pc represent the photons that have escaped the inner regions by scattering many times and driving the frequency into the wings of the spectrum, and they are freely streaming outward through the diffuse outer regions. As the collapse progressively accelerates, the dynamical time decreases, giving less time for the photons to propagate through the pre-galactic medium. This behavior can be seen through the steadily decreasing radiation distribution at large radii at $t = 1260$ and 398 yr for the largest shells. Eventually in the later times, the distributions for the largest shells transform into Gamma distributions

Table 3.3: Output times and range of radii of the radiating shells in the equation of state calculation

Case i	Time t_i [yr]	Shell radii range [10^{16} cm]
0	3,980	10 – 100
1	1,260	5 – 100
2	398	3 – 100
3	126	2 – 100
4	39.8	1 – 100
5	12.6	1 – 100

as the integration times shorten to $\sim 10^8$ s. However for the radiation originating from intermediate radii (e.g. $r = 0.00972$ pc and 0.0162 pc at $t = 12.6$ yr), the Lyα photon distribution still have a plateau at small radii.

3.3.4 Effective equation of state with Lyα scattering

The radiation distributions from individual shells informs us how the radiation transports given an origin, but at some given time, the overall Lyα emissivity distribution is the key quantity in determining the coupling between the Lyα photons and the neutral medium. Ultimately, we can compare the radiation distribution from the transport calculation to the optically-thin (free streaming) case to calculate the reduction in the radiative cooling rate from collisional excitations and ionizations.

Figure 3.7 shows the resulting Lyα normalized emissivities as a function of radius at several times. We only consider the shells within the radius range given in Table 3.3 to reduce the computation, and we have found that the shells outside the given ranges do not contribute to the overall emissivity. We first start by calculating the total emissivity from the first time interval ($t_0 \rightarrow t_1$), shown as the blue line in the Figure. Then at the next output time t_2, we calculate the total emissivity in the next interval ($t_1 \rightarrow t_2$) and add it to the previous profile. This process is repeated until we reach the final output simulation time. In other words, at some time t_n, we construct the time-integrated emissivity profile

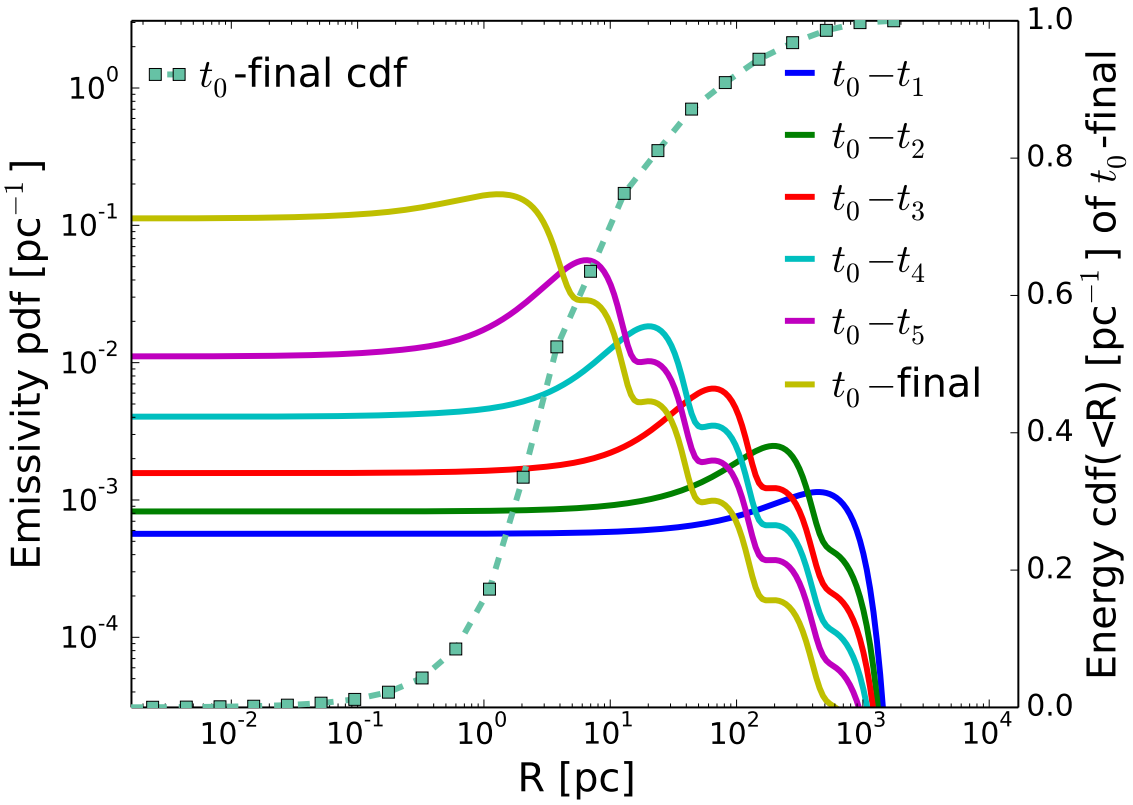

Figure 3.7: The total Lyα emissivity integrated (Equation 3.13) from all of the shells shown in Figure 3.6 and all times from t_0 to t_i. The yellow (top) solid line shows the Lyα emissivity at the final time of the simulation. The dashed line with square points depicts the cumulative Lyα emissivity at the final time with 50% (90%) of it being contained within 3 pc (50 pc).

by discretely adding each time interval:

$$\eta^{\rm total}(t_{\rm n}, r) = \sum_{i}^{n} \eta(t_{\rm i} \rightarrow t_{\rm n}, r) = \sum_{i}^{n} \sum_{\rm shells} \eta^{s}(t_{\rm i} \rightarrow t_{\rm n}, r) \tag{3.13}$$

where n is an integer in the interval $[0, 5]$, and its maximum corresponds to the number of simulation outputs considered. During the summation, we smooth the Monte Carlo results with the kernel density estimation (KDE) method in `scipy` with the default parameters (Jones et al., 2001). However because n is small, we have numerical artifacts at large radii from the addition of the local maxima from previous times (i.e. $i < n$), but they do not affect the accuracy of the final emissivity profile.

As the halo collapses, the Lyα emissivity progressively becomes more centrally concentrated because of the increased photon generation rate from the higher densities. At the final time (yellow line in Figure 3.7) when the maximum density $n_{\rm H} = 3 \times 10^{11}$ cm^{-3}, we see that the bulk of the Lyα is contained within $r < 10^{19}$ cm $\simeq 3$ pc that is approximately the Jeans length of the central object. At this radius, the number density $n_{\rm H} \simeq 10^{4}$ cm^{-3}, above which the medium becomes prone to Lyα scattering and a reduction in radiative cooling. Also we show cumulative emissivity profile within a radius R

$$\eta(< R, t_{\rm final}) = \int_{0}^{R} \eta^{\rm total}(t_{\rm final})\, dV \tag{3.14}$$

in Figure 3.7 as the dashed cyan line, illustrating that 50% (90%) of the Lyα radiation is contained within $\sim$3 pc (50 pc).

Finally with the Lyα emissivity profile $\eta^{\rm total}$ at the final time $t_{\rm final}$, we can determine how much the radiative cooling is reduced. We first convert this profile into a function of density by using the halo radial density profile (Figure 3.2). Then we take the difference between our Monte Carlo radiation transport result and the optically-thin emissivity $n^{\rm src}$ (see Equations 3.5 and 3.6) and convert that into an effective heating rate as a function of

density. Figure 3.8 depicts the resulting effective equation of state up to a number density $n_{\rm H} = 10^{12}$ cm^{-3} that is approximately the maximum density in the simulation. Here we take the initial temperature at $n = 0.1$ cm^{-3} to be $T = 9000$ K. As the gas condenses, Lyα radiation becomes more coupled to the neutral gas, reducing its cooling rate with respect to the optically-thin rate, resulting in the gas gradually heating to 5×10^4 K at $n_{\rm H} = 3 \times 10^4$ cm^{-3}. However at higher densities (smaller radii), the gas cools back to 10^4 K because the Lyα emissivity plateaus within 3 pc, corresponding to $n_{\rm H} = 10^4$ cm^{-3} in the density profile. This heating from partially Lyα trapping at moderate densities is in stark contrast to the optically-thin case, where the gas slowly cools from 9000 K to 7000 K (green dashed line). The gas starts to cool because the optically thin cooling rate increases as $n_{\rm e} n_{\rm HI}$ or $n_{\rm e} n_{\rm HII}$ for collisional excitation and recombination, respectively, while the Lyα emissivity from the Monte Carlo calculation has plateaued. The combination of this saturation and increasing optically-thin cooling rate ultimately results in the dense gas cooling back below 10^4 K. We then differentiate this effective equation of state to obtain the adiabatic index $\gamma = 1 + d\ln T / d\ln \rho$ for an ideal gas (red dashed line in Figure 3.8). As the gas heats, γ increases from unity to ~4/3 at $n_{\rm H} = 10^4$ cm^{-3}, suddenly decreases to ~4/5 at $n_{\rm H} = 10^6$ cm^{-3}, and then recovers back to unity with increasing density.

In Figure 3.8, we compare our equation of state to the one analytically derived from spherical symmetry in Spaans & Silk (2006), shown as a dashed black line, that has the form

$$\gamma - 1 \approx -\frac{\frac{1}{2} + \frac{7}{18} B n_1^{7/18}}{\log(C n_1^{0.5}) + B n_1^{7/18}}, \tag{3.15}$$

where $B \approx 0.47$ cm$^{7/6}$, $C \approx 10^{-34}$ cm$^{3/2}$, and n_1 is 100 times the number density in units of cm^{-3} (see Latif et al., 2011, for the motivation to boost n_1). This result describes a smooth but quick transition from isothermal to adiabatic ($\gamma = 5/3$). It diverges for high number densities and must be limited to 5/3 at high densities. The bulk of the increase in γ comes between $\log(n_{\rm H}/{\rm cm}^{-3}) = 4 - 5$, whereas our results starts to increase from unity

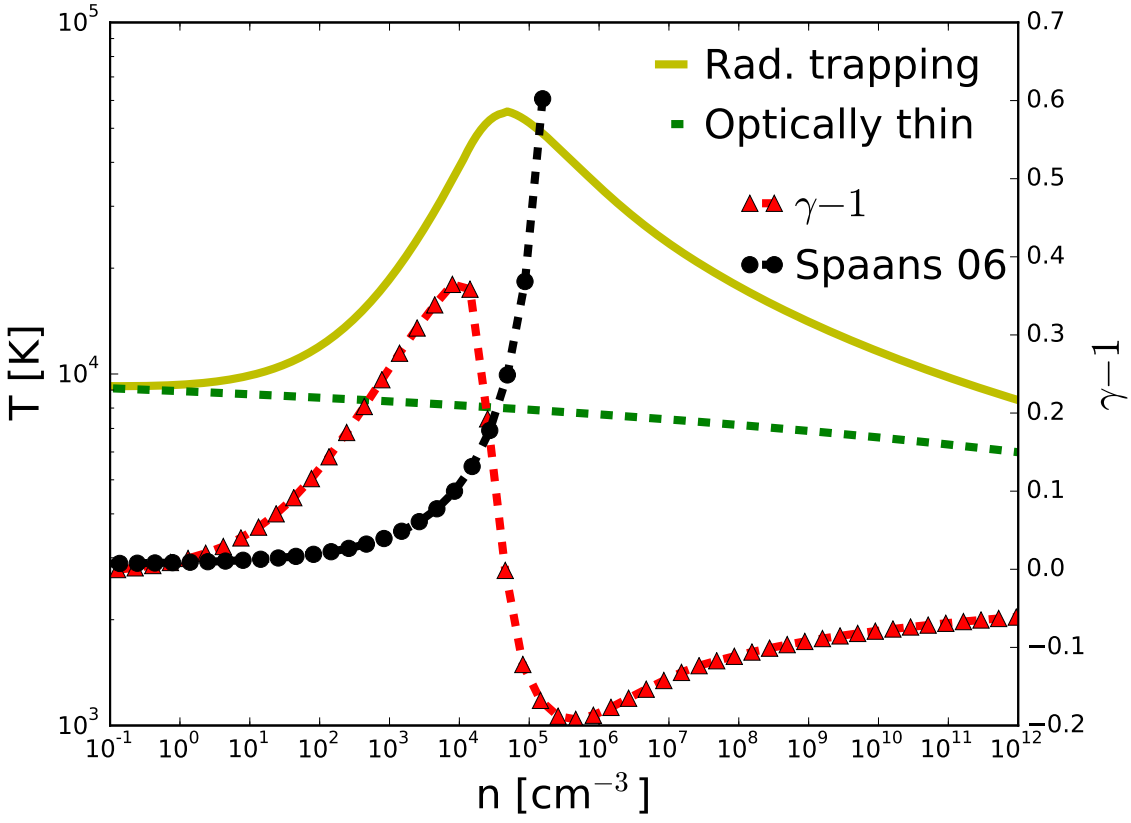

Figure 3.8: *Left axis:* Effective equation of state derived from the Lyα radiation transfer calculation (solid yellow) and optically-thin cooling rates (green dashed). The gas heats from the initial temperature of 9,000 K to 50,000 K by $n_{\rm H} = 3 \times 10^4$ cm^{-3} from Lyα trapping and then cools to 10^4 K at higher densities. *Right axis:* The red dashed line shows the adiabatic index $\gamma - 1$ of the effective equation of state ($p \propto \rho^\gamma$; $T \propto n^{\gamma-1}$) from this work. With increasing density, it increases from $\gamma - 1 = 0$ (isothermal) to 1/3 at $n = 10^4$ cm^{-3}, coming from the suppressed Lyα cooling due to radiation trapping. It rapidly becomes negative above this density, illustrating the renewed ability to cool. The black dashed line shows the adiabatic index from the analytical work of Spaans & Silk (2006) that diverges above 10^5 cm^{-3} where it should be limited to 5/3, appropriate for an adiabatic primordial atomic gas. Our model predicts that the collapsing gas will heat at comparatively lower densities.

around $100\ \mathrm{cm}^{-3}$, only reaching $\sim$4/3 at $10^4\ \mathrm{cm}^{-3}$. Our effective equation of state is still valid for high number densities when the cloud is optically thick, whereas the Spaans & Silk result breaks down and must be approximated with an adiabatic equation of state.

3.4 Conclusions and Discussion

We have utilized a suite of Monte Carlo Lyα radiative transfer calculations to study the effects of Lyα radiation trapping in a metal-free pre-galactic halo, which we have extracted from an AMR cosmological simulation, using ENZO. In this thesis, we have quantified the delayed radiation propagation and associated reduced radiative cooling within these objects that could be precursors of direct collapse black holes or dense stellar clusters. From these calculations, we have estimated an effective equation of state for this collapsing primordial gas. The key results of this thesis are summarized below.

1. By introducing a Lyα trapping model, we found that the primordial cooling rates are reduced below 20,000 K at densities above 100 cm^{-3}. Above this temperature, cooling from spontaneous emission in hydrogen dominates, and below this density, the gas is effectively optically thin to Lyα radiation.

2. The majority of the Lyα photons are generated within a radius of $\sim$1 pc and $\sim$1 kyr before the collapse of the central primordial gas cloud inside of a pre-galactic atomic cooling halo. This gas is optically thick to Lyα radiation, which is trapped within the cloud, but it eventually escapes from the cloud. Thus, the optically-thin cooling rates overestimate the actual cooling behavior of this collapsing gaseous object.

3. When we consider a static density field, whether it be uniform or an isothermal profile, the Lyα radiation outward propagation is delayed by resonance scattering, resulting in a emissivity radial profile that is well described by a Gamma distribution. Subsonic inward or rotational bulk velocities allow the Lyα photons to shift into the

wings of the line profile but have little effect on reducing the amount of trapping.

4. We find that the Lyα radiation continues to be trapped as the halo collapses to high densities. Here we applied the static model results to a dynamically collapsing halo in an approximate manner, where we transport the Lyα radiation from shells at six different epochs during the collapse. However, the radiative cooling rates are not fully suppressed with the adiabatic index rising from unity to ∼4/3 at $n_{\rm H} = 10^4\ {\rm cm}^{-3}$ with the temperature increasing to 50,000 K at the same number density. At higher densities, the Lyα emissivity saturates while cooling rates from collisional excitation and recombination increase as n^2, allowing the gas to cool back to 10,000 K. This thermodynamic track results in a heated envelope with a cooled core that will form either a dense stellar cluster or a supermassive star, eventually forming a massive black hole seed.

We have seen that Lyα radiation trapping alters the thermal properties of the collapsing system that will change its Jeans mass, ultimately controlling the fragmentation mass scale and resulting collapsed object. The Bonnor-Ebert mass (Bonnor, 1956; Ebert, 1955) considers an external pressure $P_{\rm ext}$ around an isothermal gaseous cloud, which is given by

$$M_{\rm BE} = 1.18 \frac{c_{\rm s}^4}{G^{3/2}} P_{\rm ext}^{-1/2}\ {\rm M}_\odot \tag{3.16}$$

$$\simeq 20 T^{3/2} n^{-1/2} \mu^{-2} \gamma^2\ {\rm M}_\odot \tag{3.17}$$

where the second expression is calculated by setting the external pressure to the local pressure. Previous studies of the direct collapse black hole pre-cursors become Jeans unstable at a Bonnor-Ebert mass around 10^5 M$_\odot$ at a radius of ∼1 pc (e.g. Bromm & Loeb, 2003; Wise et al., 2008; Regan & Haehnelt, 2009), which is approximately where we find the primordial gas to be prone to Lyα trapping. We find that the gas heats to 50,000 K at this scale that is 5–6 times hotter than the typical 8000 K temperature found in studies using

optically-thin cooling rates. This heating increases the Bonner-Ebert mass at this scale by an order of 10–15, which will hinder the initial collapse until the central object can accumulate additional gas. However after the cloud becomes gravitationally unstable, it will cool back down to 8,000–10,000 K, resulting in a cool dense core surrounded by an envelope that is 5 times hotter. This additional external pressure may drive a decrease in the Bonnor-Ebert mass at higher densities.

One shortcoming of our work is the post-processing treatment of the Lyα radiation transport, where the additional heating does not affect the collapse. In the time-dependent case, we utilized the temperature profile from the cosmological simulation that was calculated with the optically-thin cooling rates. But any Lyα feedback will change the gas temperature and thus neutral fraction that will ultimately alter the Lyα radiation field. When the gas is heated above the optically-thin solution, the Lyα photons will scatter to the wings of the line profile faster and overall will have longer mean free path. Additionally, we have assumed spherical symmetry, whereas in a full three-dimensional setup with coupled Lyα transfer anisotropic structures, such as bubbles or channels, can form during the collapse (e.g. Smith et al., 2015), which could have similar anisotropic behavior as ionizing radiation transport in massive star formation (e.g. Krumholz et al., 2009; Rosen et al., 2014). This anisotropy may alter the accretion flows onto and throughout the collapsing gas cloud. For instance, Lyα trapping may favor some directions than others, creating warmer channels and inhibiting any accretion through those solid angles.

Such feedback loops would create a complex interplay between accretion flows, shocking onto the Jeans unstable gas cloud, Lyα radiation trapping, and the resulting thermal and hydrodynamic response. This will likely alter the angular momentum and entropy of the infalling gas and could have an effect on the outcome of the collapsing object – the spin and mass of a direct collapse black hole, or the star formation efficiency and size of a dense stellar cluster. As computational methods and hardware improve, it is becoming feasible to

perform Lyα radiation transport coupled with the hydrodynamics to resolve these complexities arising from the aforementioned feedback processes (e.g. see a discussion in Smith et al., 2017) that will bring us closer to resolving the nature of the initial central object of these highly irradiated, metal-free, pre-galactic halos.

3.5 Appendix: Cooling with approximate Lyα radiative transfer

3.5.1 Average number of scattering events

We base our treatment of Lyα radiation trapping in the radiative cooling rate calculation described and presented in Sections 3.2.1 and 3.3.1, respectively, on the Omukai (2001) model. In order to calculate the average number of scattering events before escaping the system, we solve the radiative transfer equation for Lyα photons with the Eddington approximation in the isotropic limit (Adams et al., 1971) that describes the evolution of intensity J as a function of optical depth τ and frequency shift $x \equiv (\nu - \nu_0)/\Delta\nu_{\rm D}$ as

$$\frac{\nabla^2 J(\tau, x)}{3H^2(a, x)} = J(\tau, x) - \int_{-\infty}^{\infty} J(\tau, x')\, q(x, x')\, dx' - S(\tau, x), \tag{3.18}$$

where H is the normalized Voigt profile (Equation 3.4). Recall that $a \equiv A_{12}/4\pi\Delta\nu_{\rm D}$ (Section 3.2.1). Here $q(x, x')$ is the normalized redistribution function that describes the frequency shifts during scattering events in the atom's rest frame (Hummer, 1962). The source function $S(\tau, x)$ describes the generation of Lyα radiation at some optical depth and frequency. Using a Taylor expansion of the redistribution functions (e.g. Adams et al., 1971; Harrington, 1973; Rees & Ostriker, 1977), the radiation transfer equation can be formulated as a Poisson equation,

$$\frac{\partial^2 J}{\partial \tau^2} + \nabla^2 J = -3\frac{S(\tau, x)}{4\pi}. \tag{3.19}$$

The equation is solved in spherical symmetry with the boundary condition

$$\frac{\partial J(x,\tau)}{\partial \tau} = -\frac{3}{2} H(a,x) J(\tau,x), \tag{3.20}$$

describing a system with $\tau = 0$ at the center and $\tau = \tau_0$ at the outer boundary $r = R$. Considering an isotropic source at some optical depth $\tau_{\rm s}$, the analytical solution (for the complete derivation, see Appendix C in Dijkstra et al., 2006) to Equation (3.19) is,

$$J(\tau,\sigma) = \frac{\sqrt{6}}{16\pi^2 R} \frac{1}{\tau_0 \tau \tau_{\rm s}} \sum_{n=1}^{\infty} \sin(\lambda_{\rm n}\tau) \sin(\lambda_{\rm n}\tau_{\rm s}) \frac{\exp(-\lambda_{\rm n}|\sigma|)}{\lambda_{\rm n}}, \tag{3.21}$$

where $\sigma \equiv (2\pi/27)^{1/2} x^3/a$. The values $\lambda_{\rm n}$ are the coefficients in the solution to the equation,

$$\frac{d^2 J}{d\tau^2} + \lambda^2 J = 0 \tag{3.22}$$

that has solutions in the form $J_n = A\cos(\lambda_{\rm n}\tau)$ (Unno, 1952; Harrington, 1973). After determining the values of λ and thus the solution to J, it can be integrated from the center to the optical depth τ_s and compared to the intensity J at the outer boundary. The respective ratio of these two quantities relates the number $N_{\rm sc}$ of scatterings inside a sphere with optical depth τ_s to the total number $N_{\rm bd}$ of photons emitted from boundary τ_0

$$\begin{aligned} \frac{N_{\rm sc}(x,\tau_s)}{N_{\rm bd}(x,\tau_s)} &= \frac{\int_0^{\tau_0} 4\pi\tau^2 J(\tau,\sigma)\, d\tau}{J(\tau_0,\sigma)} \\ &= \frac{\mathcal{L}(x,\tau_0,\tau_{\rm s})/[2i\tau_0 A^2(x,\tau_0)]}{\sin(\pi\tau_{\rm s}/\tau_0)/\{[3H(a,x)][\cos(\pi\tau_{\rm s}/\tau_0)+\cosh(\sigma/\tau_0)]\}}, \end{aligned} \tag{3.23}$$

where

$$\mathcal{L}(x,\tau_0,\tau_{\rm s}) \equiv {\rm Li}_2[A(x,\tau_0)\,(|\sigma| - i\tau_{\rm s})] - {\rm Li}_2[-A(x,\tau_0)\,(|\sigma| + i\tau_{\rm s})] \tag{3.24}$$

Table 3.4: Coefficients A_{ij} for the exponential fit to the number of scattering events in Equation (3.27)

	$i=0$	$i=1$	$i=2$	$i=3$	$i=4$	$i=5$
$j=0$	2.597(0)	1.193(0)	4.021(–2)	2.375(–3)	8.825(–5)	–6.167(–6)
$j=1$	–2.000(0)	–3.342(–1)	–9.067(–3)	–3.954(–4)	1.008(–5)	
$j=2$	3.400(–1)	3.150(–2)	7.111(–4)	2.748(–7)		
$j=3$	–2.422(–2)	–1.351(–3)	–1.157(–5)			
$j=4$	8.436(–4)	2.059(–5)				
$j=5$	–1.139(–5)					

Note: The values are in scientific notation with the exponent in parentheses.

and

$$A(x,\tau_0) = \frac{\pi}{\tau_0}\left(1 - \frac{2}{3H(a,x)\tau_0 + 2}\right). \tag{3.25}$$

The function $\mathrm{Li}_n(z) \equiv \sum_{k=1}^{\infty}(z^k/k^n)$ is an $n=2$ polylogarithmic function defined in the complex plane. From this solution, we can integrate over the frequency x (or its equivalent σ) and optical depth τ_s from the center to the boundary, determining the average number of scatterings for a photon escaping from the system to be

$$N_{\mathrm{esc}} = \frac{3}{\tau_0^3}\int_0^{\tau_0} \frac{\int_{-\infty}^{\infty} N_{\mathrm{sc}}(x,\tau_{\mathrm{s}})\,dx}{\int_{-\infty}^{\infty} N_{\mathrm{bd}}(x,\tau_{\mathrm{s}})\,dx}\tau_{\mathrm{s}}^2\,d\tau_{\mathrm{s}}. \tag{3.26}$$

This expression for the average number N_{esc} of scatterings cannot be solved analytically, so we numerically integrate it for 1600 equally log-spaced pairs of temperature T in the range of $10^3 - 10^6$ K (corresponding to some $\Delta\nu_{\mathrm{D}}$) and optical depth τ_0 in the range $10^3 - 10^9$. We fit these numerical results to the two-variable exponential polynomial function

$$\frac{N_{esc}(T,\tau_0)}{\tau_0} = \sum_{i,j}^{i+j\leq 5} \exp\left[A_{\mathrm{ij}}\,(\ln T)^i\,(\ln\tau_0)^j\right] \tag{3.27}$$

with the coefficients A_{ij} given in Table 3.4 and shown in Figure 3.9.

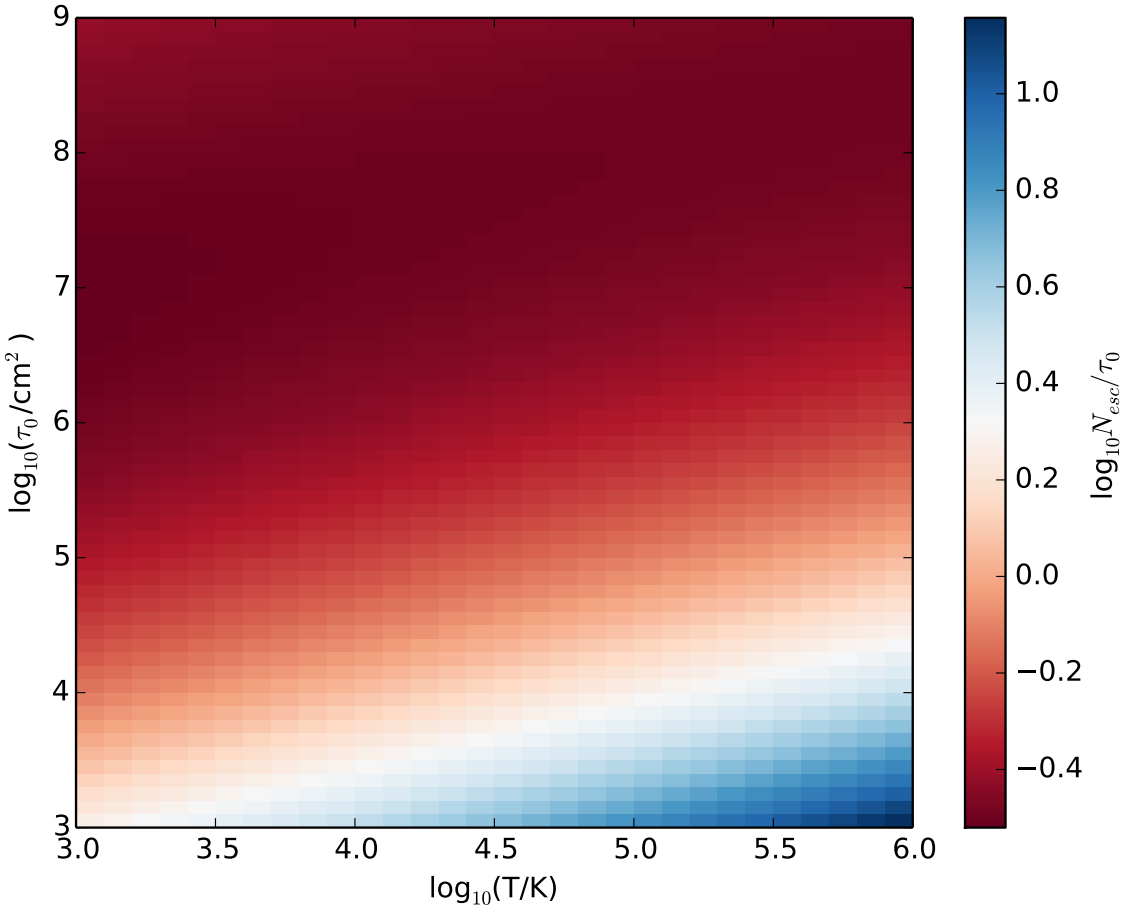

Figure 3.9: The two-dimensional functional fit (Equation 3.27; Table 3.4) to the calculated ratio of the average scattering number and the optical depth with respect to temperature and optical depth.

3.5.2 Radiation emission in a two-level system

We simplify the Lyα emission process by considering a two-level system because the spontaneous transitions from more excited states reside in the optically thin regime (Shang et al., 2010). The number density of the first excited state is related to the ground state by

$$\frac{n_2}{n_1} = \frac{C_{12} + (g_2/g_1)u_\nu A_{21}}{C_{21} + (1 + u_\nu)A_{21}}, \tag{3.28}$$

where $C_{\rm ij} = n_{\rm e}k_{\rm ij}({\rm e}) + n_{\rm H}k_{\rm ij}({\rm H})$ is the collisional de-excitation rate by free electrons and hydrogen atoms, and $g_n = 2n^2$ is the statistical weight (e.g. Tielens & Hollenbach, 1985; Omukai, 2001). The quantity

$$u_\nu = \frac{c^2}{2h\nu_{21}^3} J_{\rm cont}(\nu_{21}) \gg 1 \tag{3.29}$$

is related to the incoming photon flux at the energy difference $E_{21} = h\nu_{21} = 10.2$ eV between the states. The population density of the excited state (Equation 3.28) will change through collisional processes and spontaneous emission

$$\frac{dn_{2\to1}}{dt} = k_{21}({\rm e})n_2 n_{\rm e} + k_{21}({\rm H})n_2 n_1 + A_{21}n_2, \tag{3.30}$$

and the associated cooling rate per unit volume is reduced by the number of scatterings (Equation 3.27),

$$\Lambda_{2\to1} = \frac{h\nu_{21}}{N_{\rm esc}} \frac{dn_{2\to1}}{dt}. \tag{3.31}$$

We use the collisional coefficient rates from Omukai (2001):

$$k_{21}({\rm e}) = 1.155 \times 10^{-8} \frac{\sqrt{\beta(\beta+1)}}{\beta + 0.28} \ {\rm cm}^3 \ {\rm s}^{-1}, \tag{3.32}$$

$$k_{21}(\mathrm{H}) = 1.454 \times 10^{-15} \frac{T^{1/2} + 1.693 \times 10^{-5}\, T^{3/2}}{1 + 8.46 \times 10^{-17}\, T^2}\ \mathrm{cm}^3\ \mathrm{s}^{-1}, \tag{3.33}$$

where $\beta \equiv E_{21}/kT$. In the temperature range $T = 8 - 10 \times 10^3$ K, radiation originating from the two-photon process is in the optically thin regime, but we need to consider it in the model to obtain accurate electron states for the first excited state. The ratio between the $2s$ and $2p$ states is given by

$$\frac{n_{2\mathrm{s}}}{n_{2\mathrm{p}}} = \frac{g_{2\mathrm{s}}}{g_{2\mathrm{p}}} \frac{C_{2\mathrm{s}2\mathrm{p}}}{C_{2\mathrm{s}2\mathrm{p}} + A_{2\mathrm{s}1\mathrm{s}}}, \tag{3.34}$$

where $(g_{2\mathrm{s}}, g_{2\mathrm{p}}) = (2, 6)$, and $A_{2\mathrm{s}1\mathrm{s}} = 8.23\ \mathrm{s}^{-1}$. The collision rate can be described with the fit (Omukai, 2001)

$$C_{2\mathrm{s}2\mathrm{p}} = 6.21 \times 10^{-4} T^{-1/2} \ln(5.7T) \left[1 + \frac{0.78}{\ln(5.7T)}\right] n(\mathrm{e})\ \mathrm{s}^{-1}. \tag{3.35}$$

Lastly, the Einstein A-coefficient associated with spontaneous emission for the 2p $\rightarrow$ 1s and 2s $\rightarrow$ 1s transitions are respectively

$$A_{21} = \frac{n_{2\mathrm{p}}}{n_2} A_{2\mathrm{p}1\mathrm{s}} \quad \text{and} \quad A_{2\mathrm{ph}} = \frac{n_{2\mathrm{s}}}{n_2} A_{2\mathrm{s}1\mathrm{s}}, \tag{3.36}$$

resulting in the cooling rate from the two-photon process

$$\Lambda_{2\mathrm{ph}} = h\nu_{21} A_{2\mathrm{ph}} n_{2\mathrm{s}} \tag{3.37}$$

CHAPTER 4

CONCLUSION

4.1 Summary of the thesis

In this thesis, we studied the impact of Lyα radiation on the formation of supermassive black hole seed formation. We found that the temperatures increase within the outer portions of the collapsing birth cloud due to the trapping of the Lyα radiation. This heating could increase mass of the black hole seed by increasing the associated Jeans mass. The Lyα photon simulation was carried out with Monte Carlo methods, which took the gas cloud properties from an Enzo cosmological simulation that focused on a halo conducive for massive black hole formation through the direct collapse scenario.

In chapter 1, we first introduced the formation of the SMBHs and the three seeding mechanisms black holes. We then provided theoretical and observational evidence for why we chose the direct collapse black hole as the focus of this thesis. The radiation background and the reasons behind the target galaxy masses were discussed. We also described the sources, evolution, and effects of a Lyman-Werner (H_2 dissociating) background and the metallicity of the universe at very high redshifts $z \gtrsim 10$.

We then elaborated on the scattering mechanisms of Lyα photons and the cooling mechanisms within the primordial galaxies. We explored the ideal cases of slabs and spheres for which there are analytical results. We derived the radiation probability distribution that results in the Voigt profile. We showed the origin of Lyα photons, which is composed of two major sources—recombination and collisional excitation. We described the scattering mechanisms, focusing on the radiation scattering cross section of photons and neutral

hydrogen atoms, providing the basis for Monte Carlo methods. Lastly, we introduced the two-photon mechanism that is important in the cooling of chemically pristine halos in the early Universe.

In chapter 2, we described all of the relevant numerical methods and techniques. First, we reviewed the astrophysical code Enzo, including the physical equations solved, the hydrodynamics solvers, the chemical networks considered, the basis behind structured adaptive mesh refinement, and methods to solve the radiation transfer equation. Next we listed the details and procedures used in the transfer of Lyα Monte Carlo radiation in our code. The random number generator and the Monte Carlo rejection method are described in detail in this section. Lastly, we tested our code with the ideal uniform sphere case, comparing it against the standard Neufeld test and the scattering number test both of which have analytical solutions.

In chapter 3, we explored the dynamics and cooling of a primordial gas cloud with and without Lyα radiation. We carried out a cosmological simulation that focused on the collapse of a halo that is conducive to massive black hole seed formation. We post-processed this simulation data with a Monte Carlo radiation transfer calculation for a static snapshots, where we considered a density profile extracted from the simulation. We also considered various configurations of the electron and hydrogen number densities during different stages of the catastrophic collapse. We fit the resulting evolution of the collapse with the Gamma distributions that are useful for future studies. By doing so, we determined the confidence intervals for parameters that describe the propagation of Lyα radiation within this dense self-gravitating gas cloud. The resulting equation of state of such an optically-thick cloud are then compared with other simulation results that considered a static equation of state throughout the collapse, improving on this previously-used simple model.

4.2 Future Development

In an ideal world, Monte Carlo Lyα transfer calculations would be embedded self-consistently into hydrodynamics simulations. However, the high computational expense of such a calculation prevents such an improvement. As a result, the Lyα transfer calculations miss the rich dynamics that arise when the full hydrodynamical state are utilized in a transfer calculation, which could then have a back-reaction to the momentum and pressure of the Lyα photon scatterings. The fields of machine learning are quickly being applied to scientific problems, and here we propose an Expectation-Maximization (EM) method to further investigate the effects of Lyα transfer on the direct collapse black hole scenario.

We propose to use the EM method to generate the density distribution functions to be used with radiation transfer. For instance, the hydrodynamical state in an Enzo simulation would be represented by a 3-D mixture of Gaussian distributions to simulate each dense clump. For such a combination of K Gaussians, the same number of Gaussian density concentrations are identified. In the rest of this thesis, we introduce a classical K-Gaussian EM method and then derive the K-concentration method that is applied to a cosmological self-gravitating collapse.

4.2.1 Details of the K-Gaussian Model

Consider a uni-modal Gaussian 3-D distribution of

$$\mathcal{N}(X|\mu_k, \Sigma_k) \equiv \frac{1}{|\Sigma|^{1/2}(2\pi)^{3/2}} \exp\left[-\frac{1}{2}\left(X-\mu_k\right)^T \Sigma_k^{-1}(X-\mu_k)\right]. \tag{4.1}$$

Suppose we have N indistinguishable points in dataset D, describing the spatial distribution of hydrogen number densities. Now we consider this distribution at some location X a

mixture of K Gaussians as

$$p(X) = \sum_{k=1}^{K} \pi_k \mathcal{N}(X|\mu_k, \Sigma_k), \tag{4.2}$$

where $\mathcal{N}$ describes a single Gaussian distribution. The EM procedure is as follows:

1. Initialize the variables (π_k, μ_k, Σ_k) with $k = 1, ..., K$. Note that the initialization should be widely separated because they can denote different distributions.

2. Iterate following steps until the calculated conditions reach or converge to the expected value:

   (a) "E-step": update the τ_k^i value given current (π_k, μ_k, Σ_k).

$$\begin{aligned} \tau_k^i = p(z_k^i = 1|D, \mu, \Sigma) = \frac{\pi_k \mathcal{N}(x_i|\mu_k, \Sigma_k)}{\sum_{k'=1}^{K} \pi_{k'} \mathcal{N}(x_i|\mu_{k'}, \Sigma_{k'})} \\ \text{with} \quad (k = 1, 2, ..., K) \quad \text{and} \quad (i = 1, 2, ..., N) \end{aligned} \tag{4.3}$$

   (b) "M-step": update (π_k, μ_k, Σ_k) given a τ_k^i value

$$\begin{aligned} \pi_k &= \frac{\Sigma_i \tau_k^i}{N} \\ \mu_k &= \frac{\Sigma_i \tau_k^i x^i}{\Sigma_i \tau_k^i} \\ \Sigma_k &= \frac{\Sigma_i \tau_k^i (x^i - \mu_k)(x^i - \mu_k)^T}{\Sigma_i \tau_k^i} \\ \text{with} \quad & (k = 1, 2, ..., K) \end{aligned} \tag{4.4}$$

4.2.2 Details of the K-Concentration Model

During the formation of a direct collapse black hole, there are mergers of the halos and internal gas clumps that contribute separately to the radiation field. This process happens because of the long-range effects of Lyα radiation transfer escaping from individual gas

clumps that could then impact nearby clumps. For a typically single halo, we assume the same structure applied,

$$log(n) = \begin{cases} L_n - \beta \log(r) \quad \text{for} \quad (r > \Delta) \\ L_n - \beta \log(\Delta) \quad \text{for} \quad (r \leq \Delta) \end{cases}, \tag{4.5}$$

where n is the neutral hydrogen density and r is the radius in cgs units with $r = |\hat{T}(X - \mu)|$. The symbol $\hat{T}$ represents the transformation from a sphere to an off-axis ellipsoid, and μ is the center of the density concentration, while L_n and β are constant parameters. The parameter Δ is the cutoff radius for an isodensity sphere. Note that we assume a logarithmic number density profile in this manner. After normalization, we obtain the probability density

$$p(X|\mu, \Delta, \hat{T}) \propto \frac{\log n}{r_{n0}^3 - \Delta^3}, \tag{4.6}$$

where r_{n0} is where the radius at which the density is unity. At this location, we can neglect the generation of photons, where the condition $r_{n0} \gg \Delta$ also holds. We now have the probability density

$$\begin{aligned} p(X|\mu_k, \Delta_k, \hat{T}_k) =& \frac{1}{C}[\Theta(|\hat{T}_k(X - \mu_k)| - \Delta_k)(L_n - \beta \log(|\hat{T}_k(X - \mu_k)|)) \\ &+ \Theta(\Delta_k - |\hat{T}_k(X - \mu_k)|)(L_n - \beta \log(\Delta_k))], \end{aligned} \tag{4.7}$$

where C is a constant. We can calculate the log likelihood of m variables as

$$\begin{aligned} l(\theta_{\text{param}}, D_{\text{var}}) &= \log \prod_{i=0}^{m} \sum_{k=1}^{K} p(X_i, k|\theta) \\ &= \sum_{i=1}^{m} \log \left[\sum_{k=1}^{K} \pi_k \, p(X_i|\mu_k, \Delta_k, \hat{T}_k) \right] \end{aligned} \tag{4.8}$$

Applying the convex method to the log likelihood, we arrive at

$$l(\theta, D) \geq f(\theta) = E_{p(k_1,k_2,\ldots,k_K)} \left[\sum_{i=0}^{m} \log(p(X_i, k|\theta)) \right] \tag{4.9}$$

We now reformulate the E-step as the following expression

$$\tau_k^i = \frac{\pi_k p(X_i|\mu_k, \Delta_k, \hat{T}_k)}{\sum_{k'} \pi_{k'}\, p(X_i|\mu_{k'}, \Delta_{k'}, \hat{T}_{k'})}. \tag{4.10}$$

In the same light, we can generate two additional non-normalized probability quantities, $r_k^i = |\hat{T}_k(X_i - \mu_k)|$ and $\theta_{ki} = \Theta(r_k^i - \Delta_k)$. We reformulate the M-step as

$$\begin{aligned} f(\theta) = & \sum_{i=1}^{m} \sum_{k=1}^{K} \tau_k^i \Big\{ \log \pi_k + \log \Big[\Theta(|\hat{T}_k(X_i - \mu_k)| - \Delta_k)(L_n - \\ & \beta \log(|\hat{T}_k(X_i - \mu_k)|)) + \Theta(\Delta_k - |\hat{T}_k(X_i - \mu_k)|)(L_n - \beta log(\Delta_k)) \Big] \\ & + C \Big\}, \end{aligned} \tag{4.11}$$

where C is a constant. The Lagrangian of the system can be written as

$$L = \sum_{i=1}^{m} \sum_{k=1}^{K} \tau_k^i \left(\log \pi_k + \mathcal{O} \right) + \lambda \left(1 - \sum_{k=1}^{K} \pi_k \right), \tag{4.12}$$

where $\mathcal{O}$ describes higher-order terms. From this expression, we determine that

$$\pi_k = \frac{1}{m} \sum_{i=1}^{m} \tau_k^i \tag{4.13}$$

By restricting the system with the following conditions, $\partial L/\partial \mu_k = 0$, $\partial L/\partial \Delta_k = 0$ and $\partial L/\partial \hat{T}_k = 0$, we finally arrive at

$$\begin{aligned}
\mu_k &= \frac{\sum_{i=1}^{m} \frac{\tau_k^i X_i \theta_{ki}}{(r_k^i)^2 (L_n - \beta \log(r_k^i))}}{\sum_{i=1}^{m} \frac{\tau_k^i \theta_{ki}}{(r_k^i)^2 (L_n - \beta \log(r_k^i))}} \\
\Delta_k &= \min(r_k^i) \\
\hat{T}_{kpq} &= \frac{\sum_{i=1}^{m} \sum_{c \neq q} \frac{\tau_k^i \hat{T}_{kpc} (\mu_{kc} - X_{ic})(X_{iq} - \mu_{kq}) \theta_{ki}}{(r_k^i)^2 (L_n - \beta \log(r_k^i))}}{\sum_{i=1}^{m} \frac{\tau_k^i (\mu_{kq} - X_{iq})^2 \theta_{ki}}{(r_k^i)^2 (L_n - \beta \log(r_k^i))}}
\end{aligned} \tag{4.14}$$

In order to make the K-concentrations more physically representative of the system, we make an adjustment to the original distribution function as

$$\log(n) = \begin{cases} \max[10(L_n - \beta \log(r)) - K_0, 0] & \text{for} \quad (r > \Delta) \\ \max[10(L_n - \beta \log(\Delta)) - K_0, 0] & \text{for} \quad (r \leq \Delta) \end{cases} \tag{4.15}$$

By identifying each K-concentration in a simulation dataset, it is possible to extend the Lyα scattering radiation transfer equation to the halo collapse scenario presented in this thesis that use our Monte Carlo method. Furthermore, the application of neural network can be utilized for the computational cells in simulations, where the outflow of the radiation fields are "black boxes" given an input of the incident radiation and the parameters of the cells. With this framework, it could be possible to develop an efficient and fast computational model to handle the Lyα radiation transfer self-consistently in radiation hydrodynamics simulations.

BIBLIOGRAPHY

Abel T., Anninos P., Zhang Y., Norman M. L., 1997, New A, 2, 181

Abel T., Bryan G. L., Norman M. L., 2002, Science, 295, 93

Adams T. F., 1971, ApJ, 168, 575

Adams T. F., Hummer D. G., Rybicki G. B., 1971, J. Quant. Spec. Radiat. Transf., 11, 1365

Agarwal B., Khochfar S., 2015, MNRAS, 446, 160

Agarwal B., Dalla Vecchia C., Johnson J. L., Khochfar S., Paardekooper J.-P., 2014, MNRAS, 443, 648

Ahn S.-H., Lee H.-W., Lee H. M., 2002, ApJ, 567, 922

Aihara H., et al., 2017, preprint, (arXiv:1704.05858)

Alexander T., Natarajan P., 2014, Science, 345, 1330

Almgren A. S., Bell J. B., Lijewski M. J., Lukić Z., Van Andel E., 2013, ApJ, 765, 39

Alvarez M. A., Komatsu E., Doré O., Shapiro P. R., 2006, ApJ, 647, 840

Alvarez M. A., Wise J. H., Abel T., 2009, ApJ, 701, L133

Anninos P., Zhang Y., Abel T., Norman M. L., 1997, New A, 2, 209

Antonov V. A., 1962, Solution of the problem of stability of stellar system Emden's density law and the spherical distribution of velocities

Bacon R., et al., 2010, in Ground-based and Airborne Instrumentation for Astronomy III. p. 773508, doi:10.1117/12.856027

Baker J. G., Menzel D. H., 1938, ApJ, 88, 52

Barnes L. A., Haehnelt M. G., 2009, MNRAS, 397, 511

Barnes L. A., Haehnelt M. G., 2010, MNRAS, 403, 870

Becerra F., Greif T. H., Springel V., Hernquist L. E., 2015, MNRAS, 446, 2380

Begelman M. C., Volonteri M., Rees M. J., 2006, MNRAS, 370, 289

Berger M. J., Colella P., 1989, Journal of Computational Physics, 82, 64

Black J. H., 1981, MNRAS, 197, 553

Bondi H., 1952, MNRAS, 112, 195

Bonnor W. B., 1956, MNRAS, 116, 351

Bromm V., Loeb A., 2003, ApJ, 596, 34

Bromm V., Loeb A., 2004, New A, 9, 353

Bromm V., Coppi P. S., Larson R. B., 1999, ApJ, 527, L5

Bromm V., Ferrara A., Coppi P. S., Larson R. B., 2001, MNRAS, 328, 969

Bromm V., Yoshida N., Hernquist L., 2003, ApJ, 596, L135

Bryan G. L., Norman M. L., 1997, ArXiv Astrophysics e-prints,

Bryan G. L., Norman M. L., Stone J. M., Cen R., Ostriker J. P., 1995, Computer Physics Communications, 89, 149

Bryan G. L., et al., 2014, ApJS, 211, 19

Cen R., 1992, ApJS, 78, 341

Colella P., Woodward P. R., 1984, Journal of Computational Physics, 54, 174

Collins D., 2010, in From Stars to Galaxies: Connecting our Understanding of Star and Galaxy Formation. p. 17

Collins D. C., Padoan P., Norman M. L., Xu H., 2011, ApJ, 731, 59

Collins D. C., Kritsuk A. G., Padoan P., Li H., Xu H., Ustyugov S. D., Norman M. L., 2012, ApJ, 750, 13

Couchman H. M. P., 1991, ApJ, 368, L23

Cowie L. L., Hu E. M., 1998, AJ, 115, 1319

Cunningham A. J., Frank A., Varnière P., Mitran S., Jones T. W., 2009, ApJS, 182, 519

Davies M. B., Miller M. C., Bellovary J. M., 2011, ApJ, 740, L42

Dijkstra M., Haiman Z., Spaans M., 2006, ApJ, 649, 14

Dijkstra M., Haiman Z., Mesinger A., Wyithe J. S. B., 2008, MNRAS, 391, 1961

Duffell P. C., MacFadyen A. I., 2011, ApJS, 197, 15

Ebert R., 1955, ZAp, 37, 217

Eisenstein D. J., Hut P., 1998, ApJ, 498, 137

Ekström S., Meynet G., Maeder A., Barblan F., 2008, A&A, 478, 467

Fan X., 2006, New A Rev., 50, 665

Fang T., Bryan G. L., 2001, ApJ, 561, L31

Ferland G. J., Korista K. T., Verner D. A., Ferguson J. W., Kingdon J. B., Verner E. M., 1998, PASP, 110, 761

Fryxell B., et al., 2000, ApJS, 131, 273

Furlanetto S. R., Schaye J., Springel V., Hernquist L., 2005, ApJ, 622, 7

Fynbo J. U., Møller P., Warren S. J., 1999, MNRAS, 305, 849

Fynbo J. U., Møller P., Thomsen B., 2001, A&A, 374, 443

Gammie C. F., Shapiro S. L., McKinney J. C., 2004, ApJ, 602, 312

Ge Q., Wise J. H., 2017, MNRAS, 472, 2773

Gingold R. A., Monaghan J. J., 1977, MNRAS, 181, 375

Glover S., 2005, Space Sci. Rev., 117, 445

Glover S. C. O., 2015, MNRAS, 451, 2082

Glover S. C. O., Abel T., 2008, MNRAS, 388, 1627

Górski K. M., Hivon E., Banday A. J., Wandelt B. D., Hansen F. K., Reinecke M., Bartelmann M., 2005, ApJ, 622, 759

Gronke M., Bull P., Dijkstra M., 2015, ApJ, 812, 123

Hahn O., Abel T., 2011, MNRAS, 415, 2101

Haiman Z., Loeb A., 2001, ApJ, 552, 459

Haiman Z., Rees M. J., 2001, ApJ, 556, 87

Hamilton D. R., 1940, Physical Review, 58, 122

Harrington J. P., 1973, MNRAS, 162, 43

Heger A., Woosley S. E., 2002, ApJ, 567, 532

Heger A., Fryer C. L., Woosley S. E., Langer N., Hartmann D. H., 2003, ApJ, 591, 288

Heggie D. C., 1975, MNRAS, 173, 729

Hénon M., 1965, Annales d'Astrophysique, 28, 992

Herrmann F., Hinder I., Shoemaker D., Laguna P., Matzner R. A., 2007, ApJ, 661, 430

Hill G. J., et al., 2008, in Kodama T., Yamada T., Aoki K., eds, Astronomical Society of the Pacific Conference Series Vol. 399, Panoramic Views of Galaxy Formation and Evolution. p. 115 (arXiv:0806.0183)

Hinshaw G., et al., 2013, ApJS, 208, 19

Hummels C. B., Bryan G. L., Smith B. D., Turk M. J., 2013, MNRAS, 430, 1548

Hummer D. G., 1962, MNRAS, 125, 21

Inayoshi K., Haiman Z., Ostriker J. P., 2016, MNRAS, 459, 3738

Jeon M., Pawlik A. H., Greif T. H., Glover S. C. O., Bromm V., Milosavljević M., Klessen R. S., 2012, ApJ, 754, 34

Jessop C., Duncan M., Chau W. Y., 1994, Journal of Computational Physics, 115, 339

Johnson J. L., Bromm V., 2007, MNRAS, 374, 1557

Johnson J. L., Dijkstra M., 2017, A&A, 601, A138

Johnson J. L., Greif T. H., Bromm V., 2007, ApJ, 665, 85

Johnson J. L., Whalen D. J., Fryer C. L., Li H., 2012, The Astrophysical Journal, 750, 66

Jones E., Oliphant T., Peterson P., et al., 2001, SciPy: Open source scientific tools for Python, http://www.scipy.org/

Kawakatu N., Umemura M., 2005, ApJ, 628, 721

Kitayama T., Yoshida N., Susa H., Umemura M., 2004, ApJ, 613, 631

Kravtsov A. V., Klypin A. A., Khokhlov A. M., 1997, ApJS, 111, 73

Kritsuk A. G., Norman M. L., 2004, ApJ, 601, L55

Krumholz M. R., Klein R. I., McKee C. F., Offner S. S. R., Cunningham A. J., 2009, Science, 323, 754

Kuhlen M., Madau P., 2005, MNRAS, 363, 1069

Lackner C. N., Cen R., Ostriker J. P., Joung M. R., 2012, MNRAS, 425, 641

Laney C. D., 1998, Monthly Notes of the Astronomical Society of South Africa, 57, 8

Latif M. A., Zaroubi S., Spaans M., 2011, MNRAS, 411, 1659

Laursen P., Razoumov A. O., Sommer-Larsen J., 2009, ApJ, 696, 853

Laursen P., Sommer-Larsen J., Razoumov A. O., 2011, ApJ, 728, 52

Li Y., Bryan G. L., 2012, ApJ, 747, 26

Lodato G., Natarajan P., 2006, MNRAS, 371, 1813

Loeb A., Rasio F. A., 1994, ApJ, 432, 52

Loeb A., Rybicki G. B., 1999, ApJ, 524, 527

Loken C., Norman M. L., Nelson E., Burns J., Bryan G. L., Motl P., 2002, ApJ, 579, 571

Lucy L. B., 1977, AJ, 82, 1013

Madau P., Rees M. J., 2001, ApJ, 551, L27

Martin E. C., et al., 2014, in Ground-based and Airborne Instrumentation for Astronomy V. p. 914781, doi:10.1117/12.2056896

McGreer I. D., Bryan G. L., 2008, ApJ, 685, 8

Micic M., Abel T., Sigurdsson S., 2006, MNRAS, 372, 1540

Mignone A., Zanni C., Tzeferacos P., van Straalen B., Colella P., Bodo G., 2012, ApJS, 198, 7

Mortlock D. J., et al., 2011, Nature, 474, 616

Neufeld D. A., 1990, ApJ, 350, 216

Nilsson K. K., Meisenheimer K., 2009, New A Rev., 53, 37

Nilsson K. K., Fynbo J. P. U., Møller P., Sommer-Larsen J., Ledoux C., 2006, A&A, 452, L23

Norman M. L., Bryan G. L., Harkness R., Bordner J., Reynolds D., O'Shea B., Wagner R., 2007, preprint, (arXiv:0705.1556)

O'Leary R. M., Rasio F. A., Fregeau J. M., Ivanova N., O'Shaughnessy R., 2006, ApJ, 637, 937

O'Shea B. W., Norman M. L., 2007, ApJ, 654, 66

O'Shea B. W., Norman M. L., 2008, ApJ, 673, 14

O'Shea B. W., Bryan G., Bordner J., Norman M. L., Abel T., Harkness R., Kritsuk A., 2004, ArXiv Astrophysics e-prints,

Omukai K., 2001, ApJ, 546, 635

Osterbrock D. E., Ferland G. J., 2006, Astrophysics of gaseous nebulae and active galactic nuclei. University Science Books

Partridge R. B., Peebles P. J. E., 1967, ApJ, 147, 868

Planck Collaboration et al., 2016, A&A, 594, A13

Rees M. J., Ostriker J. P., 1977, MNRAS, 179, 541

Regan J. A., Haehnelt M. G., 2009, MNRAS, 393, 858

Regan J. A., Johansson P. H., Wise J. H., 2016, MNRAS, 459, 3377

Regan J. A., Visbal E., Wise J. H., Haiman Z., Johansson P. H., Bryan G. L., 2017, Nature Astronomy, 1, 0075

Reynolds D. R., Hayes J. C., Paschos P., Norman M. L., 2009, Journal of Computational Physics, 228, 6833

Ricotti M., Ostriker J. P., 2004, MNRAS, 352, 547

Rosen A. L., Lopez L. A., Krumholz M. R., Ramirez-Ruiz E., 2014, MNRAS, 442, 2701

Ruffert M., 1994, in Shafter A. W., ed., Astronomical Society of the Pacific Conference Series Vol. 56, Interacting Binary Stars. p. 434

Salpeter E. E., 1964, ApJ, 140, 796

Sarazin C. L., White III R. E., 1987, ApJ, 320, 32

Schleicher D. R. G., Spaans M., Glover S. C. O., 2010, ApJ, 712, L69

Shang C., Bryan G. L., Haiman Z., 2010, MNRAS, 402, 1249

Shapiro S. L., 2004, ApJ, 610, 913

Slyz A. D., Devriendt J. E. G., Bryan G., Silk J., 2005, MNRAS, 356, 737

Smith B. D., Hallman E. J., Shull J. M., O'Shea B. W., 2011, ApJ, 731, 6

Smith A., Safranek-Shrader C., Bromm V., Milosavljević M., 2015, MNRAS, 449, 4336

Smith A., Becerra F., Bromm V., Hernquist L., 2017, preprint, (arXiv:1706.02751)

Spaans M., Silk J., 2006, ApJ, 652, 902

Spitzer Jr. L., 1969, ApJ, 158, L139

Spitzer Jr. L., 1978, JRASC, 72, 349

Springel V., 2010, MNRAS, 401, 791

Stacy A., Bromm V., Loeb A., 2011, MNRAS, 413, 543

Stenflo J. O., 1980, A&A, 84, 68

Stone J. M., Norman M. L., 1992, ApJS, 80, 753

Tasitsiomi A., 2006, ApJ, 648, 762

Tassis K., Abel T., Bryan G. L., Norman M. L., 2003, ApJ, 587, 13

The Enzo Collaboration et al., 2014, ApJS, 211, 19

Thorne K. S., 1974, Scientific American, 231, 32

Thoul A. A., Weinberg D. H., 1995, ApJ, 442, 480

Tielens A. G. G. M., Hollenbach D., 1985, ApJ, 291, 722

Truelove J. K., Klein R. I., McKee C. F., Holliman II J. H., Howell L. H., Greenough J. A., 1997, ApJ, 489, L179+

Truelove J. K., Klein R. I., McKee C. F., Holliman II J. H., Howell L. H., Greenough J. A., Woods D. T., 1998, ApJ, 495, 821

Turk M. J., Abel T., O'Shea B., 2009, Science, 325, 601

Unno W., 1952, PASJ, 3, 158

Van Borm C., Bovino S., Latif M. A., Schleicher D. R. G., Spaans M., Grassi T., 2014, A&A, 572, A22

Verhamme A., Schaerer D., Maselli A., 2006, A&A, 460, 397

Villumsen J. V., 1989, ApJS, 71, 407

Visbal E., Haiman Z., Terrazas B., Bryan G. L., Barkana R., 2014a, MNRAS, 445, 107

Visbal E., Haiman Z., Bryan G. L., 2014b, MNRAS, 445, 1056

Volonteri M., Rees M. J., 2006, ApJ, 650, 669

Volonteri M., Lodato G., Natarajan P., 2008, MNRAS, 383, 1079

Wang P., Abel T., Zhang W., 2008, ApJS, 176, 467

Whalen D., Abel T., Norman M. L., 2004, ApJ, 610, 14

White S. D. M., Frenk C. S., 1991, ApJ, 379, 52

White S. D. M., Rees M. J., 1978, MNRAS, 183, 341

Willott C. J., et al., 2010, AJ, 139, 906

Wise J. H., Abel T., 2007, ApJ, 665, 899

Wise J. H., Abel T., 2011, MNRAS, 414, 3458

Wise J. H., Turk M. J., Abel T., 2008, ApJ, 682, 745

Wolcott-Green J., Haiman Z., 2012, MNRAS, 425, L51

Wu X.-B., et al., 2015, Nature, 518, 512

Xu H., O'Shea B. W., Collins D. C., Norman M. L., Li H., Li S., 2008, ApJ, 688, L57

Xu H., Li H., Collins D. C., Li S., Norman M. L., 2011, ApJ, 739, 77

Yahagi H., Yoshii Y., 2001, ApJ, 558, 463

Yajima H., Khochfar S., 2014, MNRAS, 441, 769

Yoshida N., Omukai K., Hernquist L., Abel T., 2006, ApJ, 652, 6

Zel'dovich Y. B., 1964, Soviet Physics Doklady, 9, 195

Zhang W., MacFadyen A. I., 2006, ApJS, 164, 255

Zheng Z., Miralda-Escudé J., 2002, ApJ, 578, 33

Ziegler U., 2005, Computer Physics Communications, 170, 153